SEISMIC PERFORMANCE UPGRADING OF REINFORCED CONCRETE FRAMES USING SHAPE MEMORY ALLOY BARS

Master of Science Thesis

Burak DURAN

Eskisehir, 2018

SEISMIC PERFORMANCE UPGRADING OF REINFORCED CONCRETE FRAMES USING SHAPE MEMORY ALLOY BARS

Burak DURAN

Master of Science Thesis

Department of Civil Engineering
Supervisor: Assoc. Prof. Dr. Özgür AVŞAR
Co-advisor: Assoc. Prof. Dr. Kadri CAN ATLI

Eskisehir
Anadolu University
Graduate School of Science
June, 2018

FINAL APPROVAL FOR THESIS

This thesis titled "Seismic Performance Upgrading of Reinforced Concrete Frames Using Shape Memory Alloy Bars" has been prepared and submitted by Burak DURAN in partial fullfillment of the requirements in "Anadolu University Directive on Graduate Education and Examination" for the Degree of Master of Science in Civil Engineering Department has been examined and approved on 28/06/2018.

Committee   Signature

Member (Supervisor)   :   Assoc. Prof. Dr. Özgür AVŞAR   …………..

Member   :   Prof. Dr. Murat Altuğ ERBERİK   …………..

Member   :   Assoc. Prof. Dr. İlker KAZAZ   …………..

Prof. Dr. Ersin YÜCEL

....

Director

Graduate School of Science

ABSTRACT

SEISMIC PERFORMANCE UPGRADING OF REINFORCED CONCRETE FRAMES USING SHAPE MEMORY ALLOY BARS

Burak DURAN

Department of Civil Engineering

Programme in Mechanics

Anadolu University, Graduate School of Science, June, 2018

Supervisor: Assoc. Prof. Dr. Özgür AVŞAR

(Co-Supervisor: Assoc. Prof. Dr. Kadri CAN ATLI)

Turkey, which is located on an earthquake zone containing active fault lines, experiences earthquakes that cause loss of live and property. Considering that a serious part of the present population lives in cities near fault lines which can produce severe earthquakes and a significant part of our reinforced concrete buildings are substandard structures. It is important to upgrade the seismic performance of existing substandard RC buildings in order to avoid loss of live and property. In this master's thesis study, four 2/3 scaled and one-bay one-storey reinforced concrete frame representing existing substandard RC buildings with some deficiencies were designed and constructed in the laboratory conditions and then tested under displacement controlled quasi-static reversed cyclic loading experimentally. The first RC frame was the reference frame and rest of the frames were upgraded with conventional steel, Copper-Aluminum-Mangane (CuAlMn) and Nickel-Titanium (NiTi) Superelastic (SE) Shape Memory Alloys (SMAs) with the intent of enhancing seismic performance of non-code-conforming RC frames. The strengthening bars were attached to the substandard RC frame and then tested under the same quasi static cyclic loading. At the end of the eperiments, the SMAs showed a superelastic effect during the cyclic displacements reducing the residual displacements and the shape of hysteresis were flag-shaped due to inherit characteristics of SMAs.

Keywords: Reinforced concrete, Shape memory alloy, Upgrading, Ambient vibration, Flexural damage

ÖZET

ŞEKİL BELLEKLİ ALAŞIM ÇUBUKLAR İLE BETONARME ÇERÇEVELERİN SİSMİK PERFORMANSININ İYİLEŞTİRİLMESİ

Burak DURAN

İnşaat Mühendisliği Anabilim Dalı

Mekanik Bilim Dalı

Anadolu Üniversitesi, Fen Bilimleri Enstitüsü, Haziran, 2018

Danışman: Doç. Dr. Özgür AVŞAR

(İkinci Danışman: Doç. Dr. Kadri CAN ATLI)

Aktif fay hatlarını içerisinde barındıran bir deprem kuşağı üzerinde yer alan ülkemizde, can ve mal kayıplarına neden olan depremler yaşanmaktadır. Mevcut nüfusun önemli bir bölümünün şiddetli depremler üretebilecek fay hatlarına yakın şehirlerde yaşadığı ve mevcut betonarme binaların büyük bir bölümünün standart-altı yapılar olduğu düşünüldüğünde, bu binaların performanslarının arttırılarak can ve mal kayıplarının önüne geçilmesi önem arz etmektedir. Bu yüksek lisans tez çalışması kapsamında, mevcut betonarme çerçeveli binaları çeşitli eksiklikler ile temsil eden, 2/3 ölçekli, tek katlı ve tek açıklıklı, dolgu duvarsız, 4 adet betonarme çerçeve laboratuvar ortamında üretilmiş ve deneysel olarak deplasman kontrollü tersinir tekrarlı yatay yükler altında test edilmiştir. İlk çerçeve referans olmak üzere, sonraki çerçeveler sıradan çelik, Bakır-Alüminyum-Mangan (CuAlMn) ve Nikel-Titanyum (NiTi) Şekil Bellekli Alaşım (ŞBA) çubuklar ile güçlendirilerek sismik performanslarının arttırılması hedeflenmiştir. Güçlendirme çubukları, geliştirilen güçlendirme detayı ile çerçevelerin içerisine bütünleşik hale getirilmiş ve tersinir tekrarlı yatay yük altında test edilmişlerdir. Deney sonuçlarına göre, şekil bellekli alaşımların sahip oldukları "süperelastisite" özelliği sayesinde betonarme çerçevelerin kuvvet-deplasman eğrisi üzerinde gözlemlenmiş ve bu sayede çerçevelerin kalıcı deplasman değerleri azalırken, enerji sönümleme kapasiteleri artmıştır. Bu çalışma ile, mevcut binaların deprem performanslarının iyileştirilmesi kapsamında yenilikçi bir yöntem önerisi sunulmuştur.

Anahtar Kelimeler: Betonarme çerçeve, Şekil bellekli alaşım, Güçlendirme, Çevresel titreşim, Eğilme hasarı

ACKNOWLEDGEMENT

STATEMENT OF COMPLIANCE WITH ETHICAL PRINCIPLES AND RULES

I hereby truthfully declare that this thesis is an original work prepared by me; that I have behaved in accordance with the scientific ethical principles and rules throughout the stages of preparation, data collection, analysis and presentation of my work; that I have cited the sources of all the data and information that could be obtained within the scope of this study, and included these sources in the references section; and that this study has been scanned for plagiarism with "scientific plagiarism detection program" used by Anadolu University, and that "it does not have any plagiarism" whatsoever. I also declare that, if a case contrary to my declaration is detected in my work at any time, I hereby express my consent to all the ethical and legal consequences that are involved.

....

Burak DURAN

TABLE OF CONTENTS

TABLES

TABLE OF FIGURES

xiii

xiv

TABLE OF SYMBOLS

$\dot{\varepsilon}$	: Strain rate
ε_r	: Residual strain
ε_{sh}	: Strain at starting of strain-hardening for reinforcement bars
ε_{su}	: Ultimate strain of reinforcement bars
ε_{sy}	: Yielding strain of reinforcement bars
ε_u	: Ultimate strain
ε_y^{AS}	: Austenite yield strain
σ_s^{AM}	: Austenite to martensite start transformation stress
σ_s^{MA}	: Martensite to austenite start transformatiom stress
σ_f^{AM}	: Austenite to martensite finish transformation stress
σ_f^{MA}	: Martensite to austenite finish transformation stress
σ_{yo}	: Observed yield strength
μ_1	: Ductility calculated from bilinear approximation with two-slope
μ_2	: Ductility calculated from bilinear approximation with one-slope
β	: The lower plateau stress factor
α	: Post yield stiffness ratio
ξ_{eq}	: Equivalent viscous damping ratio
Δ_{max}^+	: Lateral displacement corresponding ultimate load
$\Delta_{max,i}^+$	: Maximum lateral displacement in forward direction at imposed cycle
$\Delta_{max,i}^-$	: Maximum lateral displacement in backward direction at imposed cycle
$\Delta_{0.60}^+$	: Calculated yielding displacement using the secant stifness method
$\Delta_{u,0.85}^+$	: Lateral displacement corresponding to 85% of the ultimate load
Δ_y^+	: Calculated yield displacement using initial stiffness
$\Delta_{y,1}^+$	: Yield displacement using bilinear approximation with one-slope
$\Delta_{y,2}^+$	: Yield displacement using bilinear approximation with two-slope
Δ_{RL}^+	: Loading residual displacement in forward loading
Δ_{RL}^-	: Loading residual displacement in backward loading
Δ_{rm}^+	: Residual displacement calculated from the first method upon unloading
Δ_{RU}^+	: Unloading residual displacement in forward loading
Δ_{RU}^-	: Unloading residual displacement in backward loading
A_c	: Gross section area of column
A_f	: Austenite finish temperature
A_s	: Austenite start temperature
A_{loop}	: The area enclosed within the force-displacement curve of imposed cycle
A_0	: Area of the lateral reinforcement
b_w	: Width of column
BRB	: Buckling restrained braces
CBS	: Concentrically braced frames
CFS	: Carbon fiber sheets
$CFRP$	: Carbon fiber reinforced polymer
$CuAlMn$	: Copper-aluminum-mangane
d	: Effective height of the cross section
D_{max}	: Peak displacement at imposed drift cycle
ECC	: Engineering cementitious composite

E_D	: Dissipated energy during a cyclic motion
E_{so}	: Stored or elastic strain energy
f_{ct}	: Tensile strength of concrete
f_{su}	: Ultimate strength of reinforcement steel
f_{sy}	: Yield strength of reinforcement steel
f_{yw}	: Yield strength of lateral reinforcement
F_{max}	: Peak force at imposed drift cycle
$GFRP$	: Glass fiber reinforced polymer
IDA	: Incremental dynamic analysis
k_1	: The austenite modulus
k_2	: The post yield stiffness
k_3	: The martensite modulus
K_i	: Initial stiffness
K_o	: Initial slope representing the elastic stiffness
K_s	: Secant stiffness
K_t	: Tangential stiffness
LC	: Load cell
$LVDT$	: Linear variable differential transformer
MRF	: Moment resisting frames
M_f	: Martensite finish temperature
M_s	: Martensite start temperature
n	: Number of stirrup arms at a section
N_d	: Axial load applied to the column end
$NiTi$	: Nickel-Titanium
RC	: Reinforced concrete
$RVFD$	: Re-centering variable friction device
s	: Spacing of lateral reinforcement
SE	: Super-elastic
SMA	: Shape memory alloy
SHM	: Structural health monitoring
SG	: Strain gage
V_i	: 60% percent of the maximum lateral load
V_j	: Yielding load obtained from tangential stiffness
V_{max}	: Ultimate lateral load
$V_{max,i}^{+}$	: Maximum lateral load in forward direction at imposed drift cycle
$V_{max,i}^{-}$	: Maximum lateral load in backward direction at imposed drift cycle
V_u	: Ultimate base shear load at imposed drift cycle
V_y	: Calculated yielding load using initial stifness
$V_{y,1}$	: Calculated yielding load using bilinear approximation with one-slope
$V_{y,2}$	: Calculated yielding load using bilinear approximation with two-slope

1. INTRODUCTION

There are three significant fault zones that can produce severe ground-shaking in Turkey. They are North, East and West Anatolian fault zones. In historical point of view, there were many damaging earthquakes caused by these fault lines occured in Turkey such as Erbaa (1942), Bingöl (1971), Erzurum (1983), Dinar (1995), Adana-Ceyhan (1998), Kocaeli (1999), Erzurum-Aşkale (2004) and Van (2011). All these earthquakes ended up with loss of lives and property markedly. For instance, the catastrophic 1999 Kocaeli and Düzce earthquakes caused loss of tens of thousands of lives and cost more than 16 billion dollars to the Turkish economy as well as 9-13 billion dollars of official estimates for direct damage (Erdik, 2001 and DPT, 1999). It is not surprising that Turkey is likely to have a severe earthquake within a couple of decades and most probably it will happen in the Norhwerstern part of Turkey (Marmara region) whose population is approximatelyo 30 percent of Turkey's population according to seismologic and geologic researches (Uçarkuş, 2010, p. 1 and Parsons, 2004). After seismic shakings, many improvements have been done up to day to prevent any loss due to earthquake ground shaking. The major measure to lessen the effect of earthquake over the towns is to develop modern seismic codes depending upon the researches and apply it properly during the design and construction stages. Although Turkish seismic code has been revised and promulgated recently and existing structures are being reconstructed in the context of "Urban Transformation Law", there are still a great number of buildings that need urgent strengthening and upgrading procedures to mitigate resulting damage because of earthquakes. Moreover, not only does this point creates a problem in Turkey but also it remains a challenging topic in other developing countries.

The terminology related to post-construction phase of structures is a bit confusing. Prior to explaining the purpose of this thesis study, some terms should be clearly stated to understand the gep neral concept. "Upgrading" is defined in ISO 13822 as modifications to an existing structure to improve its structural performance. Also, the term "strengthening" can be described as the number of interventions that may improve one or more seismic response parameters (stiffness, strength, ductility etc.) as a function of the desired structural performance level (Fujita et. al, 2010). It also includes the addition of structural elements or the change of the structural system. Contrary, the repair process can be clarified as the reinstatement of the original characteristics of a damaged section or member and is confined to dealing with the as-built system. Lastly,

rehabilitation is identified as an all-encompassing term that includes concepts of repair, retrofitting, strengthening and weakening that may minimize the vulnerability of building structures to earthquake loading (Di Sarno and Elnashai, 2002, s. 3). Thus, in this study, "upgrading", "strengthening" or "retrofitting" terms can be interpreted as common terms explaining an increase in structural performance of undamaged reinforced concrete frames without any removal or adding of structural members.

It is a fact that re-construction of all vulnerable structures is time-consuming and might not be cost-effective in the long-time process. Especially, an immediate intervention might be required after the damaging natural disasters for both accommodation, serviceability and meeting urgent demands. The vulnerability of a building subjected to an earthquake loading is depended on seismic deficiency of that building (El-Betar, 2016, p.1). To be able to improve the structural responses and lessen the vulnerability of structures under seismic loads, there are conventional and innovative applicable repair or retrofitting methods. When it comes to evaluate existing RC structures, the needs of upgrading or repairing process is further to be considered. What we know from field reconnaissances after severe earthquakes that most of the existing reinforced concrete (RC) structures are prone to be damaged due to the fact that they were not constructed according to the modern seismic codes (Yılmaz and Avşar, 2013). Many of the existing building stocks, which are also called substandard structures, in Europe as well as in developing countries has been designed considering old standards and has little or no consideration of seismic provision and mainly suffers from poor material quality and construction practices (Garcia, Hajirasouliha and Pilakoutas, 2010, p. 3075 and Tapan et al., 2013, p. 610-611). The general structural deficiencies that can led to much damage in these substandard structures in case of earthquake are lacking of joint transverse reinforcements, using low strength concrete and plain re-bars with improper detailing, construction applications contrary to earthquake resistant design principles such as strong beam-weak column phenomenon and several irregularities (Bal et al., 2008 and Del Vecchio et al., 2016, p. 107). As a result, many existing buildings have deficient lateral load resistance, inadequate energy dissipation capacity and can rapidly lose their strength during ground motions (Garcia, Hajirasouliha and Pilakoutas, 2010, p. 3075). The extensive human and economic losses were also observed due to absence of mentioned principles in recent earthquakes (Indonesia and Italy, 2009; Haiti and Chile, 2010; Mexico City, 2017).

As the technology and material science develop, there will be of course new materials and techniques to be used in design and construction stages with the intent of inhibiting any loss. The engineers and manufacturers are in search of producing non-conventional materials providing more advantage in controlling structural performance requirements. In this thesis study, four one-bay and one-storey, 2/3 scaled reinforced concrete frame with no infill were designed and constructed in the laboratory conditions. These RC frames represent the existing substandard RC buildings in developing countries with some common structural deficiencies and obsolete design principles such as strong beam-weak column phenomenon, low strength concrete and plain reinforcements, 90° bended hooks instead of 135°, insufficient amount and spacing of transverse reinforcements. All the frames were tested under displacement controlled quasi-static reversed cyclic loading with or without upgrading methodology. So, three of the RC frames except for the first frame, which was also denoted as reference frame, were upgraded with conventional steel and different Shape Memory Alloy Bars (SMAs) to improve structural response parameters of the substandard RC frames. A mechanism providing the strengthening bars to work under only axial loading was designed and incorporated into the RC frame. Also, ambient vibration measurements were taken from all the specimens before and after the experiments without axial loads and actuator connection. To explore the effectiveness of upgrading procedure in comparison to reference frame and each other, experimental data were analyzed, and analytical model was constructed in SeismoStruct platform. It should be noted that the SeismoStruct structural software was used in both at the pre-design process and post-process by reason of its favorable and simple modelling approach in SMAs. Additionally, all the required material tests were performed in laboratories and the results were presented in the following chapters.

In the last chapter of this thesis study, the numerical results obtained from analytical study and experimental approach were evaluated in terms of strength, stiffness, dissipated energy, ductility, equivalent viscous damping, re-centering property (self centering), strain gages data and ambient vibration results. The purpose of this thesis study is to explore the effectiveness of innovative materials in the upgrading methodology owing to their unique material characteristics by comparing them to conventional materials in order to reduce the imposed damage under the effect of earthquake loading.

2. LITERATURE REVIEW

Within the scope of this study, non-code-conforming RC frames representing existing RC building stocks in developing countries with some shortcomings were upgraded using conventional steel and innovative materials (i.e., SMAs) in a system developed for strengthening procedure. Initially, the starting point of this study is to investigate how the SMAs can contribute to the seismic performance of substandard RC framed structures. To be able to discover this effect, the material characteristics of SMAs should be simply revealed before explaining the literature and studies in detail by drawing a general outline. Also, it is required to show the effectiveness of SMAs over conventional civil engineering materials.

2.1. Shape Memory Alloys

Shape memory alloys (SMAs) are a class of materials with excellent property to remember its original shape. It means that SMAs can return to their undeformed position from large inelastic deformations either by removal of external load (stress-induced transformation) or by means of heating (temperature induced transformation). The former one is called as superelastic effect (SE) and the latter one is called as shape memory effect (SME). SMAs can be referred as smart materials for their distinctive properties and they can be employed in structural design to enhance performance of structures. The SMAs have application potential in many engineering areas due to their extraordinary advantages in energy dissipation capacity, hysteretic damping, excellent fatigue and corrosion resistance, large elastic strain ability compared to conventional materials and lastly re-centering capabilities (Desroches and Smith, 2004, p.416 and Song, Ma and Li, 2006, p.1266). All these features of SMAs provide them to be used in seismic force resistant design and repairing/retrofitting studies. These properties of SMAs are associated with its reversible martensitic transformation (solid-to-solid phase transformation) between a crystallographically more-ordered phase, the austenite, and a crystallographically less-ordered phase, the martensite (Fugazza, 2005, p. 1). The physical behavior of SMAs is a function of stress, strain and temperature (Wilson and Wesolowsky, 2005, p. 572). The phase transformations are characterized by four transition temperatures: M_f, M_s, A_f and A_s, M refers to martensitic and A to austenitic state phases. Also, f and s refer to the finish and start temperatures of the transformation process (Lobo, Almeida and Guerreiro, 2015, p. 776). They are used in the transformation

process to explain the behavior of alloys under temperature-induced or stress-induced effects. At its low tempeture phase, the alloys in martensite form are stable and they show shape memory effect (also referred to as 'one-way shape memory effect' or 'pseudoplasticity'). This effect is illustrated in Figure 2.1. There are two martensite forms depending on crystal orientation direction, twinned and detwinned martensite. In its stress-free state, if the temperature is below the M_f, the martensite SMA is in its twinned martensite phase. As the tewmperature is risen it will transform first to a state where both martensite and austenite exist together, and finally to a fully austenite phase (Wilson and Wesolowsky, 2005, p. 572). Besides this, if the critical level of stress is induced to material the alloy transfroms to detwinned martensite phase and maintains this phase upon removal of load. Then, it can return its initial shape after increasing the temperature above the A_f. Next, the material transforms to first twinned martensite phase without residual deformation by a subsequent cooling. This cyclic transformation process with the temperature or stress applied to martensite SMAs can provide fully shape recovery.
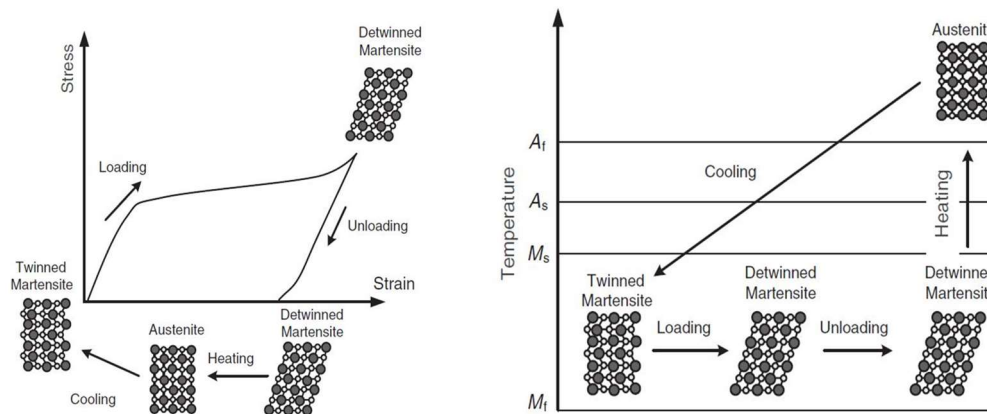
Figure 2.1. *Shape memory effect (Ozbulut, Hurlebaus and Desroches, 2011, p. 1533)*

Another essential phase transformation is superelasticity (also reffered to as 'two-way memory effect' or 'psuedoelasticity') where the transformation from austenite to martensite happens only by applying stress excitation without changing the temperature (Figure 2.2). In this case, the material starts the transformation in the form of austenite. The forward transformation occurs from austenite to detwinned martensite by applying a load and reverse transformation takes place to austenite phase by a removal of loading. As a result, a shape recovery is completed in flag-shaped stress-strain loops. Note that all

transformation processes create a hysteretic cycle. The Figure 2.3 illustrates the general behavior of superelastic SMAs under the applied loading.
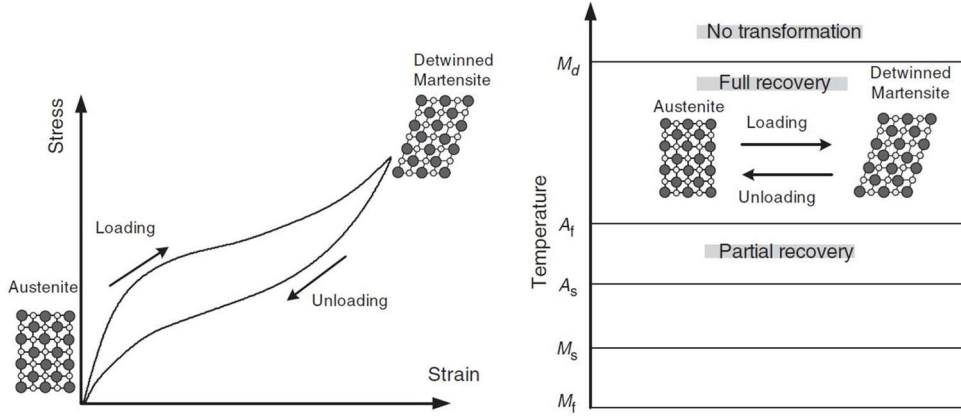
Figure 2.2. *Superelastic effect (Ozbulut, Hurlebaus and Desroches, 2011, p. 1533)*
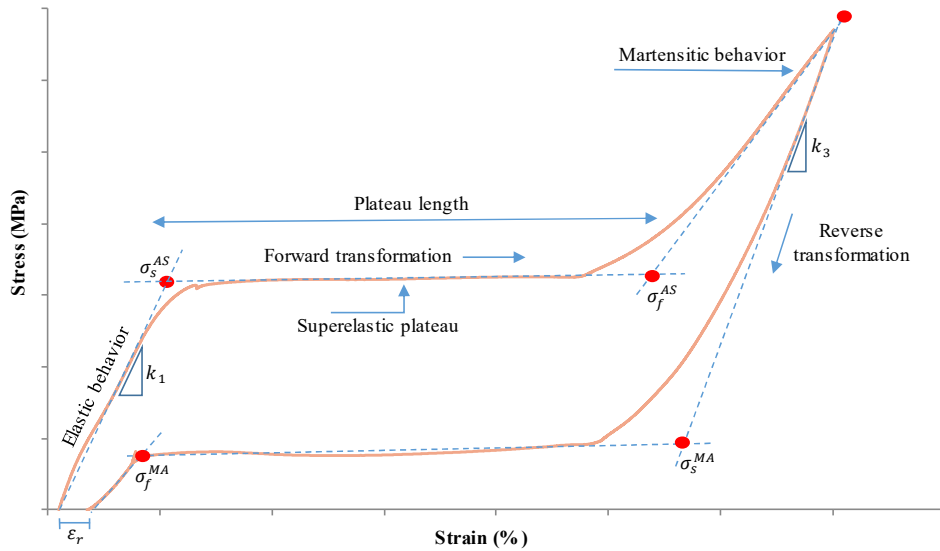
Figure 2.3. *Representative stress vs. strain relationship of SMA materials*

The most cited materials used in composition of SMAs are nickel-titanium (NiTi) and copper (Cu) based alloys. The number of studies conducted on civil engineering applications with NiTi SMAs have been focused on more than Cu-based alloys since NiTi have more advantages in offering re-centering capabilities, excellent corrosion resistance, growing damping capacity and controlling force transmissions between structural elements when structures are exposed to strong ground motions (Araki et. al, 2011, p. 107). It is the fact that these properties do not only reflect their potential usage in applications, but also the cost of row materials, the required processing, machining and heat treatment are further properties need to be considered. Nevertheless, NiTi has the higher material cost compared to Cu-based alloys and has the difficulties in machining, threading and drilling. Thus, any material should be converted into a specialized shape or processed in order to benefit from its advantages. Cu-based SMAs have been investigating in seismic resistant design as an alternative of NiTi SMAs (Araki et. al, 2011, p. 107). In this study, NiTi and CuAlMn SMA bars were employed in strengthening strategy in order to enhance the seismic performance of substandard RC frames. The SMA bars were all in austenite forms in the room temperature and the superelastic behavior was observed in both axial tests and experiments. Two kinds of SE SMAs were utilized in construction of RC frames with the aim of investigating their own advantages and comparison among themselves. Furthermore, conventional steel bars were also used in the upgrading methodology. The literature review of the seismic applications with SMAs are summarized in the following chapters based on the type of SMAs.

In the developing countries, the researchers are in search of engaging new materials to use in application considering revised seismic codes with the intent of strengthening or repairing procedures (Thermou and Elnashai, 2006). The retrofitting methodologies can be classified as conventional or innovative. Owing to the progress and advances in technology, several innovative methods have been developed for retrofitting strategies. For instance, Carbon Fiber-Reinforced Polymer (CFRP) and base isolation techniques can be included in innovative applications. But, there are still conventional methods applied to structures to increase the seismic performance such as addition of shear walls and infills, addition of steel braces and RC or steel jacketing. These methods can be applied globally or locally to the structure according to the aim of strengthening.

Almeida et. al (2017) investigated a typical existing RC three-storey school building, which does not satisfy modern earthquake codes, with steel Buckling Restrained

Braces (BRBs). They conducted non-linear static and dynamic numerical analyses on the school building to show the effect of the steel braces. Their study indicated that the BRBs, which can be grouped as passive control systems, are promising to enhance the seismic performance of existing RC framed structures.

Melkumyan (2013) retrofitted three existing buildings, which are school, apartment and historical buildings, in the field by using the base isolation technique. He described the structural retrofitting concept and presented the results obtained from earthquake response analysis for two cases. In this study, the overall cost analysis was performed to compare the innovative base isolation methods with the conventional ones. According to the results, the buildings retrofitted with seismic isolation is more reliable than the buildings retrofitted with conventional strengthening. In cost analysis, it is figured out that the cost of traditional retrofitting methods are 2.5 times more in average compared to innovative strategies.

Lee et. al (2003) studied on the effectiveness of carbon fiber sheets (CFS) to retrofit RC columns damaged by several degrees of rebar corrosion. Their study included an experimental procedure in six different specimen configurations and they applied horizontal reverse cyclic loading to the RC columns to explore the seismic behavior of structural members with carbon fiber sheets. At the end of the tests, they pointed out that the CFSs are exceedingly successfull in improving the shear strength as well as improving the ductility of columns.

Di Sarno et. al (2006) conducted experimental studies on retrofitting of framed structures by incorporating the stainless steels (SSs) into the structural system. They used the SSs with the aim of seismic retrofitting in concentrically braced frames (CBFs) and moment resisting frames (MRFs). Inelastic static and dynamic analysis were performed to check out the feasibility of utilizing SSs throughout finite element program. The dynamic analysis was carried out by selecting the near and far-field records to compare the seismic performance with different frequency content. According to the results of this study, SSs exhibited a great performance on enhancing the plastic deformation and energy absorbing capacity. Also, SSs significantly reduced the shear demand on the framed structures by 25-30% in case of using it in both columns (MRFs) and braced-columns (CBFs).

2.2. NiTi Based Shape Memory Alloys

Speicher et al. (2011) tested steel beam-column connection utilizing ordinary steel tendons, martensitic and SE NiTi tendons and finally SE NiTi tendons combined with low-strength aluminum bars. A quasi-static loading was applied to the specimens taking the drift angle as basis parameter for this loading protocol. The authors also created a connection model in OpenSEES to validate the experimental results. As a conclusion of this study, the superelastic NiTi tendons showed significant reduction in residual deformations and they have an ability of fully re-centering the connection at drift levels below 1% drift. Furthermore, a recovery was observed in the connection by 85% of its deformation after being cycled to 5% drift. Another emphasizing point of this study is that the martensitic NiTi tendons were not suitable for such an experiment. It should also be noted that the OpenSEES model is compatible with experimental data, yet it underpredicts the residual deformation for small and large rotations as well as overestimating the stiffness and strength due to its incompetence in catching the behavior in transition zone.

Tazard and Saiidi (2014, p. 04014197) studied on the mechanical properties of NiTi based superelastic (SE) SMAs and then they searched out the effect of each mechanical parameters on the seismic behavior of a SMA-reinforced concrete bridge column. Beside this, they proposed a SMA-model to determine the range for mechanical properties and they engaged the proposed reinforcing model to simulate the results obtained from their experimental tests. The axial tension test results of both reinforcing steel and SMA bars are given in Figure 2.4. The outcome of finite element analysis with the proposed specifications was in good agreement with the test data. This study also showed that the change in mechanical properties of NiTi SE SMA do not essentially influence the lateral force-displacement and moment-curvature relationships of SMA reinforced columns.
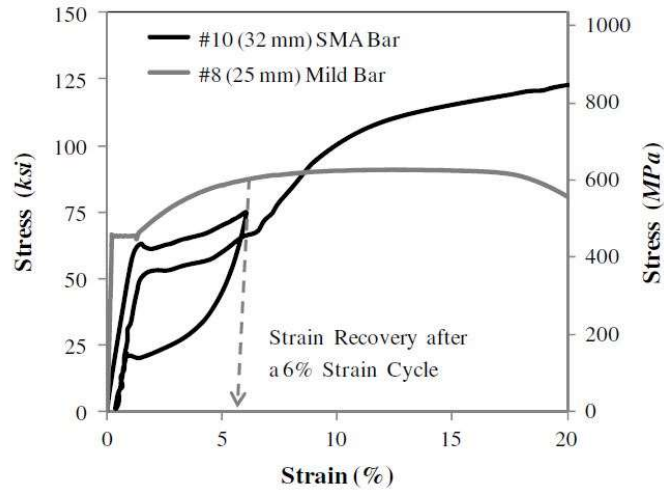
Figure 2.4. *Tension test results of reinforcing SMA and steel (Tazard and Saiidi, 2015)*

Shin and Andrawes (2010, p. 1282) performed an experimental test by using the active-confinement method to the 1/3-scaled RC columns. They used two alternative materials for confinement, one of them is thermally triggered recovery stress of prestrained SMA spirals and the another one is glass fiber-reinforced polymer (GFRP)/epoxy jacket. They conducted totally four experiments and the plastic hinge region of single column was wrapped with 2 mm-diameter NiTiNb (Nickel-Titanium-Niobium) prestrained SMAs, GFRP and hybrid confining with two of them, respectively. The results of this study indicated that the SMA and SMA/GFRP confining offered slight increment in strength and noticeable increment in flexural ductility and ultimate drift capacity compared to the reference specimen while the GFRP-wrapped specimen exhibited only a moderate improvement in drift capacity and ductility. Damage views of tested column ends are shown in Figure 2.5. Also, SMA confining technique has more practical than the GFRP application as well as its structural response benefits. Though the successful results with SMA confining, the authors agree with the idea that there is an important lack of information about the long-term behavior of these SMA spirals under real environmental conditions.
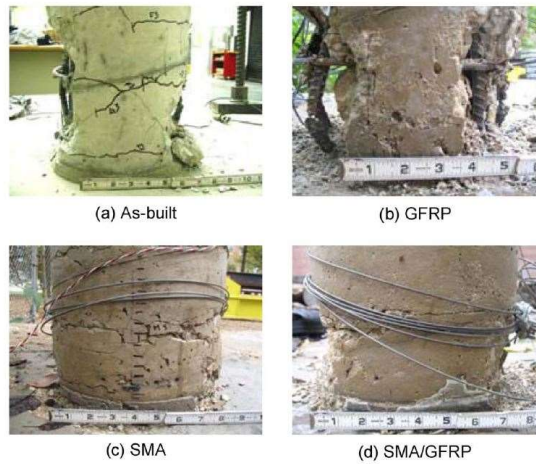
Figure 2.5. *Damage view of column bottom ends (Shin and Andrawes, 2011, p. 1289)*

Youssef et. al (2008, p. 1205) used hot-rolled NiTi SMA in the beam-column joint as an alternative rebar to the conventional steel. They constructed two 3/4-scaled beam-column joints satisfying current seismic codes and then tested them under reversed cyclic loading. The main difference between the two specimens is to be used SE NiTi SMA bar, which has 20.6 mm diameter and 450 mm long, in the plastic hinge region of beam-column joint for the second specimen. They also developed a mechanical coupler to connect the conventional steel with NiTi (Figure 2.6). As a result of the study, they obtained flag-shaped force-displacement curve due to the flag-shaped hysteretic stress-strain curve of SE SMA re-bar. This caused negligible residual displacements in the SE SMA-RC beam-column joint compared to as-built specimen. Moreover, these small residual values can require less repair time and cost. Additionally, the plastic hinge region was strongly relocated away from the column face whereas the plastic hinge developed at the face of the column in the steel-RC beam-column joint.

(a) View of mechanical coupler   (b) Test setup for coupler   (c) Reinforcement view of specimen
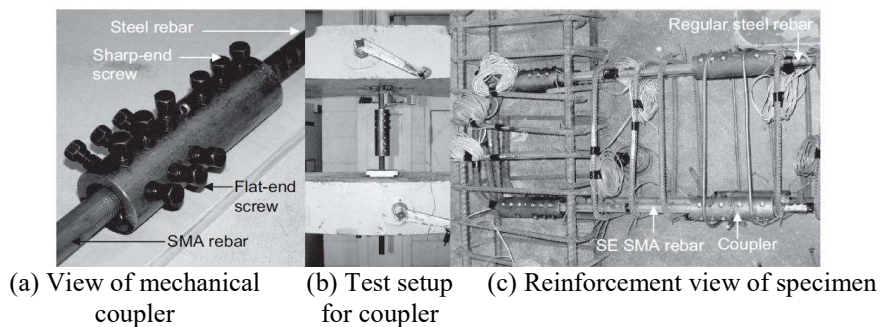
Figure 2.6. *Experimental setup (Youssef et. al, 2008, p. 1210)*

Dolce et. al (2005, p. 1687) conducted shaking table tests on a three-storey, two-bay RC plane frame, scaled down by a factor of 3.3. The structure was detailed such that a weak column-strong beam collapse mechanicsm had to be expected. In this study, the authors utilized two different types of energy dissipating and re-centering braces, which are steel plates and pre-tensioned NiTi wires, to improve the seismic performance of RC frame. They used three different configurations of SMA energy dissipating braces analytically and experimentally; austenite SE NiTi wires, martensite NiTi bars and lastly SMA with no re-centering property. Furthermore, they considered the conventional frame with and without masonry infilled panels conditions to explore the real effectiveness of the braces. Finally, the study pointed out that the SMA braces exhibit a performance comparable to those currently used in construction. Actually, the SMA and steel braced models caused similar responses under earthquake loading. The SMAs have an extremely feature of low fatigue resistance and there is no need to substitute it after shaking. According to the result of this study, the re-centering ability of SMA materials can be fully engaged in structural system by modifying the current seismic design philosophy since it focuses on minimizing the ductility demand whereas SMA meets the high ductility demands in RC members.

Saiidi et. al (2007, p. 454) investigated the effect of superelastic NiTi when used as reinforcement in concrete simply supported beam. The capability of SE NiTi to return it original position after deformation and thereby reducing the plastic deformations of concrete beam was examined experimentally. The SE NiTi rods were used as tensile reinforcement in the maximum moment region of concrete beam. In addition, the concrete strength was obtained as 40 MPa on the day of testing and yield strength of steel was determined as 439 MPa. Two different diameters of NiTi rods with the threads at the ends, 9.53 mm and 12.57 mm, were utilized in this study and the authors also made an analytical study with different material combinations with NiTi, high-strength steel and CFRP. The outcome of this study explored that the NiTi bars exhibited fully recovery after large strain values. In the experiments, the average residual deformations in the NiTi reinforced beams was 20% of that of steel reinforced beams. However, the stiffness of NiTi reinforced beams was 60% lower than the stiffness of steel-reinforced beams due to lower modulus elasticity of NiTi. Finally, the analytical study figured out that a combination of NiTi and high-strength steel could be an alternative member because of acceptable stiffness and the partial recovery of deformations.

Gao et. al (2016, p. 055030) contributed experimental studies on SMA bracing in the one-bay one-storey steel-based lateral force resisting frame. They used SE NiTi in the form of a ring connected to four tension-only cable assemblies (Figure 2.7). The full-scale quasi-static cyclic loading test and then finite element analysis were performed to investigate the performance of bracing with SMA. According to the results of this study, a ring-shaped SMA showed a favorable energy dissipation and higher lateral strength. Up to 1% story-drift, SMA ring demonstrated a typical flag-shaped hysteretic behavior and small residual deformations while the cables had almost elastic behavior. This flag-shaped behavior was observed in all three force-deformation relationships of components; cable, ring and system. Further, the finite element analysis results are compatible with the experiment excluding the residual deformations values. In summary, the SMA ring system exhibited highest lateral strength and energy dissipation. The self-centering of the suggested system was not fully succeeded due to yielding of sub-components in the cable assemblies and yielding of some part of the SMA ring. The authors emphasized that more researches are required to understand the behavior of SMAs under high strain rate and thermal conditions.

(a) *SMA ring*   (b) *Cross-braced system depending on SMA ring*
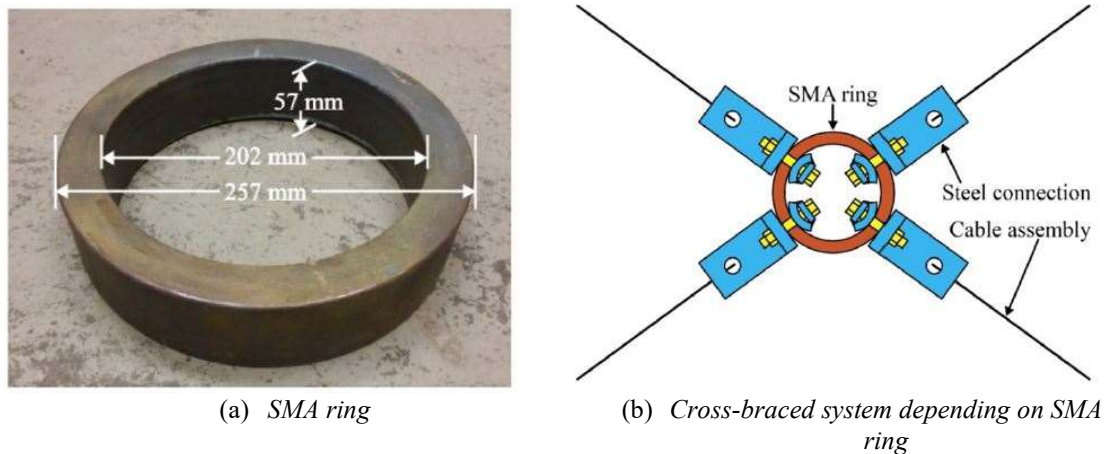
Figure 2.7. *SMA based bracing system (Gao et al., 2016)*

Ozbulut and Hurlebaus (2010) investigated the effect of superelastic NiTi SMAs in the base isolation system with the purpose of protecting highway bridges against near-field earthquakes. They called the device as SMA/rubber-based (SRB) isolation system and presented nonlinear time-history analysis on a three-span continuous bridge model with laminated rubber bearings and an auxiliary SMA device (Figure 2.8). Also, they used

13

mechanical properties of NiTi SMA obtained from axial test of 1.5 mm NiTi wire. In this study, the authors also created a neuro-fuzzy model to get the rate and temperature dependent behavior of NiTi. As a consequence of this study, lower displacement values of SMA device implying shorter wire lengths for a fixed %1 forward transformation strain value implies stiffer SMA and so the deck acceleration and normalized base shear increase by about 30% and 39%, respectively. The authors also figured out that the temperature dependent behavior of SMAs are effective in the response parameters and it can not be neglected for SMA-based isolated structures. The main barrier to use SMA in such a system can be high cost of the material.
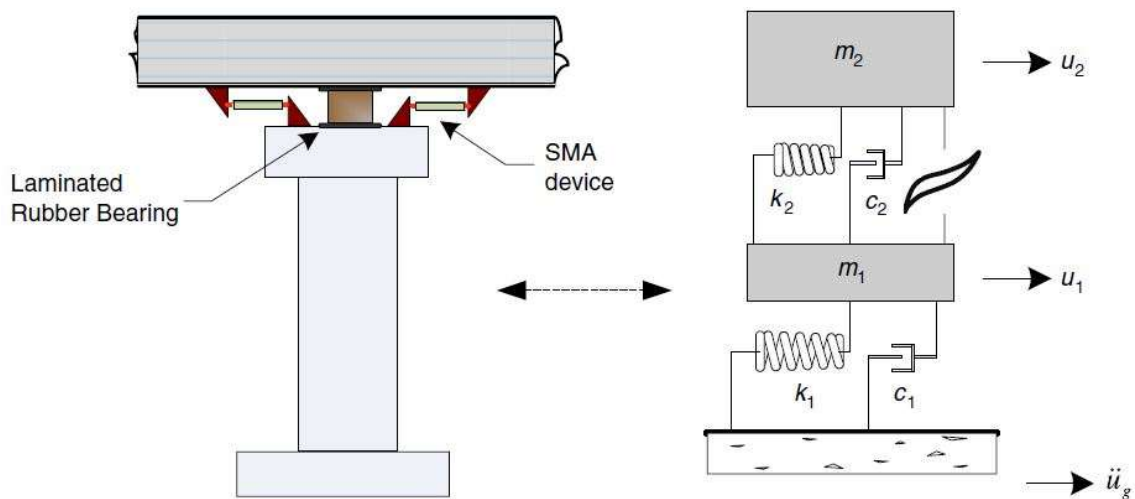
Figure 2.8. *Model of an isolated bridge with an SMA/rubber isolation system (Ozbulut and Hurlebaus, 2010)*

Ghassemieh et. al (2012) employed NiTi SMAs in two different material form and they used the NiTi SMAs as reinforcement with conventional steel re-bars in controlling concrete shear wall. They consisted of finite element modelling in Abaqus to assess the behavior of the strucrures exposed to seismic excitation. In this study, two different types of concrete shear wall, one reinforced with pre-tensioned SE SMA re-bars and the another one reinforced with ordinary SMA re-bars having shape memory effect through heating, were utilized. The mechanical and physical features of concrete shear wall were very similar to the experimental model used by Ghorbani-Renani et. al (2009). The SMA reinforcements with two different characterizations were used only in the boundary area. As a conclusion, the SMA-reinforced wall reached more ultimate lateral load and recovered its plastic deformations with a decreasing stiffness if the percentage of SMA

used in the wall is not below 50%. The critical decision should be made on the percentage of steel and SMA re-bars. In addition to this, the SMA re-bars with shape memory effect caused a decline in strength, stiffness and residual displacement. Moreover, they stated that the using pre-tensioned SMA in shear wall resulted in much stiffer and stronger structural performance than ordinary SMA re-bars. The important conclusion is that using SMA in seismic design and rehabilitation might reduce the repair cost significantly and the structure might serve even after a serious ground motion.

Li et al. (2007) experimented with simple RC beams strengthened by CFRP plates in conjunction with NiTi SMA wires. The application of this collective behavior was investigated through experiments and numerical study depending on the nonlinear finite element modelling in ABAQUS. In this study, the authors used SMA wire having diameter of 2 mm. The simply-supported beams were bonded with CFRP plates in the mid-span region and the SMA wires, which show shape memory effect through heating, were embedded in the construction stage in tension zone only. The experiments were performed considering three specimen types; reference specimen, a specimen with embedded and pre-tensioned SMA wires and lastly a specimen retrofitted with CFRP plates with embedded and pre-tensioned SMA wires. The authors applied 14 A electrical current to SMA wires via cables. Eventually, the residual deformations were significantly reduced through heating of SMA wires because of recovery stress of NiTi wires (Figure 2.9). This method can be very successful in rapid repairing of damaged structures with little complexity.

(a) Before activation of SMA   (b) After activation of SMA
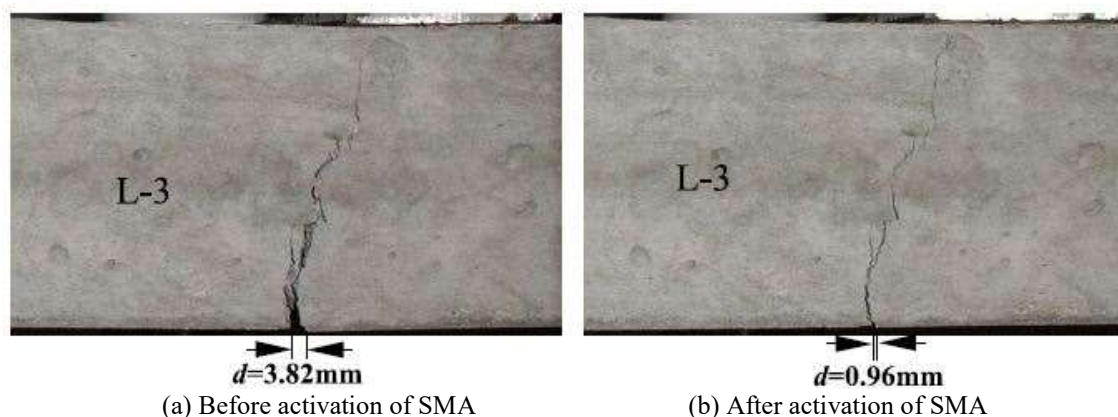
Figure 2.9. *A beam specimen with SMA wires (Li et al., 2007)*

Johnson et al. (2008) constructed large scale testing study in laboratory conditions to explore the effect of superelastic NiTi in retrofitting of bridges through shake table test. The SMA materials are worth to use in seismic applications due to advantages in hysteretic damping, strain hardening at large strains and the formation of a stress-plateau limiting force transmission. They used SMA materials as a restrainer cable in experiments with the aim of seismic retrofitting. Also, the steel restrainers were used for comparison purposes. A multiple-frame concrete box girder bridge whose dimensions depend on the superstructure dimensions of typical Caltrans bridges was used in the experiments. In addition, they used elastomeric bearings supporting the box girder cells. The SMA-restrainer cable with 84-wire and 130-wire made up of 0.584 mm diameter was utilized in close-up form. The shake table test performed with five different level of input ground motion within the range of 0.05g and 0.25g in SMA cable testing. Additionally, the authors created an analytical model in OpenSees to match the experimental results. In conclusion, the SMA restrainers were successful compared to that of conventional steel restrainer in limiting relative hinge displacement. Besides, the SMA restrainer displayed less residual strain after the tests and the system tolerated many cycles of loading with slight stiffness and stiffness degradation.

A remarkable study related to repairing of shear walls with steel and NiTi bars carried out by Cortés-Puentes et al. (2018). The repairing methodology involves removing severely damaged concrete, replacing ruptured and buckled reinforcing steel and shortening of the SMA bars (due to visible buckling) in the boundary zone from the specimens, which were reinforced with conventional steel and NiTi SMA bars, tested previously under lateral cyclic loading by Abdulridha and Palermo (2017). High strength and self consolidating concrete was used after the removal of damaged concrete. They also prevented out-of-plane displacements by constructing lateral supporting frame connected to top of the beam. At the end of the experiments, they pointed out that both the SMA-reinforced and the steel-reinforced slender shear walls were serviceable after repairing procedure (Figure 2.10). The SMA-reinforced walls exhibited a better performance in recovering the residual displacements corresponding to more than 80% recovery capacity up to 2% drift ratio whereas this ratio was around 40% for steel-reinfoced wall. Generally, this study explored that the repairing strategy enhanced some structural responses such as cracking, energy dissipation, rotation and shear strain.

(a) *Repaired steel-reinforced wall*   (b) *Repaired SMA-reinforced wall*

Figure 2.10. *Condition of walls at the end of testing (Cortés-Puentes et al. 2018)*

2.3. Copper-Aluminum (CuAl) Based Shape Memory Alloys

Shrestha et. al (2013) presented a study to explore the effectiveness of CuAlMn superelastic bars when used as reinforcement in concrete beams. They indicated that CuAlMn has low material cost and capability to recover from large strains and high machinability. In this study, a four-point reverse cyclic bending test were conducted on a 1/3-scaled concrete beam. Then, the material tests for both conventional steel and SE CuAlMn were presented. Moreover, one of the specimen was reinforced in the mid-span with CuAlMn bars having 4 mm diameter. The experiments showed that the crack width upon unloading was quite satisfactory in the specimen reinforced with CuAlMn compared to reference due to the re-centering capability. These small cracks can be effectively healed with various solutions such as epoxy injection. The authors also emphasized that the large scaled experiments are required for more reliable and practical applications.

Araki et. al (2016) figured out the potential usage of CuAlMn superelastic bars as damping braced system in a 1/3-scaled one-bay one-storey steel frame. The steel frame was braced with conventional steel and CuAlMn bars for comparison purposes. The experiments were carried out by applying both shaking table test with a frequency of 1.5 Hz and quasi-static component test. A view of experimental system is given in Figure 2.11. Accelerometers were also instrumented to the system. Besides, they extended the study with the finite element model to confirm the experiment by considering near-fault ground motion data in the analysis. A large diameter CuAlMn bars with 10 mm were used in the system as tension braces. The structural response of the proposed SMA braces was

successful due to superelastic characteristic of SMA and also in preventing pinching. Finally, the response of numerical model was also verified the effectiveness CuAlMn bars as tension bracing. The strains in SMA bars and the demand for the drift angle of the steel frame was found within a satisfactory range (strain in SMA bars and drift angle are less than 5% and 0.02 rad, respectively).
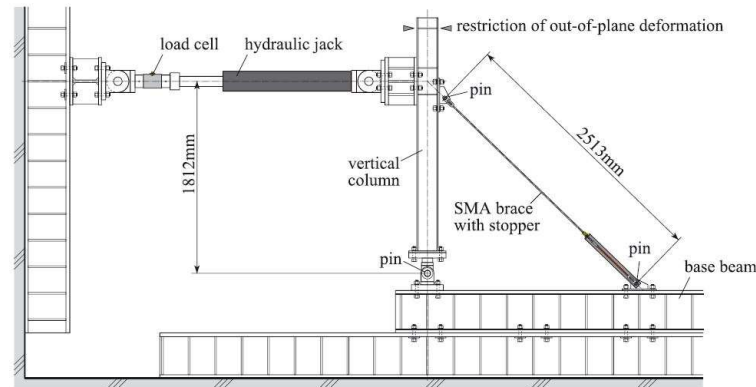
Figure 2.11. *An experimental system (Araki et al., 2015)*

Casciati et al. (2007) introduced extensive research related to new and innovative base isolator. It consists of two disks, one vertical cylinder with an upper enlargement sustained by three horizontal cantilevers and at least three inclined CuAlBe SMA bars having diameter of 3.5 mm and length of greater than equal to 20 cm (Figure 2.12). They implemented standard shaking table test with different amplitudes to the prototype of new isolator in order to determine the dynamic characteristics of structural model. The SMA bars provided stiffness against low intensity excitations and showed re-centering ability. In addition to these, the bars dissipated the energy during the motion and the force-displacement loops are wide due to superelastic behavior. In conclusion, the authors emphasized that the optimization should be carried out by trying different SMA bars and geometric characteristics
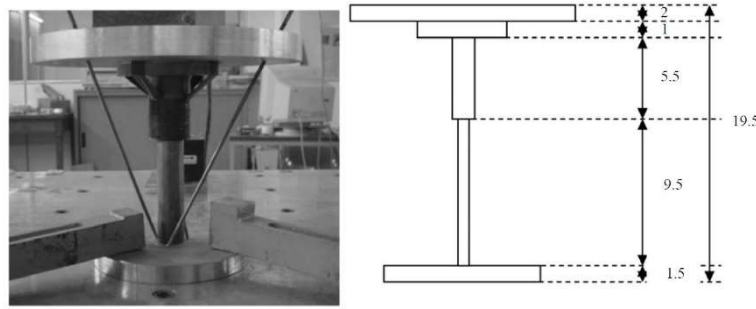
Figure 2.12. *Base isolator prototype (Casciati et al., 2007)*

Hosseini et al. (2015) proposed a new bridge column design considering the engineering cementitious composites (ECC) and CuAlMn superelastic alloy bars (SEAs). To prevent the damage occurred in bridge columns and permanent deformations, they preferred to use ECC and CuAlMn SEA bars. A total of six columns were constructed and they were subjected to seismic loading. The reasons for using the CuAlMn SEAs in this study instead of popular NiTi SE SMAs are the excellent superelasticity with nearly zero permanent deformation, low material cost and easily machineability. The SE CuAlMn SMA bars have the diameter of 9.5 mm and 11.18 mm in the mid-section and at the end, respectively with a total length of 250 mm. Here, the authors also applied a pre-tensioning (three tensile strain cycles) to the CuAlMn bars to diminish the effect of microstructural slip (Figure 2.13). The aim of considering six different configurations in the bridge column design was to determine the effectiveness of mentioned SEAs. A quasi-static reversed cyclic loading was applied to the specimen at the top. At the end of the test, wide cracks and concrete spalling were observed at 5% drift ratio. The columns can able to recover its 91% plastic deformations which the conventional column exhibited at %7 drift ratio if all the steel rebars in the plastic hinge region of the columns are replaced with CuAlMn bars. Additionally, the stiffness of the columns using ECC, CuAlMn SEA bars, or both was lower than the conventional ones due to lower elastic modulus of SEAs.
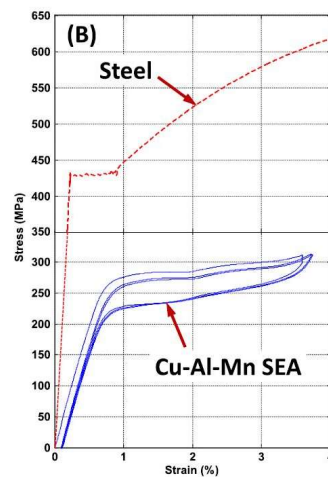
| (a) Test setup | (b) Stress-strain relations and comparison with steel reinforcement |

Figure 2.13. *Training of CuAlMn SMA bars (Hosseini et al., 2015)*

2.4. Combined Studies for Nickel and Copper Based SMAs

Shretstha et. al (2015) constructed an analytical model in OpenSees to validate the experiment carried out by Cruz and Saiidi (2011 and 2012). In the experiment, Cruz and Saiidi showed that the seismic damage could have mitigated using the innovative materials in plastic hinge region of columns and residual drifts were not important in the bridge piers. The authors of this study investigated the applicability of numerous advanced materials and their combinations, which are Self-Centering NiTi and CuAlMn as well as engineering cementitious composites (ECC), to discover the earthquake performance of five different kinds of bridges with different reinforcement details and under several near-fault earthquake records. The model was a four-span structure supported on two-column piers and seat-type abutments. Based on SE SMA combined with ECC, post-tensioned columns and columns with built-in elastomeric rubber pads models, the conclusion of this study is that the SE SMA materials are successful in providing considerably better response with minimum damage to the RC elements and superior re-centering ability with a residual drift below the limit of 1% drift ratio for all scaled ground-motions. The authors also emphasized that CuAlMn SE SMA bars with the developments of cost-effective and easily machinable ways are likely to offer more attractive methods to bridge engineers.

Zafar and Andrawes (2012) searched out the efficacy of SMA-FRP bars when used in RC moment resisting frame as an alternative reinforcement to conventional steel bars.

In this study, it is emphasized that FRP does not provide sufficient ductility and energy dissipation to the structure under seismic events. The authors therefore accounted for an analytical model in OpenSees for 2D three- storey one-bay and six-storey two-bay RC moment resisting frames (MRFs) to explore the behavior of steel, GFRP and SMA-FRP composite reinforcement (Figure 2.14). An incremental dynamic analysis (IDA) was preferred and four selected ground motions was applied to the structures to evaluate the variation in response. It was found that the steel-reinforced RC MRFs have more energy dissipation capacity and higher initial stiffness. Nonetheless, the resiudal inter-storey drift ratio of steel-reinforced frame was 84% and 62% greater than SMA-FRP and GFRP reinforced frames. In addition, frame reinforced with GFRP experienced the least value of ground motion intensity and it failed in all the cases at an earlier step of IDA compared to other models. As a conclusion of this study, it is possible to use of SMA-FRP rebars in plastic hinge regions of MRFs since it improves the energy dissipation and ductility capacity while reducing the residual drifts.
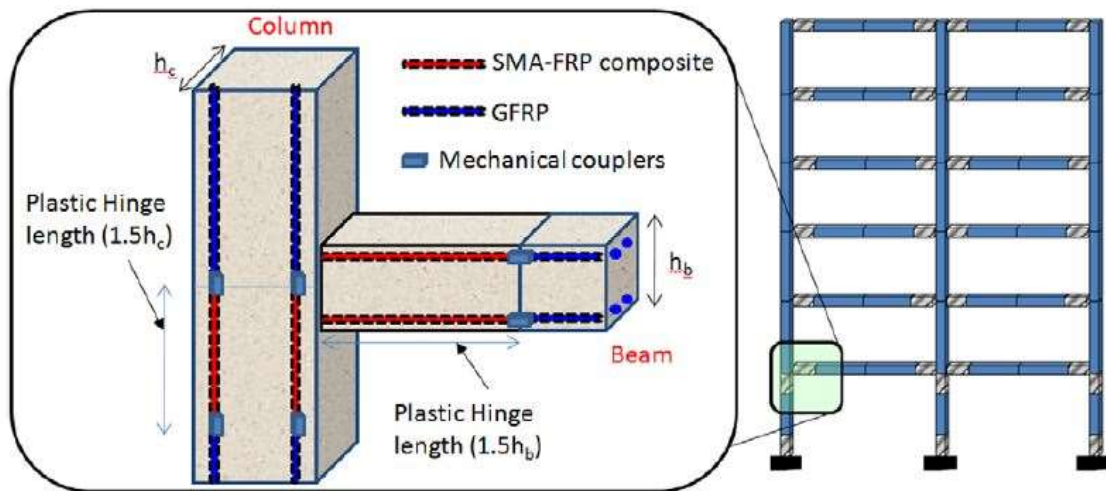
Figure 2.14. *Use of SMA-GFRP composite in beam plastic hinge zone (Zafar and Andrawes, 2012)*

3. EXPERIMENTAL PROCEDURE

The seismic upgrading of the reinforced concrete members, which does not satisfy the requirements specified in the current seismic codes, have been always a critical discussion in the structural engineering area to avoid the severe damage due to earthquake ground shaking. To put it another way, we need to some new technologies for substandard buildings to keep away from loss of lives and property. The researchers have been trying to revise the codes for new structures to be constructed, but at the same time, the number of existing RC structures are still at risk because of their under-designed conditions. In addition to deficiencies observed in the existing RC framed buildings, they were also built without any engineering and control services. Needless to say that, the way to minimize the existing risk in the structures is to either re-construction or retrofitting methods. Re-construction of all vulnerable structures are not possible due to time limitations and cost effectiveness. In this experimental study, an innovative upgrading technique with two different type of superelastic shape memory alloy bars, NiTi and CuAlMn, as well as conventional steel bars was proposed for substandard RC framed structures. To be able to represent the existing RC buildings properly, the literature was analyzed in detail and the design and construction policies were determined. The focus of this study is to search out the seismic behavior of non-code-conforming RC frames retrofitted with conventional and innovative materials under the constant axial load and reversed cyclic lateral loading experimentally and analytically. In the present study, four 2/3-scaled RC frames with no infill were constructed in the Structural Engineering Laboratory of Anadolu University, Department of Civil Engineering. The aspect ratio of the frames, which is the ratio of the frame height (h) to its width (L), is 0.67. All constructed frames are similar to each other in terms of their geometric details and material properties. The only difference among the frames is the materials used to upgrade the seismic performance of the frames. The denotations to be used in the following chapters and upgrading materials for specimens are given in Table 3.1.

Table 3.1. *Denotations and upgrading materials for specimens*

Denotations	Test no.	Upgrading material
G1-1-Reference	1	N/A
G1-2-Steel	2	Conventional steel bars
G1-3-CuAlMn	3	SE CuAlMn SMA bars
G1-4-NiTi	4	SE NiTi SMA bars

3.1. Frame Details

The reinforced concrete frames, which represent seismically vulnerable the buildings to seismic damage due to improper structural design, were constructed with one-bay and one-storey in 2/3-scaled conditions due to the limited laboratory facilities. All structural members were designed and built such that they are representative of existing RC framed buildings in the building stock of Turkey. The following old-fashioned principles, which do not satisfy the modern seismic code requirements, were taken into account in the design philosopy;

- Poor material properties (low concrete strength and plain re-bars)
- Strong beam – weak column phenomena
- Plain re-bars not satisfying the code requirements regarding the minimum amount and spacing criteria
- 90° bended hooks at the both ends of the stirrups instead of 135°
- No confinement zones at beam and column ends

The above conditions were observed in the field investigations after the damaging earthquakes. Therefore, these criteria violate the fundamental principles enforced by modern earthquake codes. The views of designed and constructed substandard RC frames are given in Figure 3.1 and Figure 3.2. The yellow rectangular hooks in the figures helped us to lift and transport the frame in laboratory via a crane.

(a) South-west view   (b) Front view
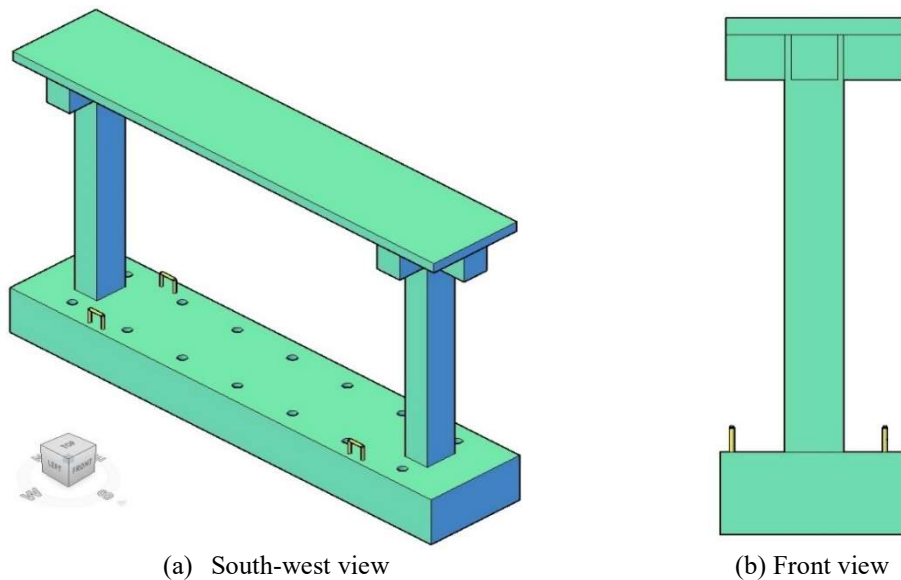
Figure 3.1. *Frame views*
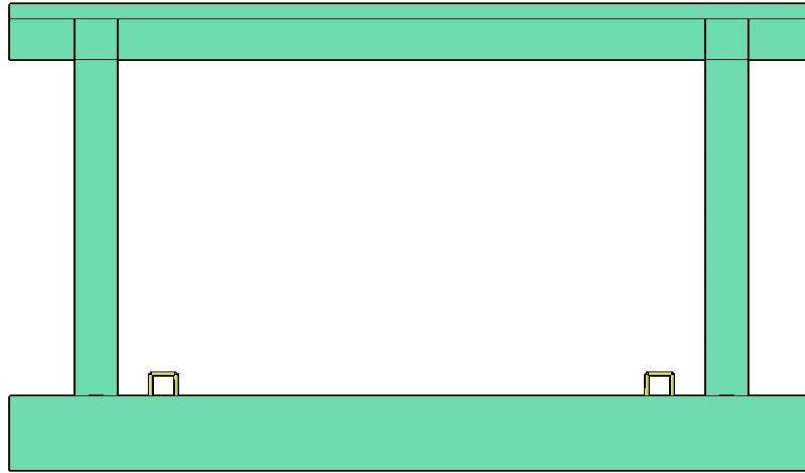
Figure 3.2. *Side view of the frame*

3.1.1. Cross-sectional details

Before constructing the frames, the most appropriate RC beam and column sections were chosen by analyzing them in XTRACT program to check the proper design conditions. In deciding the geometric dimensions and reinforcement details of RC sections, it is aimed to reflect the properties detected in existing substandard RC buildings. In addition, the laboratory conditions and the capacity of actuator is also one of the other key factors in deciding the frame sections and dimensions. Various configurations in reinforcement arrangement and section dimensions are taken into account to make final decision. There were actually two types of pre-conditions; the plastic moment capacity of the beam member should be higher than the column members and the structural members should not tend to show shear-critical behavior. In TEC (2007), it is enforced that the plastic moment capacity of columns should be higher than the plastic moment capacity of beams by 20% at the joint. Considering this rule, the beam is designed such that its moment capacity is at least 20% greater than the columns. By this way, the experimental frame to be tested can be non-code-conforming according to TEC (2007).

Moment-curvature analysis is performed in XTRACT program in pushing and pulling loading directions and in proper coordinate axis under consideration. Ten percent of the axial load capacity of the column member is applied to the column sections in the analysis, which is the actual axial load level that can be applied in the real tests. Axial

24

load is not applied to the beam section. Section views of the column and beam members are given in Figure 3.3. As it is shown, the XTRACT program uses the fibre-based section modelling.

Ø8 (Slab longitudinal bars)   Ø12 (Beam core longitudinal bars)

Ø8/150 (Beam stirrups)

Ø12 (Column longitudinal bars)
Ø8/150 (Column stirrups)

(a) T-shaped beam section
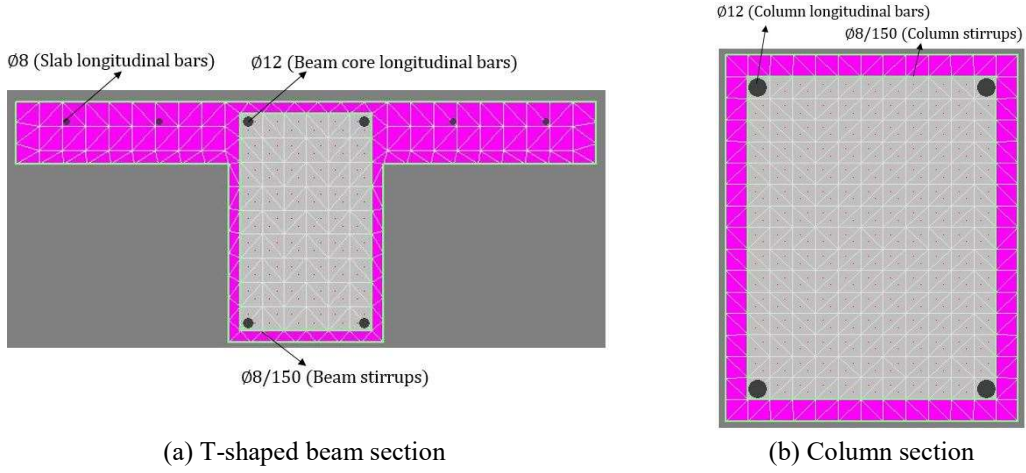
(b) Column section

Figure 3.3. *The beam and column sections in XTRACT*
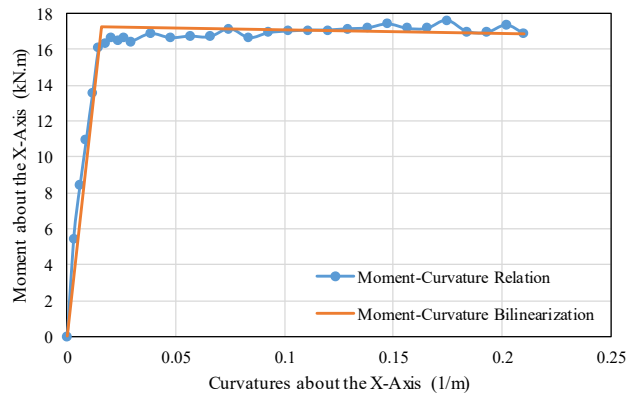
Figure 3.4. *Moment-curvature analysis of the column section*
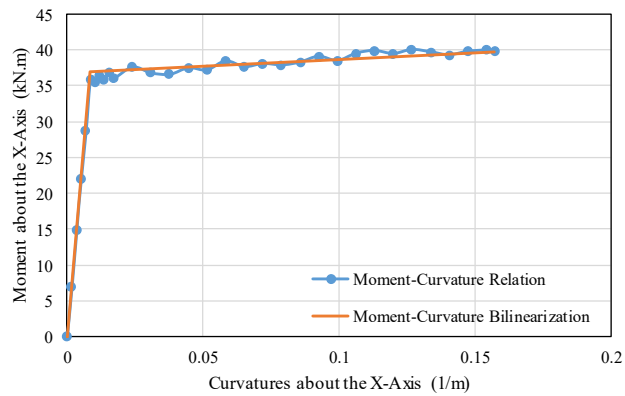
Figure 3.5. *Moment-curvature analysis of the beam section*

25

It is clear from the above Figure 3.4 and Figure 3.5 that the plastic moment capacity of the T-shaped beam section is approximately two times greater than the column capacity. So, the design philosophy is validated through XTRACT section analysis. Also, the bilinear idealization shown in the figures is automatically made by the program. Besides, the analysis results are presented numerically to understand the differences in behavior of RC sections in Table 3.2. The effective values for curvature and moment parameters are obtained from the bilinearization methodology. Based on the given table, the column sections exhibited intended low moment capacity with higher curvature.

Table 3.2. *Numerical results of moment-curvature analysis for the beam and column sections*

Properties	Unit	Column	Beam
Curvature at First Yield	1/m	0.01451	0.008543
Moment at First Yield	kN.m	16.08	35.79
Ultimate Curvature	1/m	0.2099	0.1571
Ultimate Moment	kN.m	16.88	39.81
Effective Yield Curvature	1/m	0.01559	0.008815
Effective Yield Moment	kN.m	17.28	36.93
Curvature Ductility	-	13.47	17.83

3.2. Material Properties

As indicated in previous parts, the concrete and steel materials for reinforced concrete members were selected considering the properties observed in existing RC buildings. All mechanical features of materials used in the construction was determined through material tests. The material tests are quite significant to interpret the experimental behavior and to construct the analytical model properly.

3.2.1. Concrete

The concrete compressive strength of RC frames was selected to be around 16 MPa considering the poor concrete quality in substandard RC structures in developing countries. With the aim of determining the strength of concrete, the cylindirical and cubic samples were taken at the stage of concrete casting. The dimensions for cylindirical specimens are 150 mm in diameter and 300 mm in height whereas the cubic specimens have 150 mm length in each direction. While taking the specimen in cylindirical and cubic forms, the molds were vibrated to allow air bubbles to go out. Then, the concrete specimens were taken out from the molds after 24 hours. Next, they were placed in curing

pool after 24 hours and they were waited 28 days at curing conditions according to TS-EN 12390-2. Finally, the axial concrete compressive tests were conducted at 7 and 28 days after casting as well as the tests carried out at each frame test day. To obtain more reliable data, at least three axial tests were performed at target days. The compressive test results are given in Table 3.3.

According to the results, the average compressive strength obtained as 11.4 MPa at 28 days before any test was performed. In the following days, the compressive strength of concrete was determined at experiment days as 16.2 MPa for G1-1-Reference, 17.0 MPa for G1-2-Steel, 16.2 MPa for G1-3-CuAlMn and lastly 15.8 MPa for G1-4-NiTi. Thus, the mean compressive strength of these values calculated at each test day is 16.3 MPa.

| (a) Cylindirical and cubic specimens after casting | (b) Curing pool | (c) Uniaxial compression test |

Figure 3.6. *Concrete samples*

Table 3.3. *The test results of concrete compressive strength*

Specimen No	Age of concrete (days)	Compressive strength (Mpa)	Average compressive strength (Mpa)
S1	7	9.8	
S2	7	8.9	9.2
S3	7	8.8	
S4*	28	13.0	
S5*	28	13.2	13.1
S6*	28	13.1	
S7	28	11.2	
S8	28	11.9	11.4
S9	28	11.2	
S10	65	17.8	
S11	65	13.4	16.2
S12	65	17.6	
S13	295	17.3	
S14	295	17.1	17.0
S15	295	16.8	
S16	356	16.5	
S17	356	15.6	16.2
S18	356	16.5	
S19	461	14.3	
S20	461	16.1	15.8
S21	461	17.1	

*Cubic specimens, Others are cylindirical specimens

3.2.2. Reinforcement steel

To represent the substandard structures, the plain re-bars were used in the construction except for the foundation where the ribbed re-bars were used. All longitudinal reinforcements in the T-sectioned beam and column sections have the diameter of 12 mm. The diameter of lateral reinforcement in all structural members is 8 mm. Firstly, the axial tension tests were conducted on the steel samples corresponding to each type of reinforcement used in the construction (Figure 3.7). Then, the stress-strain relationships of steel samples are shown in Figure 3.8 and Figure 3.9. Note that a number after the slash symbol represents the length of the tested steel samples.

| (a) Steel samples | (b) Uniaxial tension test setup | (c) Tested samples |
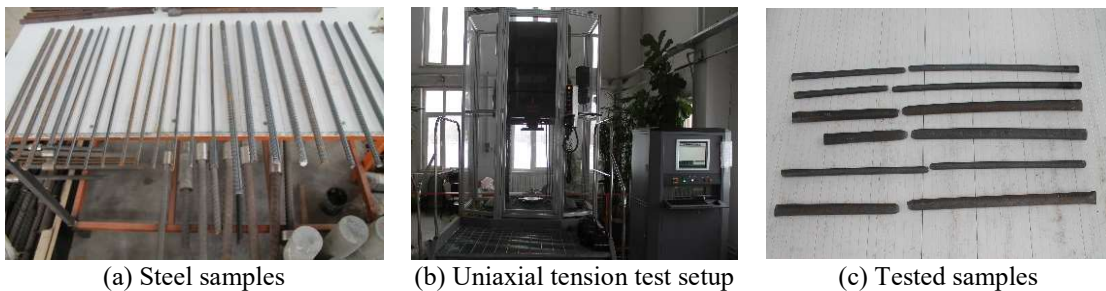
Figure 3.7. *Uniaxial tension test of reinforcement steel*
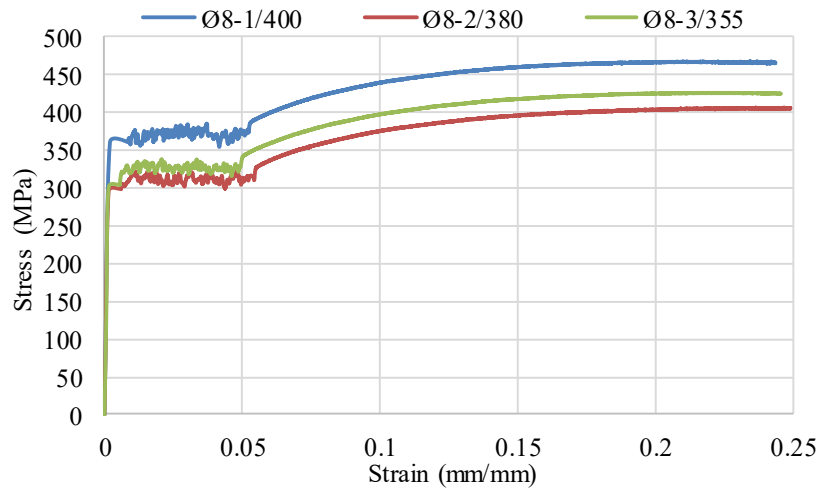
Figure 3.8. *Stress-strain behavior of ∅8 steel re-bars*
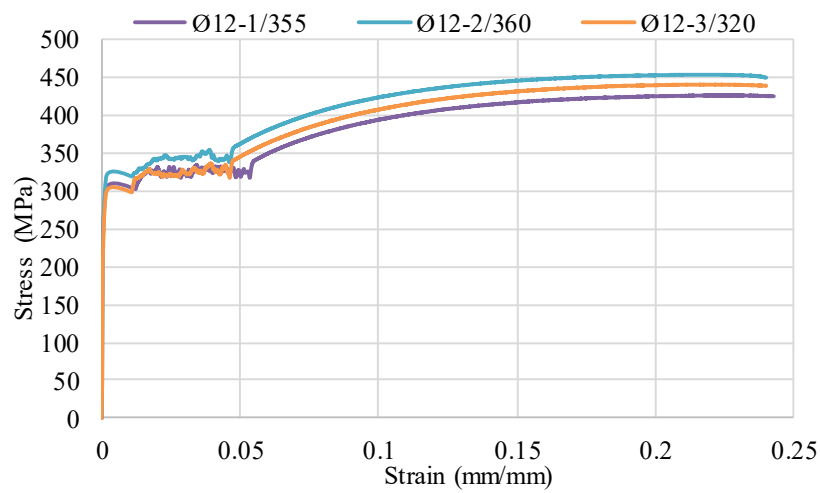
Figure 3.9. *Stress-strain behavior of ∅12 steel re-bars*

Table 3.4. *Numerical results of steel tension tests*

Samples	f_{sy} (MPa)	ε_{sy} (mm/mm)	ε_{sh} (mm/mm)	ε_{su} (mm/mm)	f_{su} (MPa)
∅8/1	370	0.0018	0.0095	0.24	465
∅8/2	310	0.0013	0.0075	0.25	405
∅8/3	325	0.0014	0.0085	0.24	425
∅12/1	325	0.001	0.011	0.24	425
∅12/2	340	0.0013	0.011	0.24	451
∅12/3	325	0.001	0.0125	0.25	440
Average	332.5	0.0013	0.01	0.24	435.2

3.2.3. Strengthening materials

As well as conventional steel and concrete material tests, the uniaxial cyclic tension tests were carried out on the dog-bone shaped coupon specimens taken from each type of strengthening materials used to upgrade the seismic performance of RC frames. The superelastic SMA bars used for strengthening procedure were provided without any small-scaled samples to perform axial test and determine the mechanical properties. Before starting the experiments, the coupon tension test specimens were taken out by means of wire erosion process. There are three types of strengthening bars, conventional Steel bars, CuAlMn and NiTi Superelastic SMA bars and the rod sections are shown in Figure 3.10. As shown in the below figure, all rod sections have threaded portions at their ends. The conventional steel material had already been subjected to uniaxial test in the bar form previously.
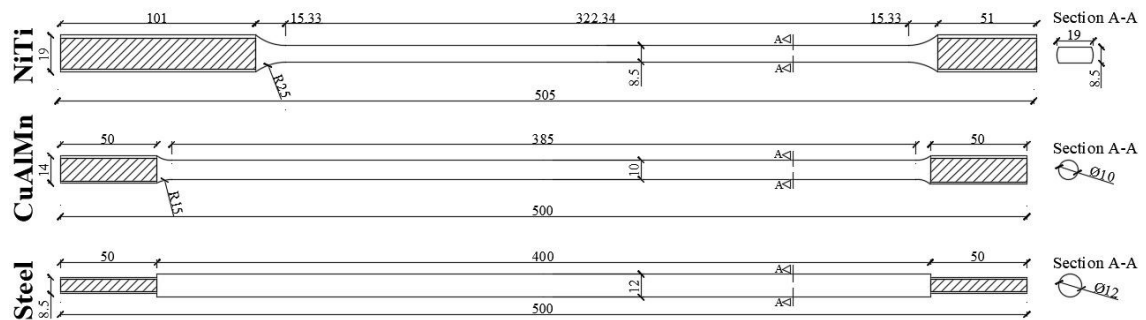
Figure 3.10. *Sectional properties of strengthening bars (Units are in mm)*

In the material selection process of SMAs, a similar approach used by Saiidi et al. (2007) and Araki et al. (2016) considered in this study. It means that the end region of the bars is threaded, and mid-portion of the bars are plain. For the steel strengthening bars, reduced area in the middle length cannot be manufactured with the existing capabilites of the workshop. Therefore, ends of the steel bars were threaded by reducing the end diameter of the bar. Although this application caused to localize the critical section of the steel bar at ends only, they were still employed in the strengthened frame to investigate the behavior.

The dog-bone shaped specimens to be tested for axial tension have a total of 30 mm in height as well as 5-7 mm in flange width. Their average web thickness and width, where the elongation took placed and stresses calculated, were around 0.95-1.15 mm and

2.98-3.04 mm, respectively (Figure 3.11). At least three uniaxial tests for each type of materials were experienced on the samples to increase the reliability of data. The strain rate, $\dot{\varepsilon}$, and room temperature, T°, were 5×10^{-4} mm/mm and almost 24°C in the tests. The strain rate used here is similar to the studies presented by Shajil, Das and Chandrasekaran (2009, p. 174) and Atli (2016). Both cyclic and monotonic loading (tension only) were conducted on the specimens to identify the mechanical properties of materials. It should be noted that the properties obtained from cyclic and monotonic loading can vary in small proportions depending on the ambient room temperature and loading frequency (Shajil, Das and Chandrasekaran, 2009 and Wilson and Wesolowsky, 2005). All material tests were completed in MTS Tensile/Compression Tester having 30 kN capacity in tension and compression located in Mechanical Engineering Laboratory of Anadolu University. In the first place, the web dimensions were measured before the test to estimate the properties. Then, the flanges of sample were connected to a gage by means of bolts and they were screwed. Next the extensometer, which measures the elongation between top and bottom gages, was located on the sample considering that it was nearly in the middle part of the height (Figure 3.12). The loading protocol, which starts with 0.5% strain value and continues until the fracture of material with 1% increasing strain at each cycle, was the same for all materials.

| (a) Web width | (b) Web thickness | (c) Length of a specimen |
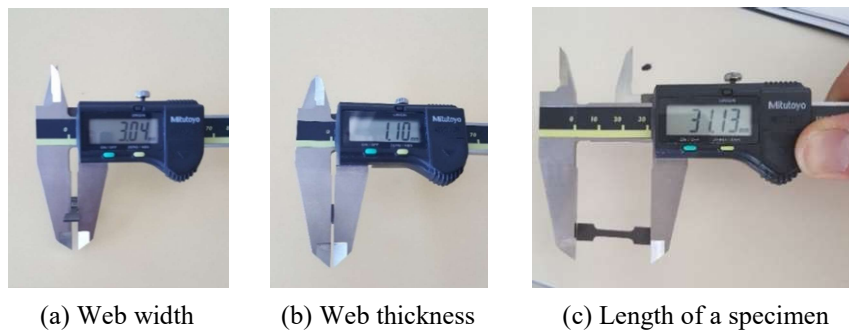
Figure 3.11. *A sample of dog-bone shaped specimen with a digital calliper*

(a) Left view   (b) Back view
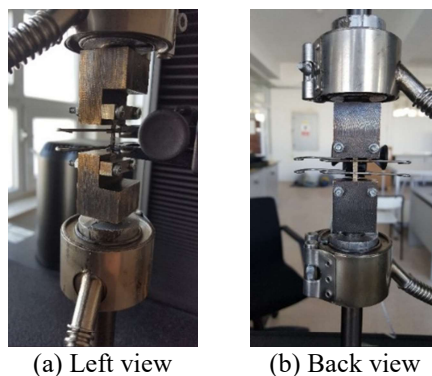
Figure 3.12. *A view of a specimen connected to a gage*

(a) Steel   (b) CuAlMn   (c) NiTi

Figure 3.13. *Tested dog-bone shaped specimens of upgrading materials*

The graphical and tabular illustration of the test results presented in Figure 3.14-Figure 3.19 and Table 3.5. To clarify the results and make more understandable, the behavior of superelastic shape memory alloy samples under increasing tension loading are presented in three types of demonstration for each material test; full phase-transformation including austenite to martensite and martensite to austenite, only austenite to martensite forward phase transformation and direct tensile test. The transformation stresses indicated in Table 3.5 were estimated considering the cyclic loading corresponding to 6% and 7% deformation cycles of NiTi and CuAlMn, respectively. In this approach, we observed a first trend line representing the beginning of martensite phase. Similar method was applied in a study performed by Fugazza (2005, p. 13). Also, austenite modulus of elasticity was calculated as the slope between 15% and 70% of σ_{yo}, which is the observed yield strength at the initiation of nonlinearity on the first cycle of loading to the upper plateau (Tazarv and Saiidi, 2014). Moreover, the martensite modulus was obtained considering the slope of line in the first increasing loading path of martensite phase. The modulus of elasticity is both temperature and strain dependent (Fugazza, 2003).
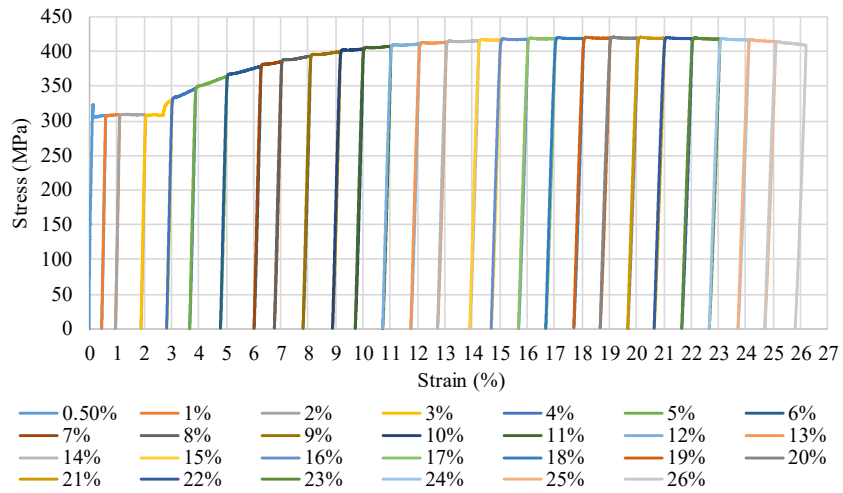
Figure 3.14. *Cyclic tensile test of conventional steel*
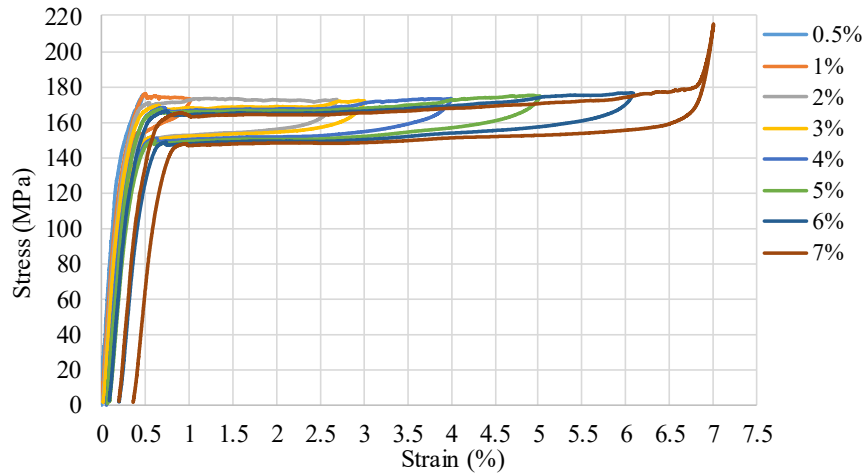
Figure 3.15. *Cyclic tension test of CuAlMn (Before martensite phase)*
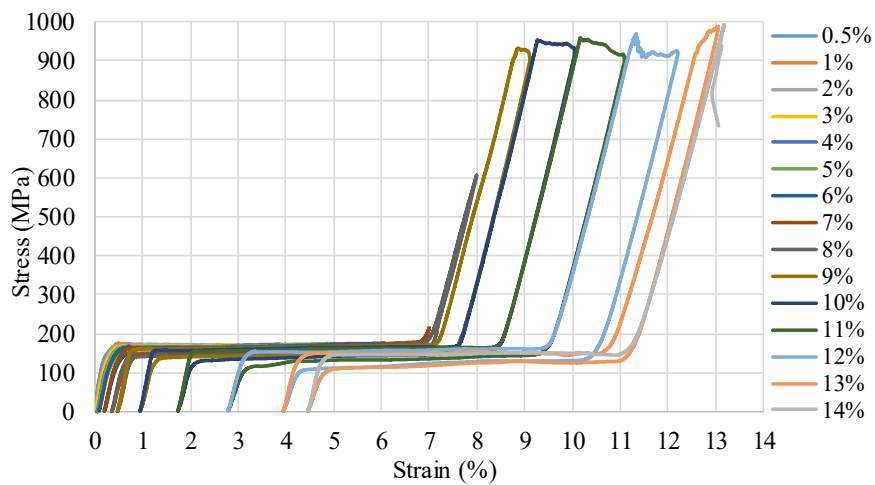
Figure 3.16. *Cyclic tension test of CuAlMn (Full phase)*

33
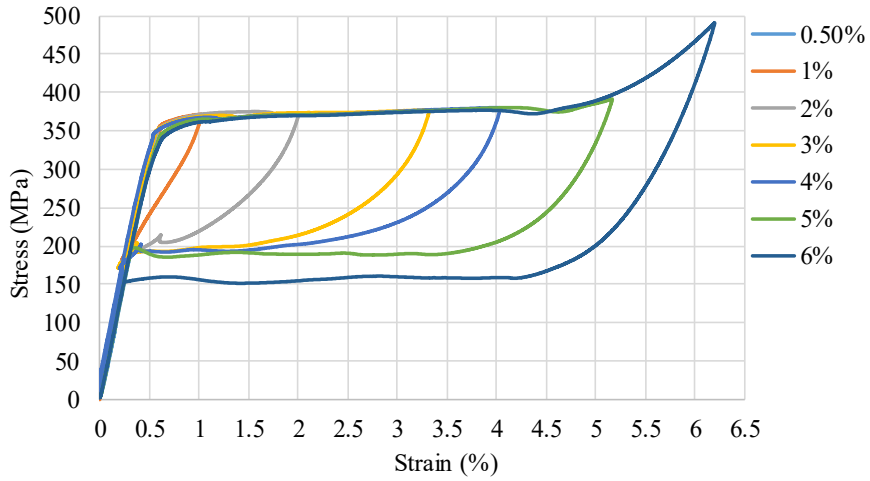
Figure 3.17. *Cyclic tensile test of NiTi (Before martensite phase)*
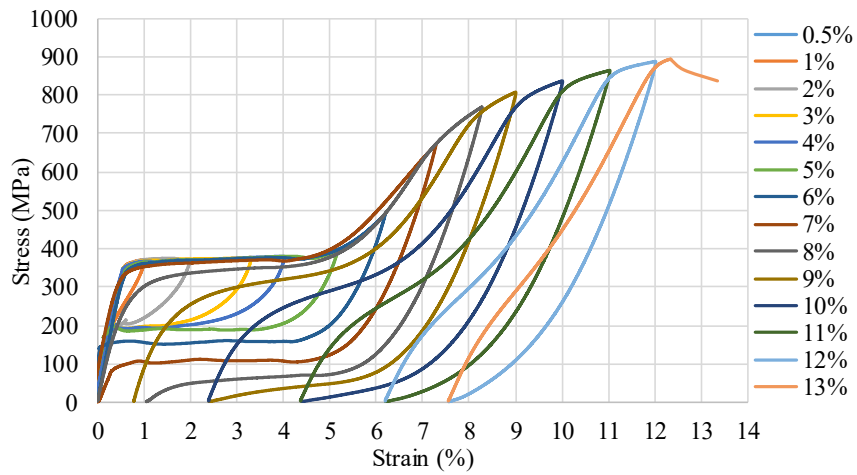
Figure 3.18. *Cyclic tensile test of NiTi (Full phase)*
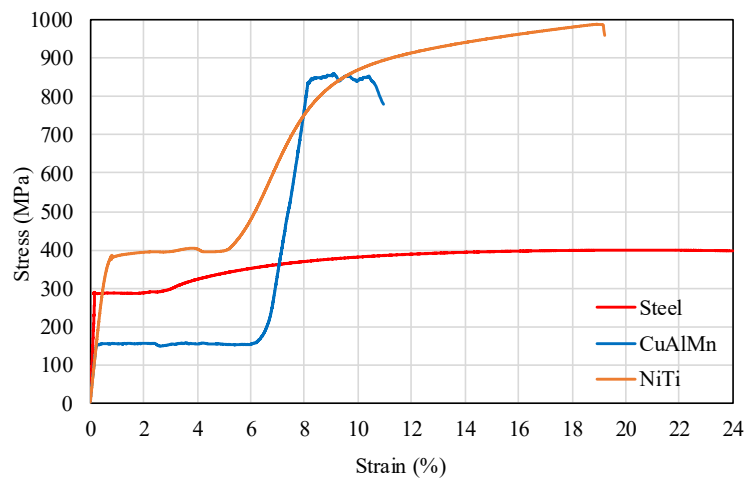
Figure 3.19. *Direct tension tests of Steel, NiTi and CuAlMn*

34

Table 3.5. *Measured mechanical properties for Superelastic NiTi and CuAlMn SMAs*

	NiTi	CuAlMn
σ_s^{AM} (MPa)	365	162
σ_f^{AM} (MPa)	385	174
σ_s^{MA} (MPa)	165	156
σ_f^{MA} (MPa)	150	145
The auestenite yield strain, ε_y^{AS} (%)	0.57	0.49
The austenite modulus, k_1 (MPa)	64500	54600
The postyield stiffness, k_2 (MPa)	372	188
The martensite modulus, k_3 (MPa)	41200	34400
The lower plateau stress factor, $\beta = 1 - \sigma_f^{MA}/\sigma_s^{AM}$	0.59	0.10
Ultimate strain, ε_u (%)	12.35	13.2
Post yield stiffness ratio, $\alpha = k_3/k_1$	0.64	0.63

It is fact that the yield and ultimate stresses of NiTi are higher than other strengthening materials. Also, the area under the stress vs. strain curve of NiTi is greater than the CuAlMn and conventional steel. Obviously, the residual strain values for the conventional steel material upon unloading are larger than the SMA materials. For the SMA materials, the cyclic behavior before and after the austenite phase have some differences. In the CuAlMn test, the hysteresis in the austenite phase has narrower loops than the loops in the martensite region. On the contrary, the NiTi has wider loops in both austenite and martensite phases compared to that of cyclic CuAlMn test. In addition, the shape of forward and reverse transformations differ from each other for NiTi and CuAlMn materials. The SE NiTi SMA has higher modulus of elasticity in both austenite and martensite region in comparison to SE CuAlMn SMA.

3.2.3.1. Residual strain

One of the significant property showing the material behavior under given loading is residual/plastic strain due to nonlinearity of material. In the elastic portion of engineering stress-strain curve, many materails comply with Hooke's law. So, the stress and strain are proportional to each other during elastic behavior. Finally, this proportionality gives the modulus of elasticity or Young's modulus, denoted E. But, the material can show nonlinear behavior after inelastic deformation starts depending on the internal or microscopic structure. In contrast to elastic region, the material experiences plastic deformations even if the load is removed due to new atomic re-arrengement.

Shape Memory Alloys have a distinctive feature of re-centering (self-centering) due to its crystallographical structure and they show negligible residual strains after removing

the load contrary to conventional steel. The illustrations of residual strain of material, ε_r, calculated from the uniaxial tension tests are given separately in the following Figure 3.20 and Figure 3.21. To provide an effective evaluation of residual deformations, the graphical results are presented with and without conventional steel material.
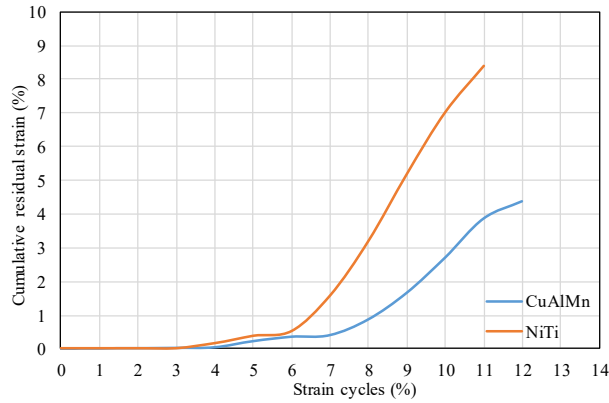
Figure 3.20. *Cumulative residual strain of SMAs*
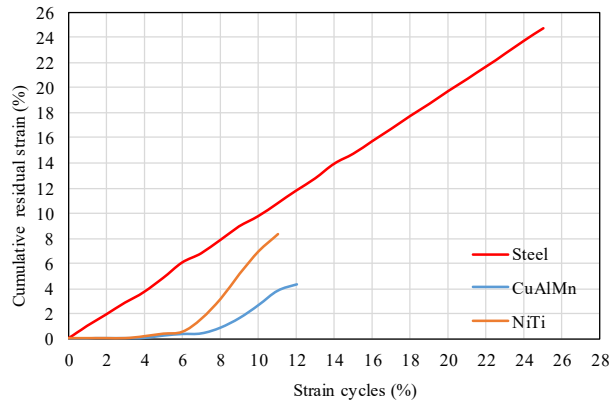
Figure 3.21. *Cumulative residual strain comparison with steel*

3.2.3.2. Recovery capacity of strengthening materials

After presenting the residual strain values of strengthening materials, another essential quantity showing the performance of materials to recover the plastic strains is the recovery capacity. This parameter is estimated from the ratio of the difference between the peak strain and unloading residual strain, which is the intersection point of unloading path to the horizontal axis, for each cyclic drift level (Cortés-Puentes et al. 2018). The recovery capacity is illustrated in Figure 3.22.
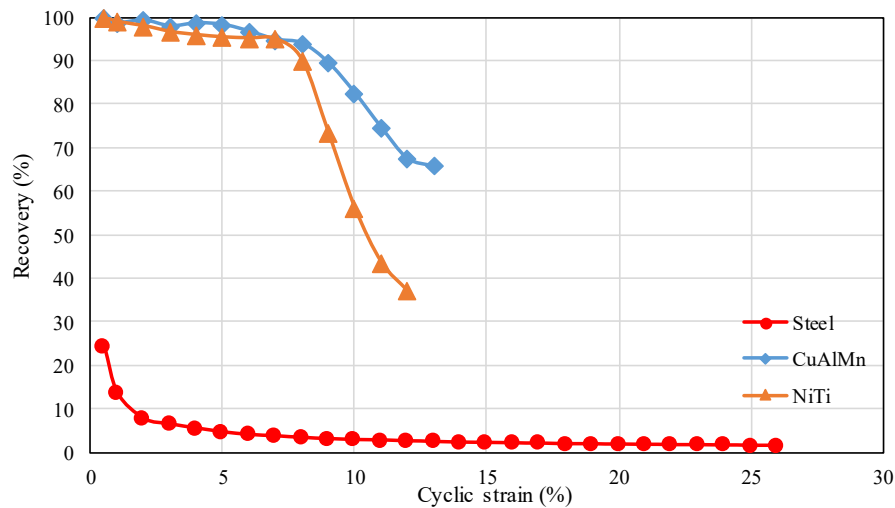
Figure 3.22. *Recovery capacity of the strengthening materials*

It is clear from the above figure that SMA materials are highly advantageous in recovering of inelastic strains in comparison to the conventional steel. This ability of SMA materials arises from the superelastic property. The SE SMA specimens have recovery capacities of almost 95% and over up to 8% cyclical drift ratio. With the starting of reverse transformations from martensite to austenite after 7% drift, the residual strain of SMAs increases and the recovery capacity decreases. At the end of the uniaxial tension test, the SMA materials still show superior performance compared to that of conventional steel. Furthermore, the recovering capacity of CuAlMn is higher than the NiTi SMA. Contrary, the steel material exhibited maximum %24.3 recovering capacity in the first cyclical drift, which is the 0.5% strain. Then, the capacity dramatically drops to %4.65 at %5 drift and it gradually continues to reduce up to fracture point.

3.2.3.3. Dissipated energy

The material absorbs energy during axial loading due to its hysteretic behavior. As shown in previous sections, the hysteretic behaviors of Steel, CuAlMn and NiTi differ from each other. This difference in hysteresis of materials brings about a difference in the amount of energy absorbed. A substantial dissipation of energy happens during a loading-unloading process causing the expectation that a pseudoelastic alloy could function as an effective damping material for incorporation in structures prone to seismic vibrations (Shajil and Chandrasekaran, 2009, p. 171). The dissipated energy of material was

calculated considering the stress-strain area enclosed within each strain cycle. In conclusion, the energy dissipation values of upgrading materials are shown in Figure 3.23.
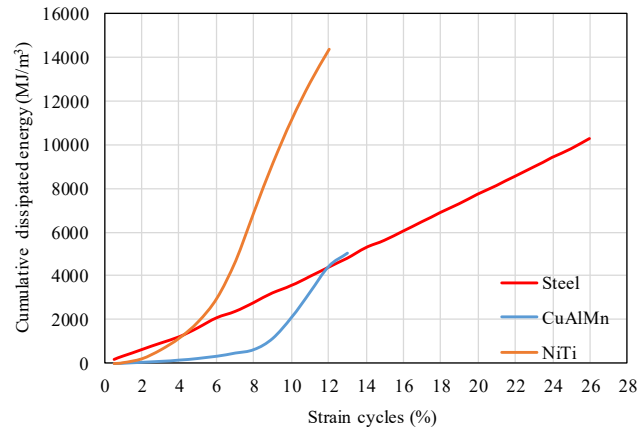
Figure 3.23. *Energy dissipation of upgrading materials during cyclic tensile tests*

It is fact that the conventional steel material shows a linear behavior in dissipation of energy under cyclic axial loading. Contrary, the SMA materials dissipate less energy at the beginning, but then, there is a visible increment in the dissipated energy by SMAs. At the end of the tests, the NiTi showed better dissipation performance in comparison to other materials. Also, the dissipated energy valu by NiTi is 40% larger than the steel although the ultimate strain of steel is relatively higher than the NiTi.

3.2.3.4. Equivalent viscous damping

Considering the hysteretic behavior of structures or materials, they absorb input energy and create hysteretic cycles. Then, such a behavior can be related to the damping capacity considering the characteristics of materials. In this section, the equivalent viscous damping is calculated using the relation between the dissipated energy and elastic strain energy. Similar damping parameter is computed for SMA materials in the studies performed by DesRoches, McCormick and Delemont (2004) and Dolce and Cardone (2001). The equivalent viscous damping is calculated using Equation (3.1) and presented in Figure 3.24.

$$\xi_{eq} = \frac{1}{4\pi} \frac{E_D}{E_{So}} = \frac{1}{2\pi} \frac{A_{loop}}{\sigma_{max} \varepsilon_{max}} \tag{3.1}$$

The SMA materials reach maximum damping ratio at around 4-6% strain and then begin to decline while the sharp decrease in the conventional steel is apparent in the graph up to 10% drift. Considerably, the NiTi has higher damping capacity compared to CuAlMn. In contrast to NiTi, CuAlMn follows more stabilized path during the cyclic test in terms of damping capacity. A sudden drop is observed with the starting of martensite and then the capacity again increases with the growing amplitude of drifts in CuAlMn.
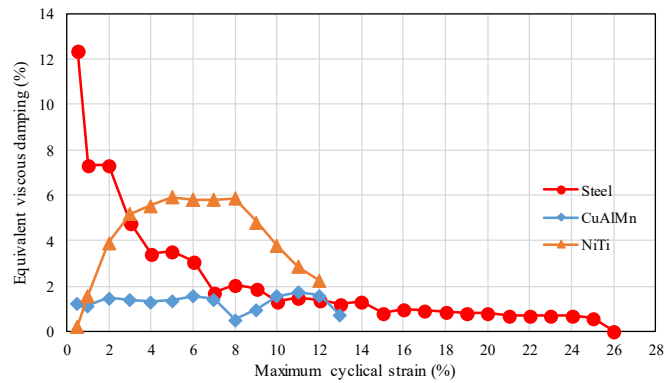
Figure 3.24. *Equivalent viscous damping of materials*

3.3. Shear Capacity Calculation of Column Sections

The RC frames tested in this study were designed such that the plastic hinges should be formed at the column ends due to bending moment under reversed cyclic lateral loading without any shear failure on the column members. In an attempt to obtain such a behavior, the plastic moment capacity of the beam section was designed to be higher than the column sections as calculated in Section 3.1.1. Herein, the shear capacity calculation of column sections was made according to equation given in TEC 2007.

$$V_r = \left[0.52 \times f_{ct} \times b_w \times d \times \left(1 + 0.07 \times \frac{N_d}{A_c} \right) \right] + \left[\frac{n \times A_0}{s} \times f_{yw} \times d \right] \tag{3.2}$$

Equation 3.2. includes tensile strength of concrete (f_{ct}), width of column (b_w), effective height of the cross section (d), axial load applied to the column (N_d), gross section area of column (A_c), number of stirrup arms at a section (n), area of the lateral reinforcement (A_0), spacing of lateral reinforcement (s) and yield strength of lateral reinforcement (f_{yw}). Considering this equation, shear capacity of one column is calculated as 48.6 kN, while the total shear capacity of the reference frame in the loading direction is 97.2 kN.

3.4. Construction of Frames

A total of four 2/3 scaled RC frames were constructed in Structural Engineering Laboratory of Anadolu University. Firstly, the formwork and reinforcement works started concurrently. Secondly, the strain gages were placed on the chosen reinforcements at the critical regions of structural members where the plastic hinges could possibly be formed. After 28 days, the formworks were removed, and the frame surfaces were limed for the cracks to be more visible on the RC members.

3.4.1. Formwork details

The formwork plan was the same for all constructed frames. In the construction of specimens, 70 mm diameter and 400 mm height cylindirical pipes were placed in the foundation to create longitudinal holes with the aim of screwing the bolts and providing fully rigid connection between the frames and strong floor at the foundation level. The plywoods were used for construction of frames and they were oiled with molding oil to avoid the concrete surface damage while the removing the formwork. The dimensions of frame formwork are given in Figure 3.25.
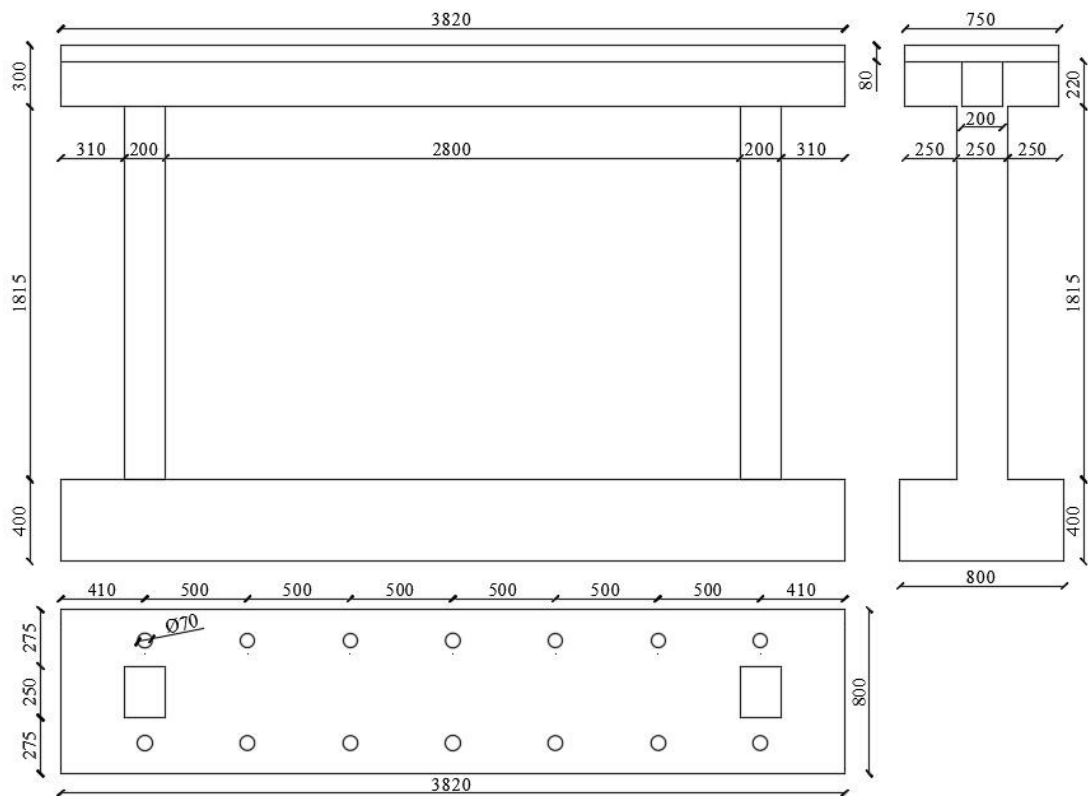
Figure 3.25. *Formwork detail of frames (Units are in mm)*

In the first place, the formwork of foundation was constructed considering the cylindirical holes to be left at the bottom part of plywood. In the second place, the reinforcement works of foundation were completed for all specimens and the reinforcements were placed inside the foundation formworks with 20 mm plastic concrete cover blocks. Afterward, formworks were performed by placing the reinforcement of the column and T-sectioned beam members inside the prepared plywoods. Finally, 15 mm concrete cover blocks were used for column and beam members.

(a) Foundation formwork

(b) Column and beam formwork

(c) Colum and beam formwork

(d) A view of coluımn top end

Figure 3.26. *Formwork works*

3.4.2. Reinforcement details

All the frames constructed in this study were similar to each other in terms of reinforcement and formwork details and so the construction was made concurrently for the specimens. Contrary to the foundation, the plain reinforcements were used in the column and beam members to represent the existing RC buildings. According to the reinforcement plan, the workers prepared the longitudinal and lateral reinforcements of structural members. All lateral reinforcements except for the foundation were constructed

with 90° bended hooks. The lateral reinforcements had 8 mm diameter in all members while the longitudinal reinforcement of foundation and other structural members had 16 and 12 mm diameter, respectively. Additionally, the longitudinal reinforcement ratio of the column sections is 0.9%. This ratio is lower than than the limits specified in TS500 and TEC2007 for column sections. The stirrups were placed with a spacing of 150 mm in the column and beam members. Therefore, there was no confinement zones at the member ends. Figure 3.27 displays the reinforcement details of RC frames.
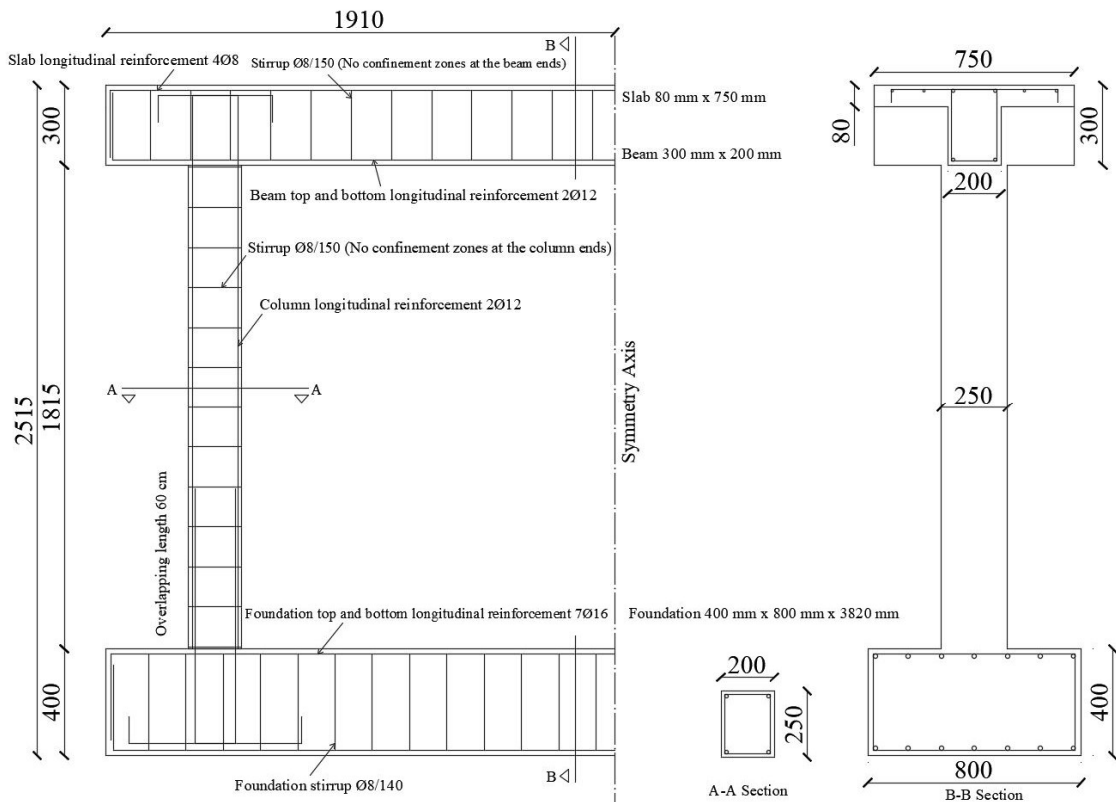
Figure 3.27. *Reinforcement details of frames (Units are in mm)*

3.4.3. Installation of strain gages

The strain gages, which are able to measure the strain on the steel reinforcements under loading condition, were placed on the longitudinal and lateral reinforcements to record the axial deformations of the re-bars at the critical RC sections. For the installation of strain gage, the following steps are applied;

1. The surface of reinforcements to be placed strain gage were smoothened by means of small hand-machine and a cleaner surface was obtained.

2. To keep the reinforcement surface free of dust and rust, an aceton with cotton was used to clean up the surface.

3. Just after cleaning up, the strain gages were immediately bonded on the bars. While placing, the important thing was to determine the axial direction at which the deformation could occur depending on loading conditions. At the same time, the adhesive should not be exposed to the gages.

In experiments, the strain gages provided by Micro Measurement Company used to record the axial strain on the steel re-bars. The internal gage resistance of used strain gages was $120 \mp 0.3 \ \Omega$ and this value were measured via a digital multimeter after completing the installation (Figure 3.28b). Thus, this measuring process provides an information about whether there is short circuit or not.

(a) Strain gage on the stirrup	(b) Control of proper installation
(c) A view from the beam end and joint	(d) Strain gages on the column top end
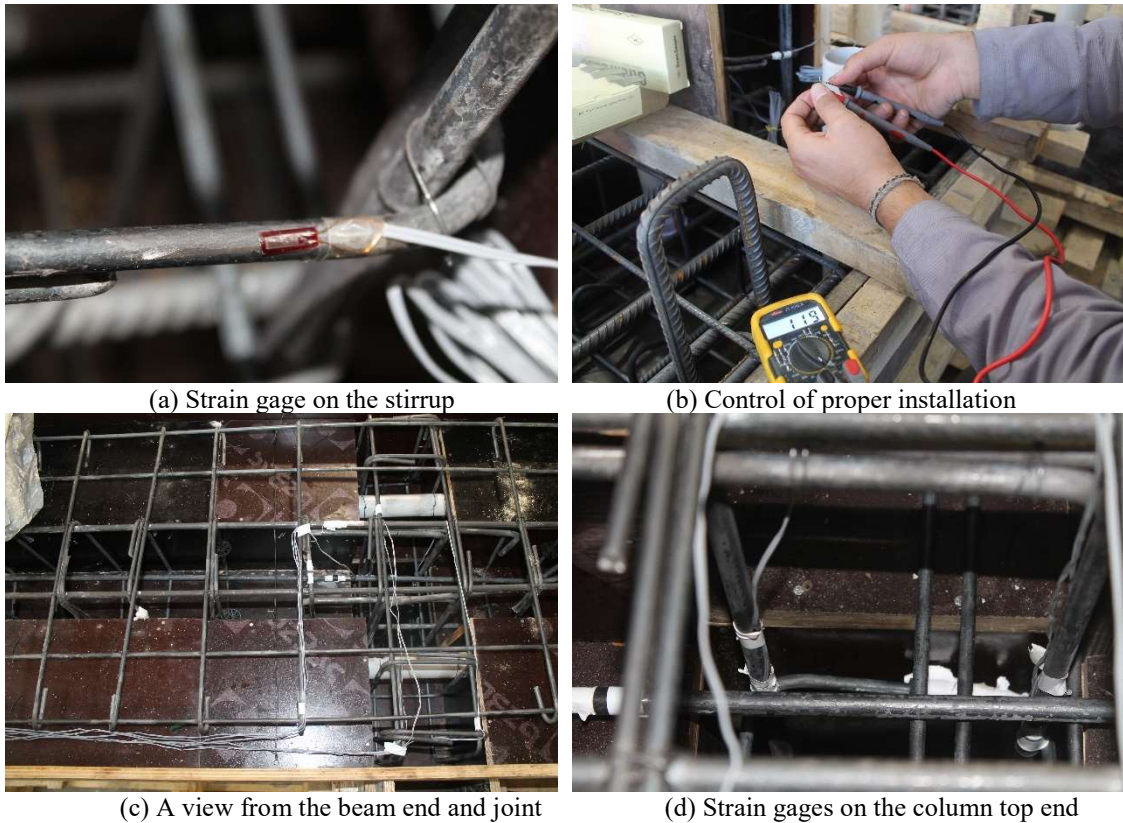
Figure 3.28. *Views of strain gage installation*

A sample arrangement for strain gages and the notations showing the position of reinforcement in the members are given in following Figure 3.29. The highlighted re-bars with colors indicated the exact location of strain gages in the frames. Moreover, this figure has a key role to understand the positions of cracks to be given in next chapters.
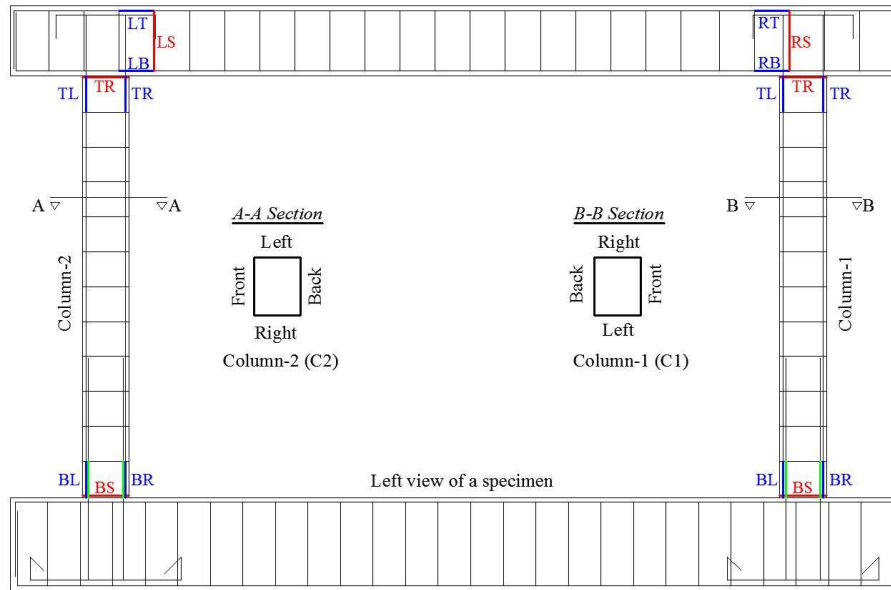
Figure 3.29. *Strain gage positions and column directions to indicate the location of cracks*
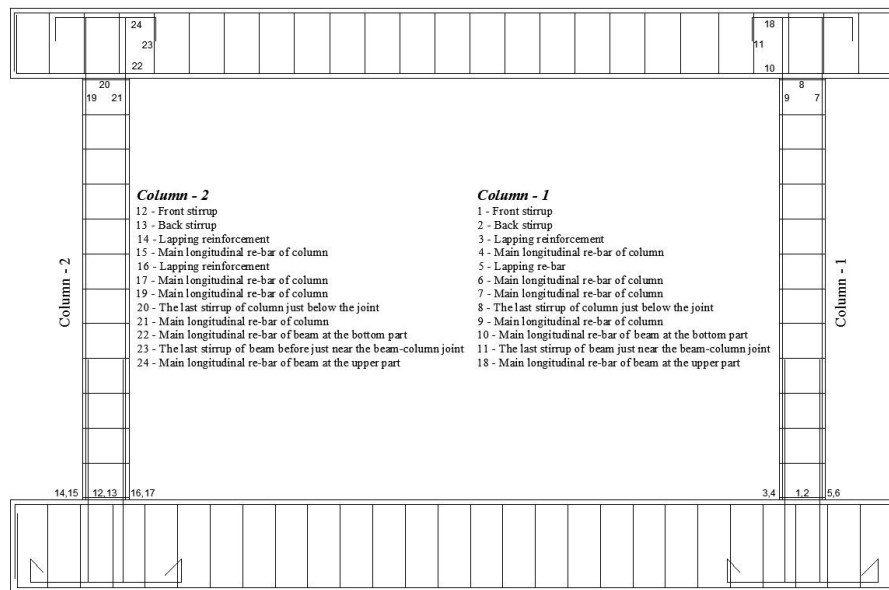
Figure 3.30. *A sample SG arrangement*

Here, the meaning of each uppercase letter in above figure is as follows; B : Bottom, T : Top, R : Right, L : Left, S : Stirrup. These denotations are going to be employed in the following chapters to explain the strain measured on reinforcements. Also, blue line represents longitudinal re-bars, green line represents lapping re-bars and lastly redline represents stirrups at measured sections.

44

Strain gage installation was the final step for construction of frames. Afterward, the frames were ready to concrete casting. In this step, the strain gages were stuck with sticky tape to avoid any physical damage during the concrete casting.

3.5. Concrete Casting

Ready-mixed concrete was used to fill the formworks with concrete after completeing the previous steps. A vertical concrete casting method was utilized due to inadeaquate area in Structural Engineering Laboratory. A mixer firstly emptied the concrete out into a large volume boiler. Then, the concrete was poured into the foundation through a crane by opening the bottom cover, but not to the highest level of foundation. Next, the column and beam formwork were filled with concrete while the vibration was being done with an internal concrete vibrator for the air bubbles to go out. Finally, surface finishing was completed to obtain a smooth and plane concrete surface. The concrete surfaces of frames watered for 7 days with the aim of obtaining suitable curing conditions.

(a) A mixer and boil	(b) Vibration process of concrete
(c) Finished-surface of slabs	(d) Watering of frames
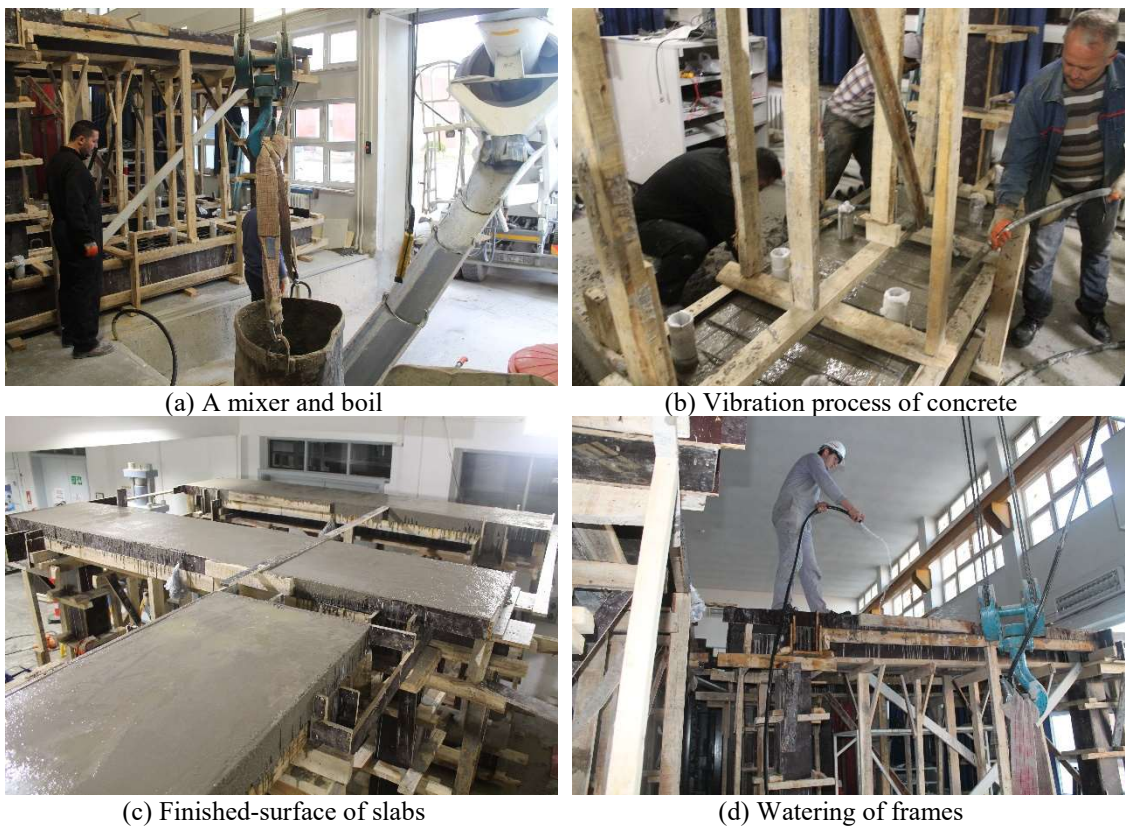
Figure 3.31. *Some stages for concrete casting*

3.6. Strengthening Mechanism

In order to get use of the superelastic behavior of SMA bars effectively, they are attached to the structural system such that SE SMA bars will work under axial tension only. A seismic protection system was designed and produced within the scope of this thesis study in such a way that the ends of RC columns were not involved in an interaction with strengthening mechanism to prevent the possible shear failures on the column faces. This philosopy is important for both functionality of column under the effect of lateral loading and avoiding premature flexural and shear failure. Consequently, a mechanism involving steel profiles and steel plates with different thicknesses were fabricated in workshop. Similar mechanisms providing SMA materials having different physical and chemical forms to be loaded axially were produced in previous studies. Eartheton et al. (2014) developed self-centering buckling restrained brace using SMA rods having shape memory effect and investigated its application for reducing the seismic damage. Ozbulut and Hurlebaus (2011) proposed the re-centering variable friction devices (RVFD), which have two subcomponents; SMA wires and variable friction damper, for adapting to civil structures exposed to near-fault ground motions to provide seismic protection. Dolce et al. (2000) presented a study about an implementation of seismic passive control device containing different types of shape memory alloy wires and bars. They designed and produced a SMA brace for framed structures and isolation devices for buildings and bridges. Lastly, U-shaped superelastic SMA damper with self-centering functions was suggested and examined experimentally and numerically by Wang and Zhu (2018) in order to explore the potential usage of flexural behavior of SE SMAs in seismic applications.

The loading path follows a way that the load comes from actuator to the RC frame at the beam level. Then, the load is transferred to the strengthening bars through U-shaped plates while some portion of the applied load was transferred to RC columns. Next, the load is transferred from the SMA bars to a vertical steel plate with 30-mm thickness above the HE-240-B beam, which is connected to steel columns having a cross-section of HE-240-B.

To avoid shear failure in the strengthening mechanism, simple analytical model of proposed mechanism was created in SAP2000 v14 platform. The mechanical properties of strengthening bars obtained from the material tests were implemented in the analytical model to calculate the response of the steel components employed for strengthening. The

maximum lateral load capacity of any upgraded RC frame was obtained in SeismoStruct under reversed cyclic loading. Afterward, this load was applied to the joints in SAP2000 in positive and negative directions to monitor the joint deformations and support reactions. In such a lateral loading, the shear stresses occur mostly in the bolts used for connection due to bending moment. The number of bolts and geometric dimensions were selected such that there was no failure in any type of bolts.
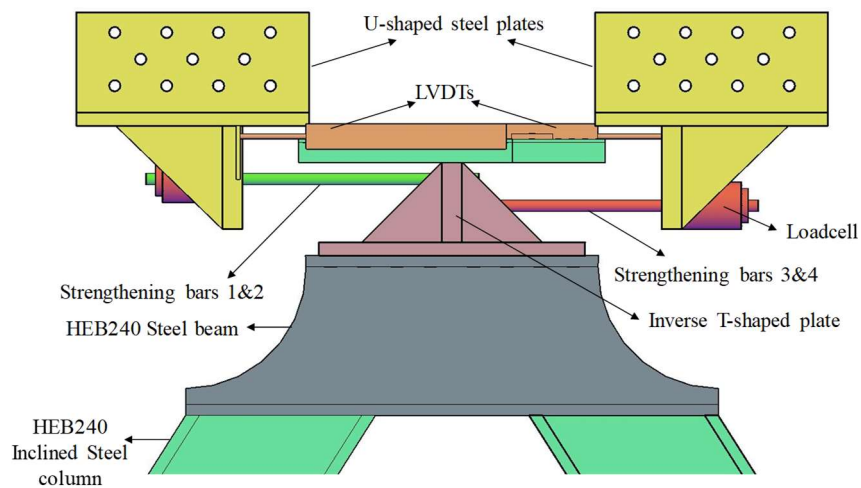
Figure 3.32. *Detail of strengthening mechanism (Side view)*
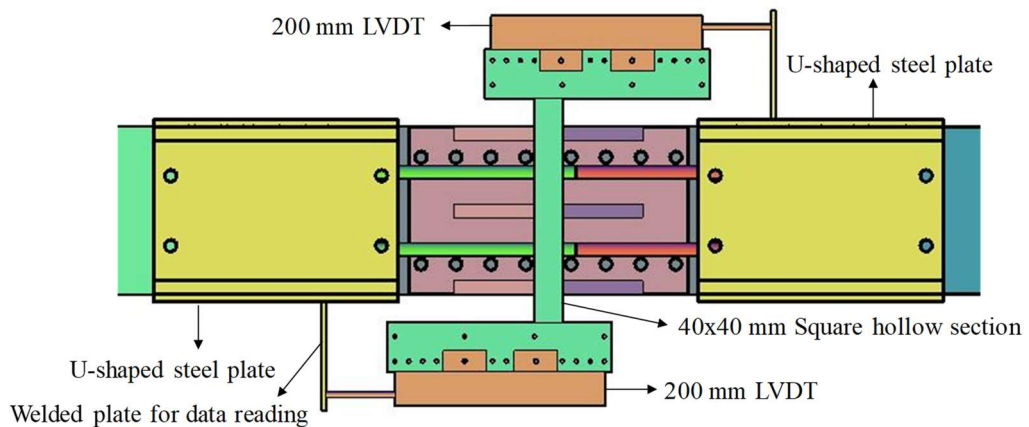
Figure 3.33. *Detail of strengthening mechanism (Top view)*
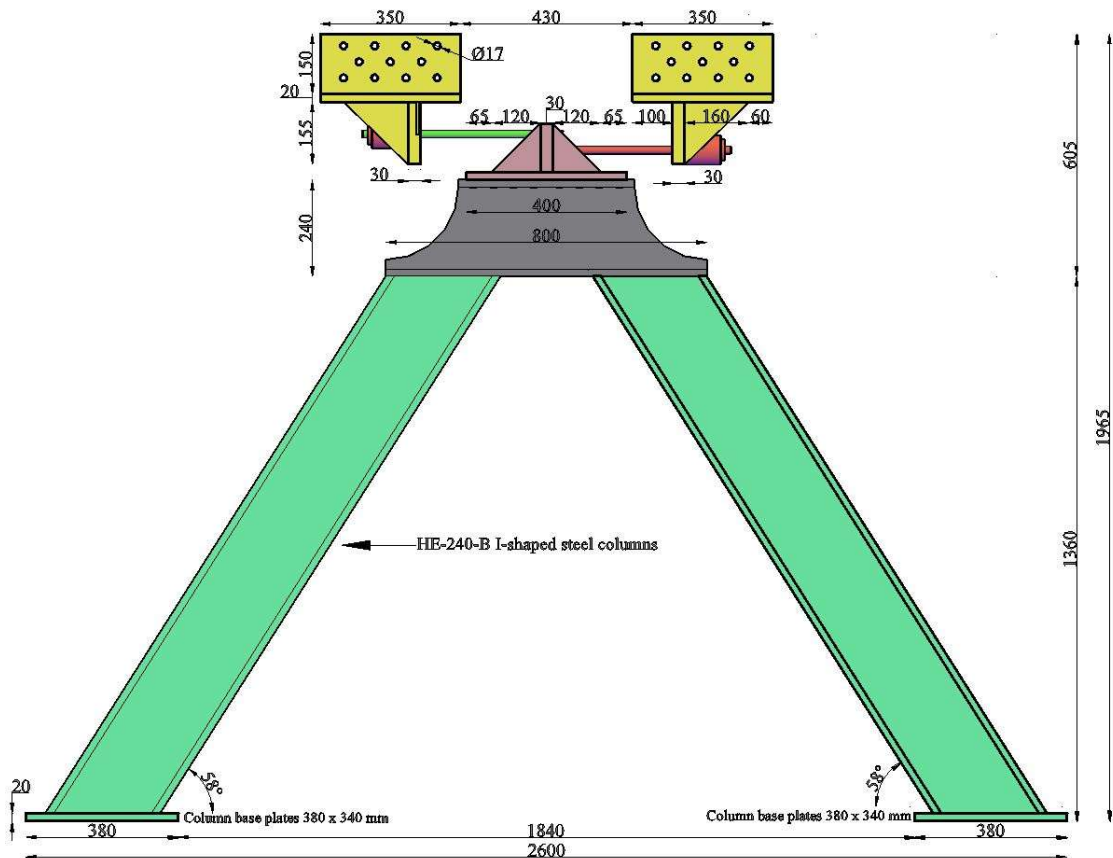
Figure 3.34. *Dimensions of strengthening mechanism (Units are in mm)*
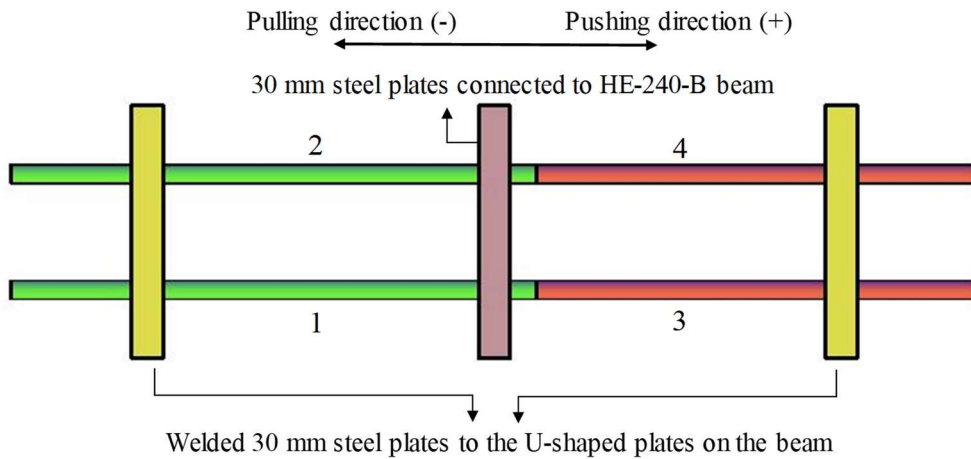
Figure 3.35. *Indication of pushing and pulling rods*

As shown Figure 3.35, the red bars are active in case of pushing direction (forward loading) while the green bars are active in pulling direction (backward loading). When

two of the SMA bars active, the other two bars are inactive, and they do not carry compression load owing to the connection details of the bars.

3.6.1. Installation of strengthening mechanism

A special care was given in the construction of strengthening mechanism to achieve tension only bars for the SE SMAs. In case of incorrect assembling, the bars could be subjected to compression force. The system includes four parts; U-shaped plates, trapezoidal portion of the mechanism including I-shaped inclined steel columns and HE-240-B beam and lastly inverse T-shaped portion placed in the center of steel beam. It should be noted that the steel columns and beam were welded to each other while the T-shaped inverse portion was mounted to the beam by means of M14x70 mm fully threaded bolts. Firstly, the trapezoidal part of the mechanism was placed on the foundation via crane and then a sketch was drawn considering the 17 mm holes left on the base plates. Secondly, the marked points were drilled vertically through the foundation with the help of a drilling machine. Thirdly, the trapezoidal portion was lastly mounted to the foundation through M16x110 mm expansion bolts. Some details of mounting are given in Figure 3.36.

| (a) A sketch for base plate of steel columns | (b) Marking of holes with red color |
| (c) Drilled holes on the foundation | (d) Completed mounting of steel columns |
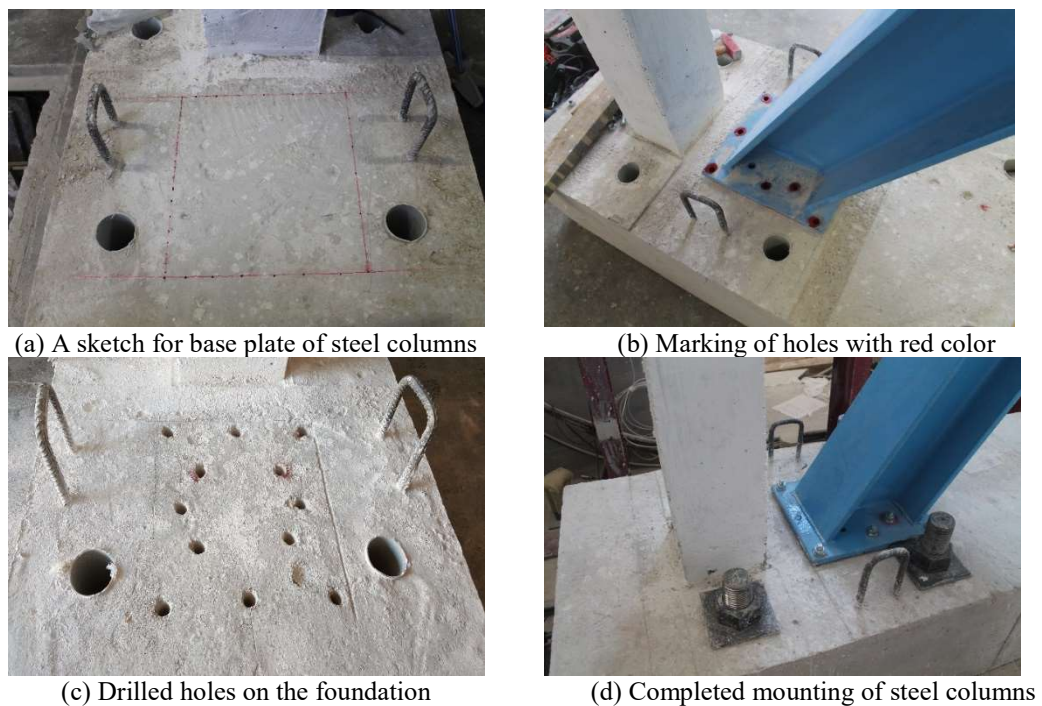
Figure 3.36. *Assembling of trapezoidal steel columns*

Next stage of installation of strengthening mechanism is to place the U-shaped plates on the beam by considering the length of the strengthening bars and the distance between the vertical plate of inverse T-shaped portion and the vertical plate of U-shaped plates. The threaded portions of strengthening bars must be out of 30 mm vertical plates to screw the nuts and it provides bars to have sufficient effective length. In the mounting of U-shaped plates to the beam, the M12x90 mm expansion bolts were used. To take out the expansion bolts after the tests, the hole length was drilled greater than the length of bolts. Thus, the bolts were embedded in the beam via a hummer after completion of each test. There was also another task on placing of the bars that they were needed to be placed in the system as they would be vertically and horizontally balanced. Some stages of assembling of U-shaped plates are illustrated in the following Figure 3.37.

| (a) First position of U-shaped plates | (b) Close view of position arrangement |
| (c) Close view after mounting of U-shaped plates | (d) Completed assembling of strengthening system |
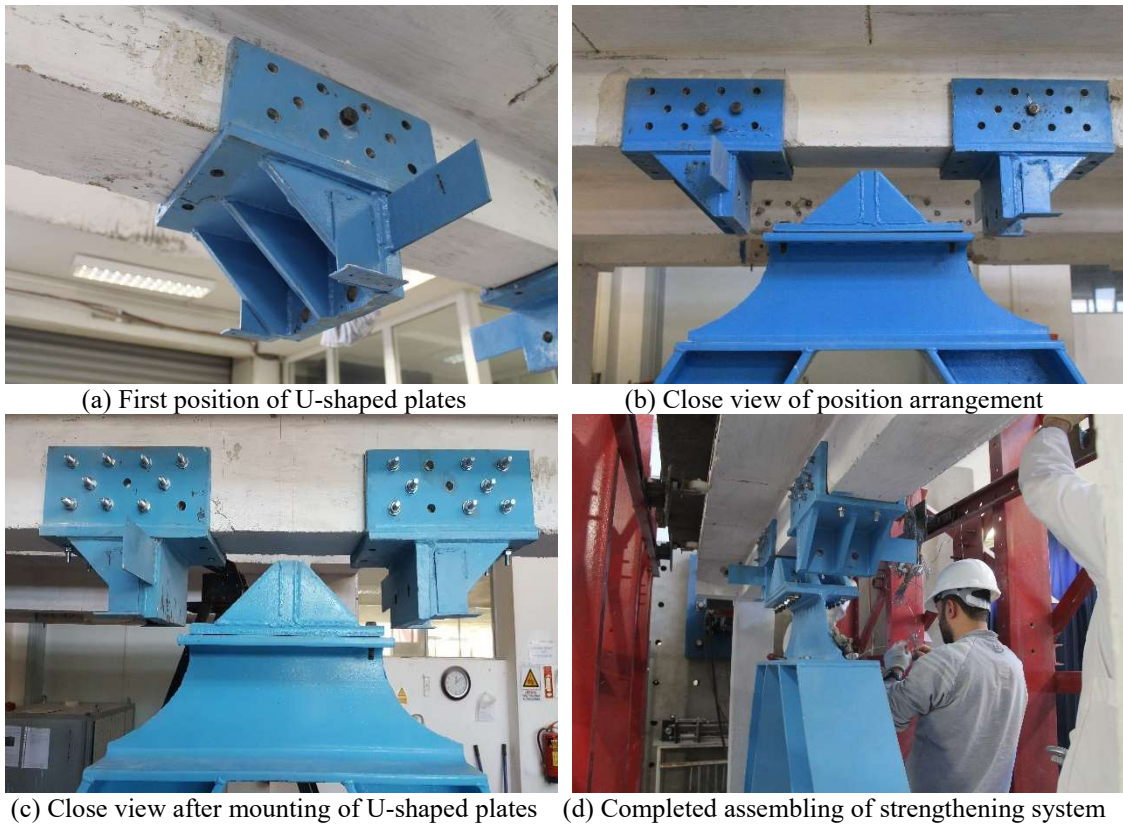
Figure 3.37. *Assembling of U-shaped plates*

3.7. Ambient Vibration Measurements

Structural Health Monitoring (SHM) is an important and developing area in many disciplines such as mechanical engineering, civil engineering and aeronautics to detect and diagnose small variation in vibratory characteristic of monitored machine or structure (Wenzel and Pichler, 2005). It has been emphasized in the past two decades that structural health monitoring can provide information about the response of the considered objects to ambient or dynamic excitations. The modal parameters of interested systems such as natural frequencies, mode shapes and damping ratios can be specified by means of ambient vibration measurements (Arslan and Durmus, 2014; Ozcelik et al., 2015). Furthermore, it is possible to interpret the seismic performance of structures damaged due to a variety of causes such as earthquakes, hurricanes, winds, traffic depending on these vibration-based measurements since the damage affects the structural characteristics such as stiffness (Amezquita-Sanchez and Adeli, 2016). The damage can be related to the loss of stiffness of the system and detected by using frequency change-based damage identification methods (Fan and Qiao, 2011; Escobar et al., 2005; Inci et al., 2017).

Within the context of this study, ambient vibration measurements were taken from RC frames before and after experiments to identify the change in the stiffness due to the damage occurred during the lateral cyclic loading. So, totally four uniaxial and force balanced accelerometers were used at the two upper ends of the RC frame at the beam and slab level. The accelerometers were placed at two end points at the slab level with the aim of comparison to improve the reliability of the ambient vibration measurement data. All measurements were carried out without any additional mass on the frame and connection between actuator and the frame. The RC frames were only connected to the strong floor by means of bolts during the vibration test measurements. Ambient vibration measurements were performed with a sampling rate of 200 Hz. It must also be kept in mind that the measurements were only conducted in frame direction since the first mode of RC frame were determined as highly dominant compared to that of second and third mode as observed in SeismoStruct v17 platform. Accelerometers and data logger are presented in Figure 3.38.

| (a) Accelerometers at the front end | (b) Data logger |

Figure 3.38. *Ambient vibration equipments*

3.8. Test Setup

All the RC frames were constructed and tested in the Structural Engineering Laboratory of Anadolu University. The required equipments and test setup were produced in Workshop of Engineering Faculty. The laboratory has a strong floor and wall with nearly 78-80 mm holes to apply a horizontal load through actuator and to fix the specimens to the base. The details of experimental setup are given in Figure 3.39-Figure 3.41.

| (a) Hydraulic MTS actuator | (b) Close view of MTS-frame connection |

| (c) Laboratory view before test setup | (d) Front view of test setup | (e) General view of experimental setup |

Figure 3.39. *Experimental setup in the structural engineering laboratory*

To be able to apply lateral load to the frames, the MTS actuator with a load capacity of 445 kN in pulling direction and 650 kN in pushing direction as well as stroke capacity of 500 mm was used in the tests. The horizontal load can be applied by means of MTS actuator either displacement or force-controlled loading. It is worthwhile to mention that the pushing load is transmitted to the RC frame by a steel plate with a thickness of 30 mm. This load comes from the core steel of hydraulic actuator. However, the pulling load is transmitted to the RC frame by means of four longitudinal rods having 33 mm diameter and connected to two 30-mm steel plates at the ends via nuts. A special attention was paid to the pre-loading while the nuts at the ends of the bars are tighthened with the aim of not to introduce further axial load to the beam.
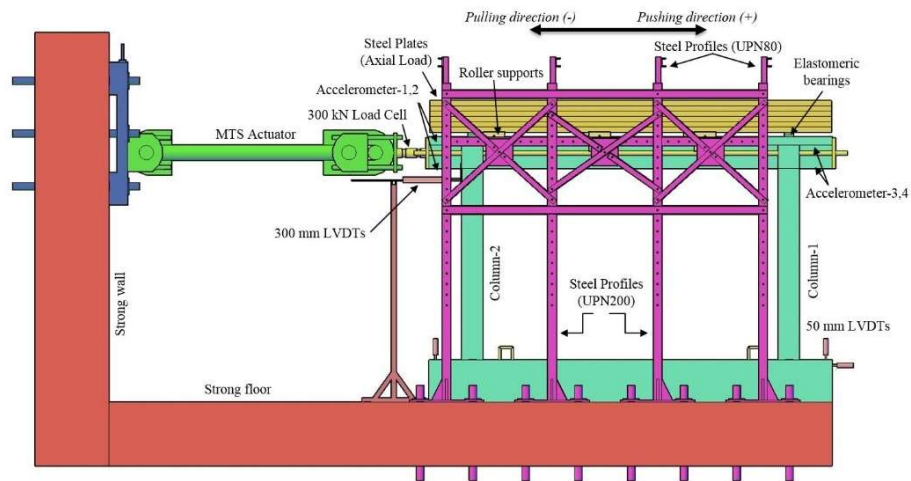
Figure 3.40. Left view of fr*ame test setup*
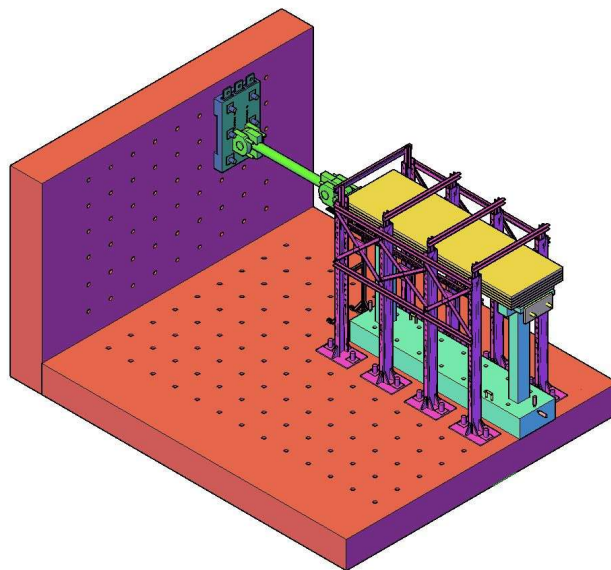
Figure 3.41. *3D view of test experimental setup*

Also, the specimens were fixed to the strong floor through 10 bolts with a diameter of 64 mm to restrict any displacement in any direction. To prevent the motion of foundation during the loading process due to gap between strong floor's hole and the bolts, rings with outer diameter of 78 mm and inner diameter of 65 mm were utilized in connection. Since the frames are similar to each other in terms of geometric dimensions, a single type of test setup was constructed. Additionally, the specimens were encircled with a steel frame involving UPN200 and UPN80 profiles to prevent out-of-plane displacements and to hold the axial load applied on the columns in case of any collapse. The constant axial load corresponding the 10% of the axial load capacity of the columns was applied to the column ends through steel plates. Further axial load level could not be applied because of limited laboratory capacity and safety concerns. Moreover, this load level is the minimum value specified in TEC (2007) for columns. Elastomeric bearings between steel plates and the column top ends were used to transmit the loads. It should be noted that these bearings also provide RC frame not to be introduced additional stiffness from steel plates. In the test setup, the roller supports were involved by a wheel system at both sides of the slab to prevent out-of-plane movement of the RC frame under the combined effect of lateral and vertical loading.

In the experiments, a displacement controlled quasi-static reversed cyclic lateral loading protocol was applied to all specimens (Figure 3.42). A three-cyclic drift ratio with 0.5% drift increment in both pushing and pulling directions was used until 1% drift ratio as %1 drift inclusive. Then, the load increment of 0.5% drift was adopted to loading protocol with two cyclic motion. While determining the loading pattern, the critical inter-storey drift ratios specified in TEC (2007) was taken into consideration as well as the literature studies. Moreover, quasi-static cyclic loading was suitable for this study since the probable damage was predicted before the test (FEMA-461). The reason for preferring more cyclic loading pattern before 1.5% drift ratio is to obtain more valuable information on the hysteretic response of the proposed strengthening system.
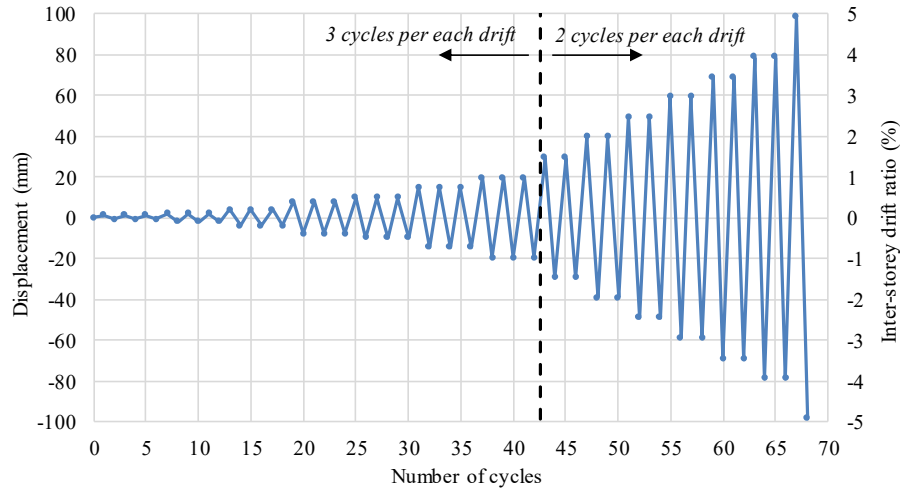
Figure 3.42. *Applied loading protocol*

3.9. Data Acquisition System

In the experiment, various measurement instrumentations were employed in the data acquisition system to get the information on the seismic response of the RC frame under lateral cyclic loading. There were four types of equipments used in the test setup to read the data;

1. Load Cells (LCs)
2. Linear Variable Differential Transformers (LVDTs)
3. Strain Gages (SGs)
4. Data Logger

An external load cell with a capacity of 300 kN was engaged in addition to the load cell embedded in hydraulic actuator. To observe the displacements at the level of beam, strengthening bars and the foundation, three LVDTs with different capacities were employed in the test setup; 300 mm, 200 mm and 50 mm, respectively. Also, 50 mm LVDTs were used to see rotation at foundation, if any. Furthermore, strain gages were placed on the reinforcements of columns and beam to observe the axial strain of re-bars during the loading. A sample SG denotation and arrangement in a frame is shown in Figure 3.30. There was a data logger reading and transferring the data from all equipments to a computer with a sampling rate of 1 Hz. Finally, four accelerometers were placed on the various points of frames to carry out ambient vibration measurements with the aim of detecting the change in natural frequency.

4. EXPERIMENTAL RESULTS

4.1. General

A total of four 2/3 scaled one-bay one-storey RC frame experiments was conducted in this thesis study. The frames were subjected to reversed cyclic loading to investigate the seismic performance of RC frames upgraded with different SE SMA and conventional steel bars. The obtained and analyzed data are presented in graphical and tabular forms in the following chapters to explore the seismic response of frames considering the related parameters. Also, the damage patterns of frames are shown throughout pictures taken during the experiments. It is important to know the denotations of frames given in Table 1 in order to follow the next chapters. The experimental results are presented in separate sections under each of its heading. Then the comparisons are made among the frame test results to point out the advantages and disadvantages of each type of strengthening procedure. Note that there were no infill walls in any frame and all of the frames under consideration were tested by using same loading conditions. It should be kept in mind that all the frames tested are the same in terms of geometric dimensions, the level of axial load and other details except for the strengthening materials. The formwork and reinforcement details, beam and column sections, test setup and lastly loading history of experiments are given in previous chapters. It was a predicted behavior in the design stage that a failure mechanism at column ends took placed due to the strong beam-weak column phenomena. Accordingly, there was no shear failure in the structural members.

4.2. G1-1-Reference Frame

The first frame test was the reference test. It is essential to have an information regarding the seismic performance of as-built RC frame without any upgrading method. The average concrete compressive strength was determined as 16.2 MPa on the test day of G1-1-Reference frame obtained from cylindirical concrete specimens.

As shown in Table 4.1, the lateral load capacity of the reference frame was determined as 31.2 kN after completing the first test. The reference frame reached its ultimate load at 47th cycle corresponding +39 mm lateral displacement and +2% drift ratio. It should be indicated that the forward and backward directions were not attained the ultimate load capacity at the same time. When the frame reached -49.14 mm displacement, a maximum peak load in horizontal direction was achieved in 52th cycle for pulling direction contrary to pushing. After 2% drift ratio, the specimen lost its

strength gradually with the formation of severe flexural cracks at the column ends. The width of existing cracks widened following 2% drift ratio. The hysteretic behavior of reference specimen is given in Figure 4.1.

Table 4.1. *The load and displacement history of G1-1-Reference*

Cycle No.	Roof Displacement (mm)	Base Shear (kN)	Real Drift Ratio (%)	Expected Drift Ratio (%)
1	0.93	3.45	0.05	0.05
2	-0.61	-8.7	-0.03	-0.05
7	1.89	7.95	0.10	0.10
8	-1.56	-12.3	-0.08	-0.10
13	3.84	14.55	0.19	0.20
14	-3.42	-18	-0.17	-0.20
19	7.74	21.75	0.39	0.40
20	-7.32	-24.3	-0.37	-0.40
25	9.78	22.35	0.50	0.50
26	-9.3	-24.6	-0.47	-0.50
31	14.67	25.65	0.74	0.75
32	-14.22	-27.3	-0.72	-0.75
37	19.02	26.7	0.97	1.00
38	-20.13	-28.65	-1.02	-1.00
43	29.19	30	1.48	1.50
44	-29.49	-30	-1.50	-1.50
47	39	31.2	1.98	2.00
48	-39.27	-30.9	-1.99	-2.00
51	48.54	30.6	2.46	2.50
52	-49.14	-31.2	-2.49	-2.50
55	58.68	29.7	2.98	3.00
56	-59.31	-30.75	-3.01	-3.00
59	68.55	29.25	3.48	3.50
60	-68.85	-29.85	-3.49	-3.50
63	78.39	28.5	3.98	4.00
64	-78.87	-29.4	-4.00	-4.00
67	98.19	27.75	4.98	5.00
68	-98.49	-28.2	-5.00	-5.00
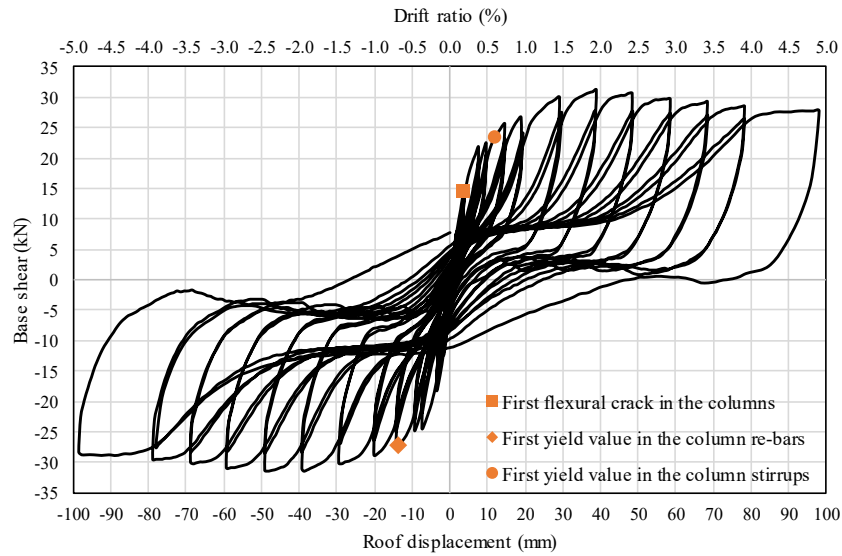
Figure 4.1. *Hysteretic behavior of G1-1-Reference Frame*

The observed and measured failure patterns are marked on the hysteretic loops of G1-1-Reference frame. In the beginning, the loops have narrow and steep paths due to its own stiffness. But then, hysteretic loops widen with the effect of starting inelastic deformations and the slope of loading and unloading path reduces following the stiffness deterioration after 0.5% roof drift ratio. There is a slight decrement in the ultimate load of the frame after it attains maximum base shear.
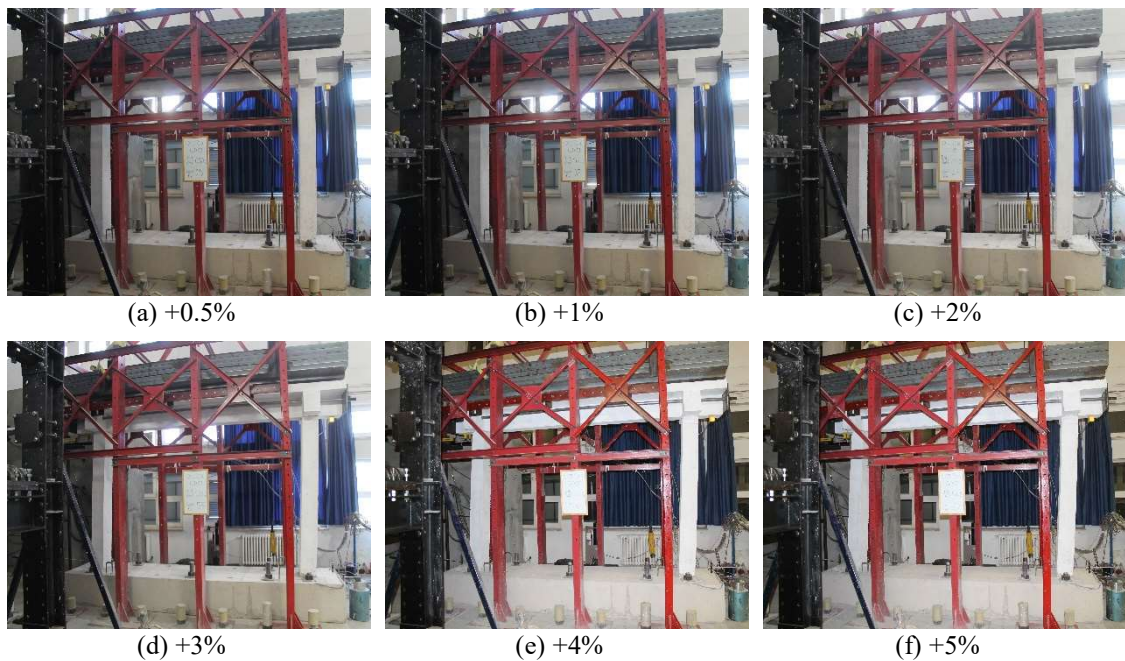
Figure 4.2. *Appearance of G1-1-Reference frame at some of the critical drift ratios*

According to the results, first flexural crack of columns was observed at +0.19% drift ratio while a serious increment in width of this crack was firstly observed in beam-column joints at +0.4% drift ratio. There was no crack on the beam member as expected. The way to realize whether the reinforcements are yielded or not is to process the data obtained from strain gages and compare with the yield strain value calculated from the material tests. In the above hysteresis curve, the small orange shapes related to yielding of reinforcements are marked taking into account this estimation. The first observed and measured failures are given in Table 4.2. In addition, the photos showing some failure patterns during the loading are given in Figure 4.3.

Table 4.2. *Critical failure steps in cracks and reinforcements*

	Cycle No.	Roof Displacement (mm)	Base Shear (kN)	Drift Ratio (%)
First flexural crack in the columns	13	3.84	14.55	0.19
First yield value in the column re-bars	32	-13.56	-27	-0.69
First yield value in the column stirrup	31	11.94	23.4	0.61

(a) First flexural crack in the column	(b) A crack measuring at -1% drift ratio
(c) Column bottom end at -1.5% drift ratio	(d) Swelling of concrete at +2% drift ratio
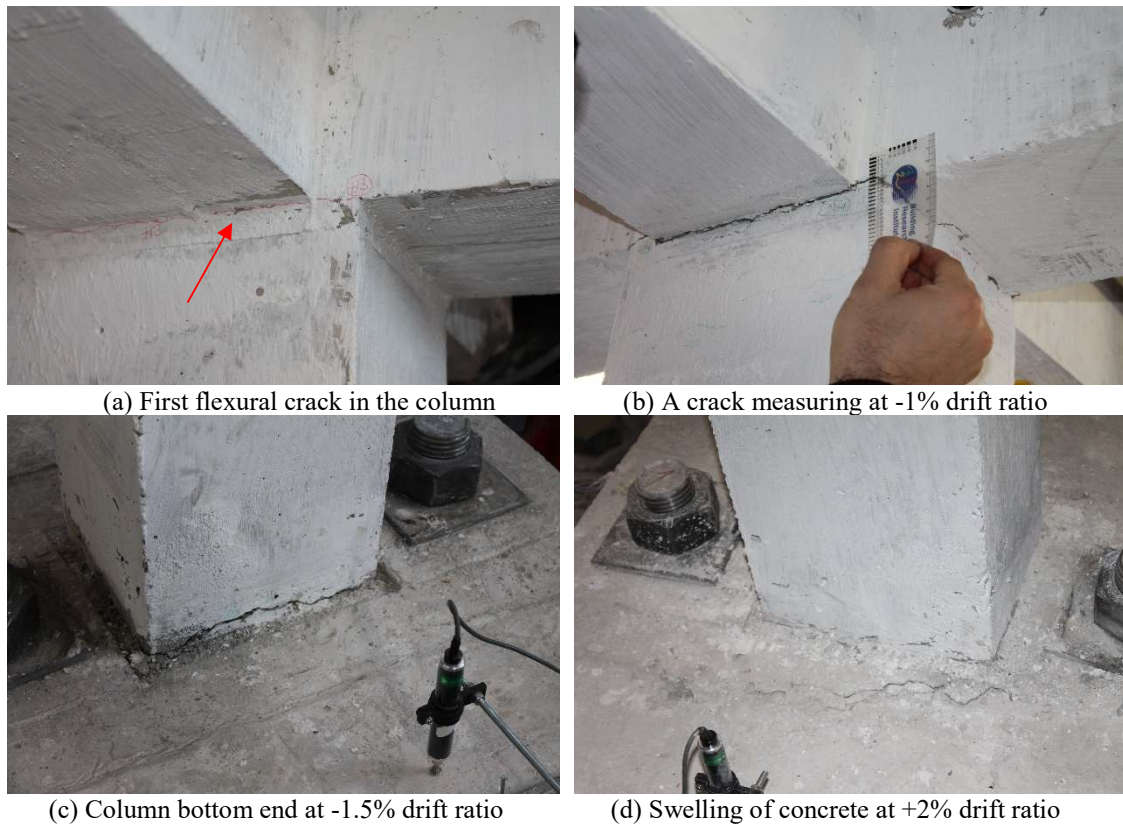
Figure 4.3. *Failure pattern of specimen G1-1-Reference frame at critical roof drifts*

G1-1-Reference frame had a lateral displacement without a failure up to 5% drift ratio. A ductile behavior was observed during the reversed cyclic loading with the formation of plastic hinges at the column ends. Such a ductile behavior can be attributed to low axial load level on the columns. As expected, there was no shear damage on the frame members. At the end of the tests, the column members were exposed to flexural damages at the ends where these regions were subjected to maximum bending moments under lateral loading (Figure 4.4).

(a) Column bottom end at +4 drift ratio

(b) Column top end at -4% drift ratio

(c) Colum top end at -5% drift ratio

(d) Column-1 view at +5% drift ratio
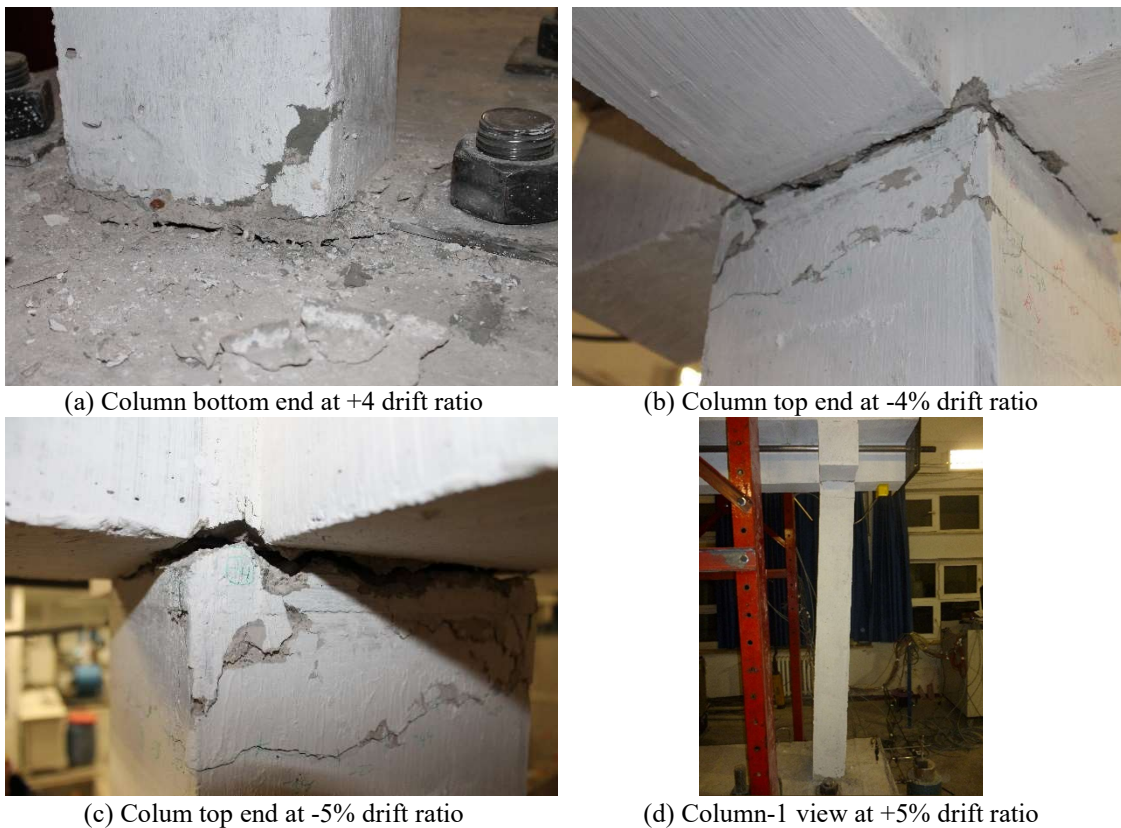
Figure 4.4. *Failure pattern of G1-1-Reference at maximum drift ratios*

The cracks formed at the column ends were visually observed and measured during the experiment. Thus, all the information regarding the cracks are presented in Table 4.3. Keep in mind that it was hard to follow each crack in the column faces at each cyclic drift ratio. Also, it was easier to follow the cracks in the top end of columns. To understand the location of cracks, it is important to remember Figure 3.29. One must be further explained to understand the location of cracks that C1 or C2 represents the Column-1 or Column-2, the Top or Bottom means region of cracks (top or bottom end of columns) and

lastly 1 or 2 next to Top and Bottom terms identify the first and nearest crack to the column (1 means firt observed crack and 2 means the second serious crack).

The first flexural crack was detected at +0.19 roof drift, but the following table (Table 4.3) gives information when the related crack comes to visibly measurable form. The first severe flexural cracks formed at the column ends where the maximum bending moment occurred. The #13 and #14 cracks attained 5 mm and 7 mm maximum crack widths at the end of the test. The second cracks formed on the column face positioned below #13 and #14 is #19 and #20. The width of these cracks are relatively lower than the first observed cracks due to less bending moment. There is a sharp increase in crack widths after the frame attained its ultimate load.

Table 4.3. *The locations of main flexural cracks with the growth in width*

Cycle No.	Crack No. Corresponding first formation	Roof Displacement (mm)	Base Shear (kN)	Drift Ratio (%)	Crack width (mm)	Location of Crack (Name of Member - Side - Region)
19	13	7.74	21.75	0.39	0.3	C1 - Front - Top - 1
20	14	-3.42	-18	-0.17	0.3	C1 - Back - Top - 1
25	13	9.78	22.35	0.50	0.35	C1 - Front - Top - 1
26	14	-9.3	-24.6	-0.47	0.4	C1 - Back - Top - 1
31	13	14.67	25.65	0.74	0.65	C1 - Front - Top - 1
32	14	-14.22	-27.3	-0.72	0.75	C1 - Back - Top - 1
37	13	19.02	26.7	0.97	0.85	C1 - Front - Top - 1
38	14	-20.13	28.65	-1.02	1.2	C1 - Back - Top - 1
44	14	-29.49	-30	-1.50	2	C1 - Back - Top - 1
47	19	39	31.2	1.98	0.4	C1 - Front - Top - 2
47	19	39	31.2	1.98	0.5	C2 - Back - Top - 2
47	13	39	31.2	1.98	2	C1 - Front - Top - 1
51	13	48.54	30.6	2.46	3	C1 - Front - Top - 1
51	19	48.54	30.6	2.46	0.7	C1 - Front - Top - 2
52	14	-49.14	-31.2	-2.49	4	C1 - Back - Top - 1
52	20	-49.14	-31.2	-2.49	0.35	C1 - Back - Top - 2
55	13	58.68	29.7	2.98	3.5	C2 - Back - Top - 1
55	19	58.68	29.7	2.98	1	C2 - Back - Top - 2
56	14	-59.31	30.75	-3.01	5	C1 - Back - Top - 1
56	20	-59.31	30.75	-3.01	0.45	C1 - Back - Top - 2
60	20	-68.85	-29.85	-3.49	0.4	C1 - Back - Top - 2
61	13	68.58	27	3.48	5	C2 - Back - Top - 1
61	19	68.58	27	3.48	1	C2 - Back - Top - 2
63	19	78.39	28.5	3.98	1.3	C2 - Back - Top - 2
64	14	-78.87	-29.4	-4.00	7	C1 - Back - Top - 1
64	20	-78.87	-29.4	-4.00	0.5	C1 - Back - Top - 2

4.3. G1-2-Steel Upgraded Frame

In the second experiment, the substandard RC frame was strengthened with four conventional steel bars. The geometric dimensions of these bars and the working principle of strengthening mechanism for pushing and pulling directions are given in previous chapters. Contrary to G1-1-Reference, this and those experiments to be presented in the following chapters have strengthening mechanism. Not only we have the structural members such as beam and column but also we have strengthening rods in the test setup to enhance the seismic performance of RC frames. Therefore, it should also be considered and evaluated the contribution of strengthening bars to the seismic performance of RC frames. For such an evaluation, extra instruments were installed to the test system in addition to existing data acquisiton system.

G1-2-Steel reached 78.9 kN ultimate lateral load capacity at 1% drift ratio for forward and backward loading. The experiment was terminated at 1.5% drift ratio because of fracturing of strengthening steel bars. It is a fact that the bars in both directions work under axial loading while the hydraulic actuator pushes or pulls the frame. It is a key role in this experiment that the length of the threaded portions for the steel rods is totally 10 cm with smaller diameter as compared to middle portion of the bars (Figure 3.10). This difference resulted in that non-threaded portions of the bars were in elastic range while the threaded portions of the strengthening rods were in inelastic range with permanent deformations. This caused the failure of the ends of the steel bars before occurrence of any nonlinear deformation at the mid-portion of conventional steel.

The force-displacement relationship of the second experiment, which presents the first cyclic loading of roof drifts, is shown in Table 4.4. Additionally, the hysteretic response of the Steel-strengthened frame is demonstrated in Figure 4.5. The G1-2-Steel upgraded frame had 44 cyclic loops at the end of the test.

Table 4.4. *The load and displacement history of G1-2-Steel*

Cycle No.	Roof Displacement (mm)	Base Shear (kN)	Real Drift Ratio (%)	Expected Drift Ratio (%)
1	0.645	24.15	0.03	0.05
2	-0.78	-15.9	-0.04	-0.05
7	1.5	38.25	0.08	0.10
8	-1.485	-27.15	-0.08	-0.10
13	3.06	45.6	0.16	0.20
14	-2.85	-42.75	-0.14	-0.20
19	7.83	70.05	0.40	0.40
20	-7.485	-65.1	-0.38	-0.40
25	9.645	70.65	0.49	0.50
26	-9.39	-69.45	-0.48	-0.50
31	14.955	78	0.76	0.75
32	-14.4	-77.1	-0.73	-0.75
37	19.65	78.9	1.00	1.00
38	-20.07	-78.9	-1.02	-1.00
43	30.015	31.95	1.52	1.50
44	-31.185	-30.45	-1.58	-1.50

Some critical response stages are marked on the hysteretic response of the G1-2-Steel in the Figure 4.5. The first flexural crack in the column was observed at +0.08% drift ratio while the frame was trying to reach +0.1% drift ratio. Similarly, flexural cracks occurred in another symmetric column when the frames attained -0.1% drift ratio. Formation of first flexural crack corresponds to 1.5 mm roof displacement and 38.25 kN base shear. As the frame exceeds elastic range of its hysteresis, G1-2-Steel showed a ductile behavior with yielding of lapping and longitudinal reinforcements of columns. Plastic hinges were formed at the top and bottom ends of columns related to overall flexural action. It is clear from the hysteresis that the frame lost its ultimate load sharply due to fracturing of strengthening bars. The loading and unloading paths have nearly same slope, which corresponds to the stiffness, especially after 0.5% roof drift ratio. The imposed displacement from 0.4% drift to 0.5% corresponds to average 2 mm and 0.5% drift seems to have narrower band hysteresis compared to that of previous loops. Additionally, the G1-2-Steel gained more stiffness in the pre-yielding and post-yielding behavior in comparison to other experiments because of contribution of steel bars to the rigidity of frame. Apparently, the frame was not exposed to serious damage as visually observed in the first specimen and the partial self-centering mechanism can be observed in the hysteresis while the frame tries to come back to the zero position.
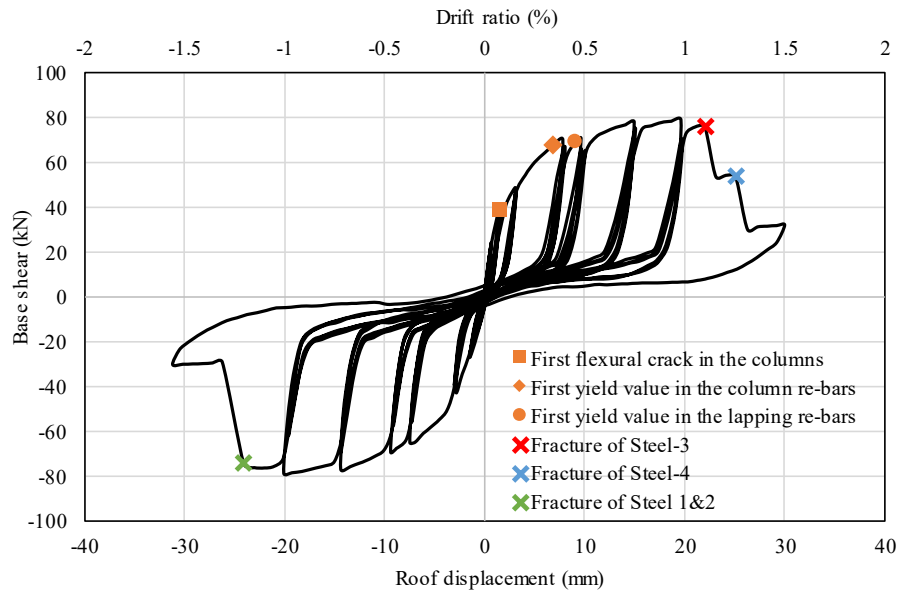
Figure 4.5. *Hysteretic behavior of G1-2-Steel*

(a) +0.5%

(b) +0.75%

(c) +1%

(d) +1.5%
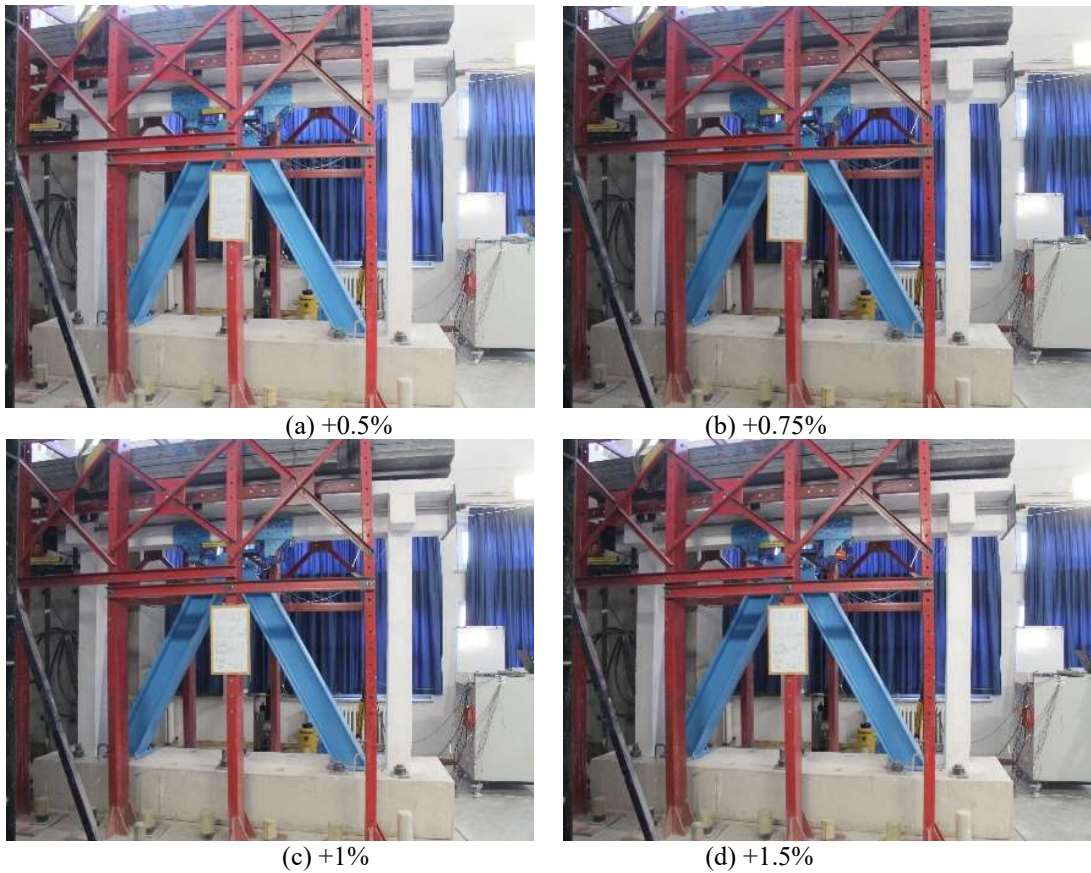
Figure 4.6. *Appearance of G1-2-Steel at critical drift ratios*

Contrary to the rods in pulling direction, the strengthening rods in pushing directions were not fractured at the same time although the failure was occurred during +1.5% drift ratio for both rods. The reasons for such a manner of rods might be due to the difference in material characterization, mechanical threading process and loading conditions. The detailed summary regarding the first flexural crack, critical failures of re-bars and fracture of steel bars is presented in Table 4.5.

Table 4.5. *Critical failure steps in cracks, reinforcements and strengthening bars*

	Cycle No.	Real Roof Displacement (mm)	Base Shear (kN)	Drift Ratio (%)
First flexural crack in the columns	13	3.06	45.06	0.16
First yield value in the column re-bar	19	6.825	67.35	0.35
First yield value in the lapping re-bar	25	9.03	69	0.46
Fracture of Steel-3	43	22.02	75.6	1.12
Fracture of Steel-4	43	25.11	53.4	1.27
Fracture of Steel 1&2	44	-24.075	-74.7	-1.22

The strengthening steel bars used in the system fractured with a ductile manner at the end of the test. It means that the threaded end regions of the bars elongated as the imposed drift ratio increases. Then, the end region of the steel bars attained ultimate strain level and the bars fractured. Some flexural failures on the columns and views from the fracturing of bars are illustrated in Figure 4.7.

| (a) First flexural crack in the column | (b) Column top end at +0.75% drift ratio |

| (c) Fracture of Steel-3 | (d) Fracture of Steel 1&2 |

Figure 4.7. *Failure pattern of G1-2-Steel at critical roof drifts*

Also note that the U-shaped plates was slightly affected by lateral loading during the test. Only the hairline concrete cracks due to compression failure around the U-shaped plate was detected in the test. No distinct failure was observed on the strengthening mechanism at the end of the test. Failure pattern of columns after the experiment are displayed in Figure 4.8.

(a) Colum-1 top end at +1.5% drift   (b) Column-2 top end +1.5% drift

(c) Colum-2 bottom end at +1.5% drift   (d) Column-1 top end view at +1.5% drift
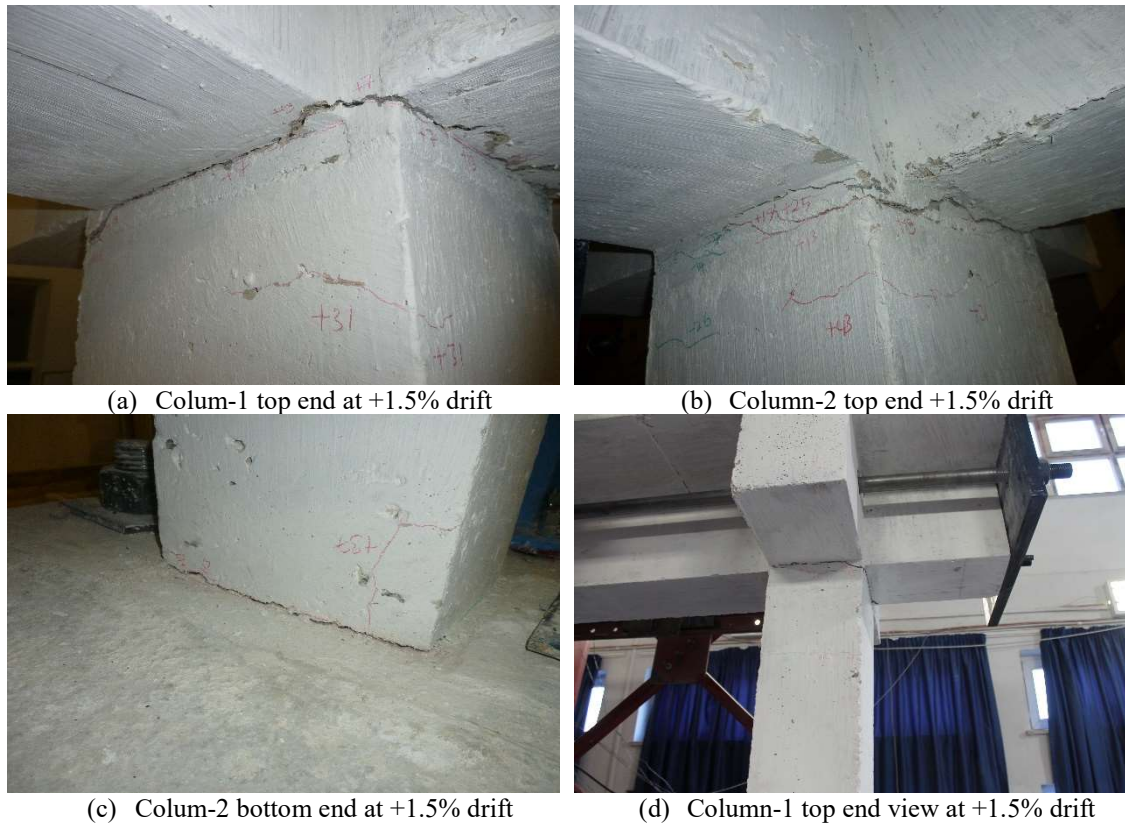
Figure 4.8. *Damage pattern of G1-2-Steel at maximum roof drifts*

The ends of strengthening steel bars are measured after the experiment to validate inelastic behavior and residual displacement. Nearly 1.5-2 cm elongation on the threaded portions of steel bars was measured while non-threaded portions have almost negligible elongation during the repeated loading. It means that the mid-portion of steel bars was in elastic range whereas the ends of bars showed nonlinear behavior with residual displacement. However, the fracture mechanism was not only developed in the nut connection of threaded portions but also observed in the mid-portion of threaded length. This indicates the uniform distribution of axial loading along the length of the strengthening bars. In addition, the views of strengthening steel bars after the experiment is shown in Figure 4.9.

(a) A general view (b) Measuring of threaded portions
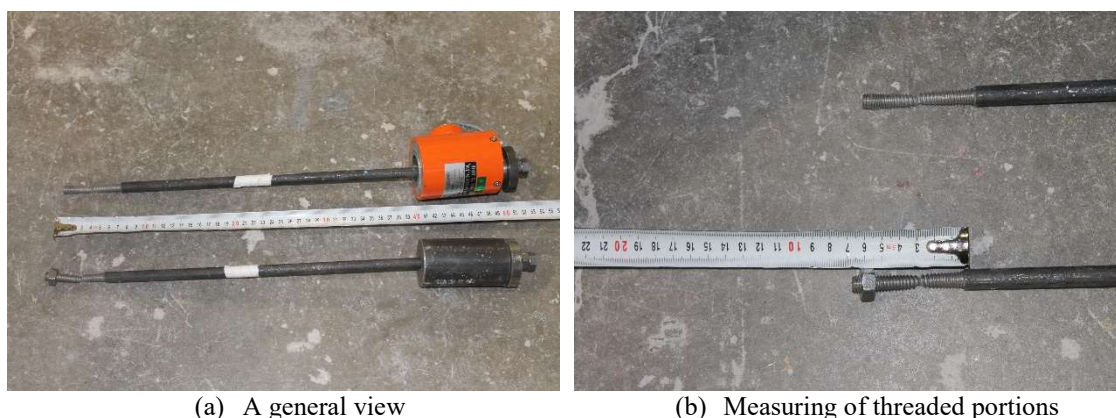
Figure 4.9. *Failure view of steel bars after the test*

Table 4.6. *The locations of main flexural cracks with the growth in width*

Cycle No.	Crack No. Corresponding first formation	Roof Displacement (mm)	Base Shear (kN)	Drift Ratio (%)	Crack width (mm)	Location of Crack (Name of Member - Side)
19	7	7.83	70.05	0.40	0.25	C1 - Left - Top - 1
26	14	-9.39	-69.45	-0.48	0.4	C1 - Back - Top - 1
31	7	14.96	78	0.76	0.8	C1 - Front - Top - 1
31	7	14.96	78	0.76	0.75	C1 - Right - Top - 1
32	14	-14.4	-77.1	-0.73	0.95	C1 - Back - Top - 1
37	13	19.65	78.9	1.00	1	C2 - Back - Top - 1
38	14	-20.07	-78.9	-1.02	1.4	C1 - Back - Top - 1
43	13	30.02	31.95	1.52	1.8	C2 - Back - Top - 1
43	7	30.02	31.95	1.52	1.8	C1 - Right - Top - 1

The measured crack widths and their locations are indicated in Table 4.6. In comparison to the reference frame, the G1-2-Steel has lower crack widths at 1.5% roof drift ratio. It also means that the imposed damage is comparable to the first specimen. The maximum crack widths were measured as 1.8 mm at +1.5% roof drift ratio after the strengthening bars were fractured.

4.3.1. Load vs. displacement relationship of steel bars

Two load cells with a capacity of 200 kN were placed on the steel bars to monitor the performance of steel bars during the test under lateral loading. Additionally, two LVDTs having a capacity of 200 mm was located at the level of strengthening bars with a purpose of measuring the lateral displacement. Knowing that the LoadCell-1 carries axial load if the actuator pulls the RC frame with a negative displacement. Contrary, the LoadCell-3 works when the actuator pushes the RC frame with a positive displacement.

68

This phenomenon is valid for other experiments when the load vs. displacement relationships of strengthening bars are introduced. Note that the strain gages connected to steel bars could not provide reasonable data for monitoring of strains since the mid-portion of steel bars could not exhibit inelastic behavior.

Figure 4.10 shows axial load and relevant lateral displacement history of steel bars. The permanent deformation of steel bars under axial loading is clear from this graph. According to given graph, the maximum axial load observed in the steel bars is 24.5 kN and 24.7 kN for pushing and pulling directions, respectively. It is possible to see similar hysteretic behavior of the steel bars under axial loading when considering the cyclic tension test results given in Figure 3.14 in terms of residual displacement. Keep in mind that the conventional steel bars had two different sections in this experiment like two different springs with different stiffnesses due to a dissimilarity in diameters of threaded and non-threaded portions.
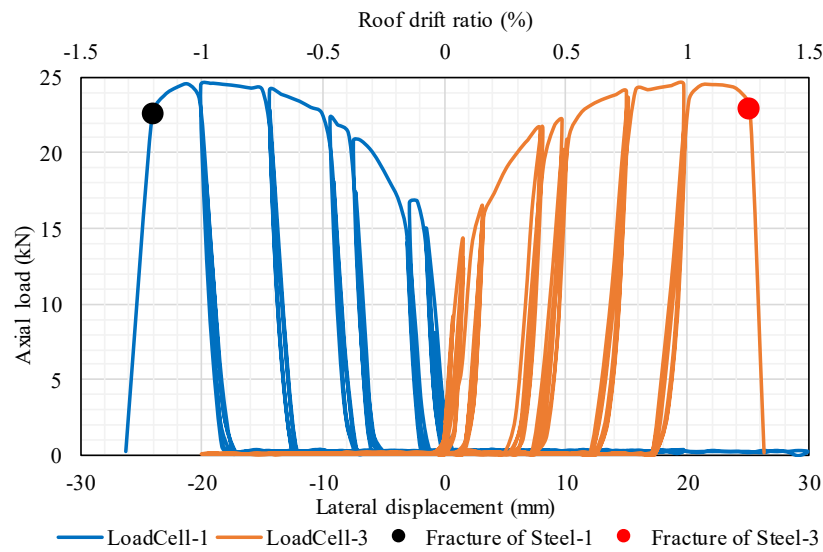
Figure 4.10. *Load vs. displacement history of Steel bars*

4.4. G1-3-CuAlMn Upgraded Frame

The third experiment was conducted by utilizing the SE CuAlMn SMA rods as strengthening materials. A methodology explained in previous chapters was used to enhance the seismic performance of RC frames by applying reversed cyclic lateral loading procedure given in Figure 3.42. The average concrete compressive strength was calculated as 17.04 MPa on the day of testing according to the uniaxial compression tests.

The lateral load capacity of the G1-3-CuAlMn is 85.8 kN in both pushing and pulling directions. The frame reached its ultimate load at +1.5% drift ratio in pushing direction whereas this load was obtained at -2% drift ratio in pulling direction. The number of lateral drift cycles tolerated by the CuAlMn-strengthened RC frame is 48. The load and displacement history of G1-3-CuAlMn is shown in Table 4.7.

Table 4.7. *The load and displacement history of G1-3-CuAlMn*

Cycle No.	Roof Displacement (mm)	Base Shear (kN)	Real Drift Ratio (%)	Expected Drift Ratio (%)
1	0.945	13.9	0.05	0.05
2	-1.005	-10.5	-0.05	-0.05
7	1.695	23.6	0.09	0.10
8	-2.07	-20.8	-0.11	-0.10
13	3.92	52.69	0.20	0.20
14	-3.93	-37.5	-0.20	-0.20
19	8.235	65.55	0.42	0.40
20	-7.365	-44.25	-0.37	-0.40
25	10.04	66.6	0.51	0.50
26	-9.96	-46.35	-0.51	-0.50
31	14.85	71.1	0.75	0.75
32	-15.10	-51.75	-0.77	-0.75
37	19.73	74.25	1.00	1.00
38	-19.86	-54.9	-1.01	-1.00
43	29.94	85.8	1.52	1.50
44	-29.3	-67.95	-1.49	-1.50
47	39.77	43.5	2.02	2.00
48	-39.2	-85.8	-1.99	-2.00

The hysteretic behavior of the G1-3-CuAlMn is given in Figure 4.11. Note that the strengthening rods in pushing and pulling directions were not fractured at the same lateral drift as it is shown in Figure 4.11. After imposing the first repeating cycle of 1.5% drift ratio, CuAlMn-3 fractured during the second positive cycle of 1.5% drift ratio. Then, the

RC frame sustained the second positive cycle of 1.5% drift ratio with only CuAlMn-4. Following the fracture of CuAlMn-3, the base shear was dropped to a lower level. Then, CuAlMn-4 was removed from the upgrading system. Next, in the last negative cycle of 1.5% roof drift, CuAlMn-1 and CuAlMn-2 did not fracture in contrast to the bars in pushing direction. Afterward, the first positive cycle of +2% drift ratio was completed without strengthening bars and the frame attained its ultimate load at -2% drift ratio while CuAlMn-2 fractured during this cycle. Finally, test was terminated due to the failure of strengthening bars in both directions after 2% drift ratio, which was repeated one time for positive and negative directions.
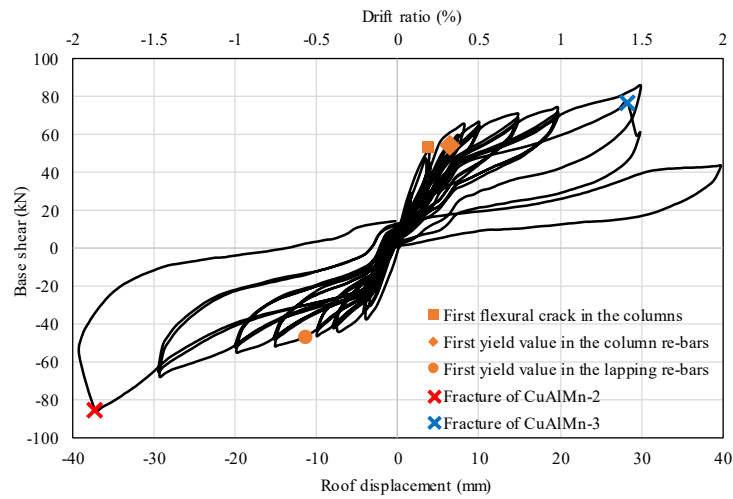
Figure 4.11. *Hysteretic behavior of G1-3-CuAlMn*

(a) +0.5% (b) +1%

(c) +1.5% (d) +2%
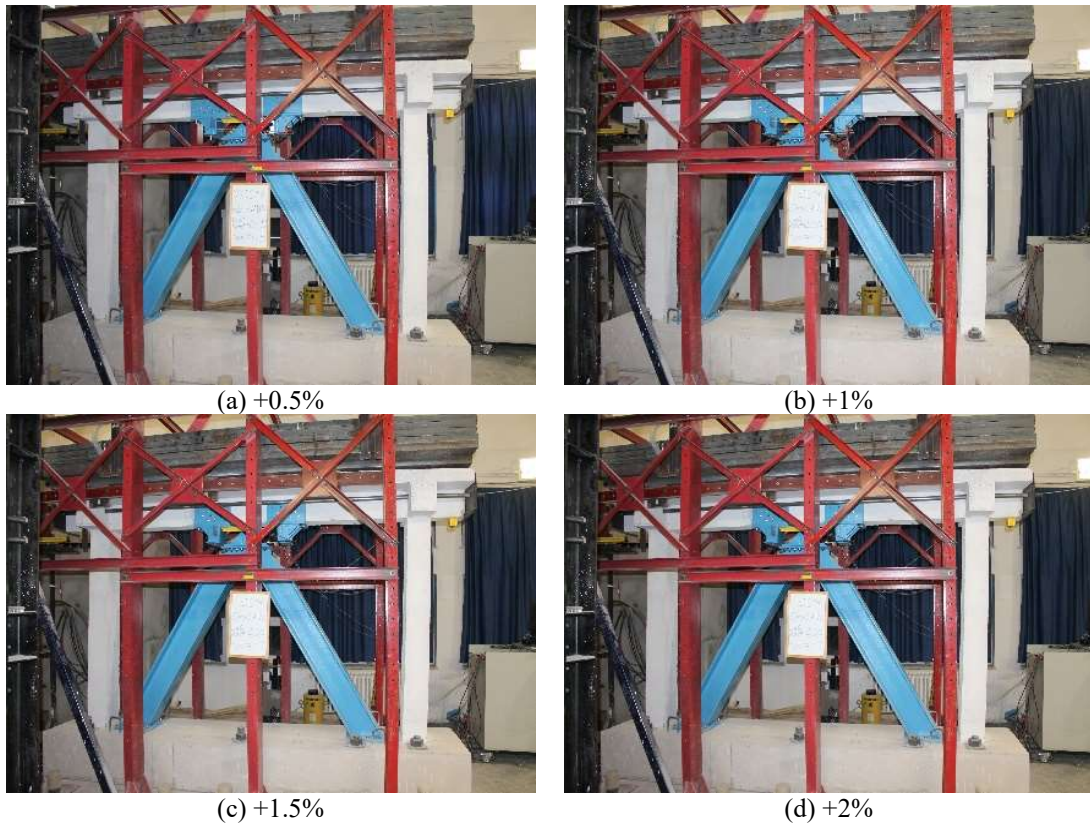
Figure 4.12. *Appearance of G1-3-CuAlMn at critical drift ratios*

The self-centering or re-centering of SMA materials is the most important property arised from the reversible transformations between austenite and martensite after the applied load is removed. Thus, the RC frame and SMA material experience unique re-centering ability with negligible small residual values compared to that of as-built specimen. Such a favorable behavior can be clearly observed in the hysteresis of G1-3-CuAlMn. Obviously, the implemented strengthening system provided the RC frame to come back zero position without residual values. The narrow band hysteresis is apparent in the CuAlMn-strengthened frame since the material exhibits this type of behavior in its own hysteretic loops. Following the apparence of flexural cracks in the columns, the frame lost its initial stiffness and inelastic deformations in the hysteresis took place. Here, the critical task is that the CuAlMn displays reversible transformations between austenite and martensite phases. Note that the austenite yielding strain of CuAlMn corresponds to the 0.1% lateral drift. So, the RC frame showed sharp increment following austenite yielding with post-yield stiffness while the strengthening rods were trying to exhibit martensitic behavior. After fracturing of CuAlMn rods, the observed base shear in the hysteresis is close to the reference frame as expected.

The first flexural crack formed at both column ends at +0.2% drift ratio and +3.92 mm lateral displacement. This first formation of crack occurred in 13th cycle. Additionally, the first yielding of column and lapping re-bars were measured at 6.525 mm and -11.37 mm lateral displacement in 25th and 32th cycles, respectively. The CuAlMn rods were not exposed to fracture at the same lateral drift due to possibly improper loading, different material characterization and threading process.

Table 4.8. *Critical failure steps in cracks, reinforcement yielding and fracture of strengthening bars*

	Cycle No.	Roof Displacement (mm)	Base Shear (kN)	Drift Ratio (%)
First flexural crack in the columns	13	3.92	52.6875	0.20
First yield value in the column re-bars	25	6.525	54.15	0.33
First yield value in the lapping re-bars	32	-11.37	-46.8	-0.58
Fracture of CuAlMn-3	45	28.275	76.95	1.44
Fracture of CuAlMn-2	48	-37.23	-85.8	-1.89
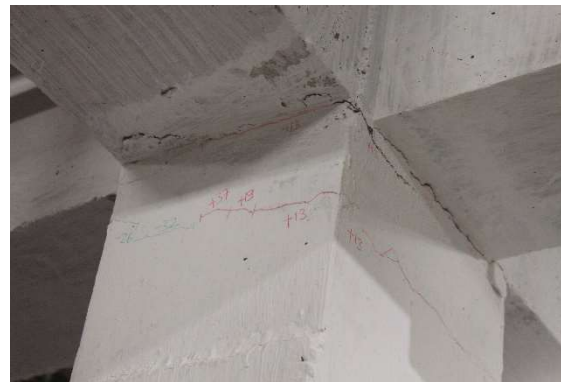
(a) First flexural crack in the columns   (b) Column top end at +1% drift ratio
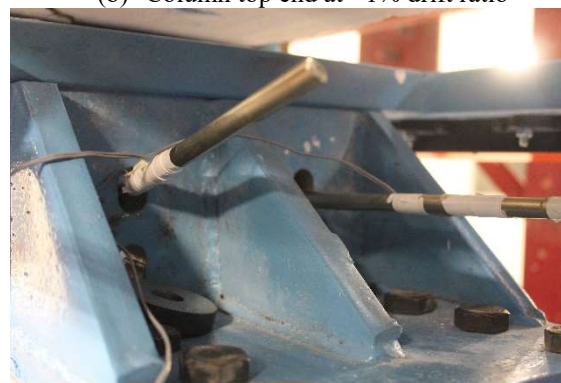
(c) Fracture of CuAlMn-3   (d) Fracture of CuAlMn-2

Figure 4.13. *Failure pattern of G1-3-CuAlMn at critical drift ratios*

Some damage pattern in the structural members during the experiment is presented in Figure 4.13. Following the +0.4% repeating drift cycles, the swelling of concrete at the column bottom end-foundation connection formed. This failure continued with separation of concrete from the foundation under the effect of lateral loading and bending moment. A serious crack at the beam-column joint was noticed at +2% drift ratio. Such a formation of crack also means that the cover concrete (unconfined concrete) lost its functionality and the section at this region has no longer sufficient flexural rigidity. The damage patterns of columns at maximum lateral drift ratio is displayed in Figure 4.14. Clearly, the plastic hinges were partially formed at the column ends. This means that the end region of the column members had still partial bending moment resistance at the end of the test.

| (a) Column back-top view at +2% drift ratio | (b) Column top view at +2% drift ratio |
| (c) Column bottom end at +1.5% drift ratio | (d) Column bottom end at -2% drift ratio |
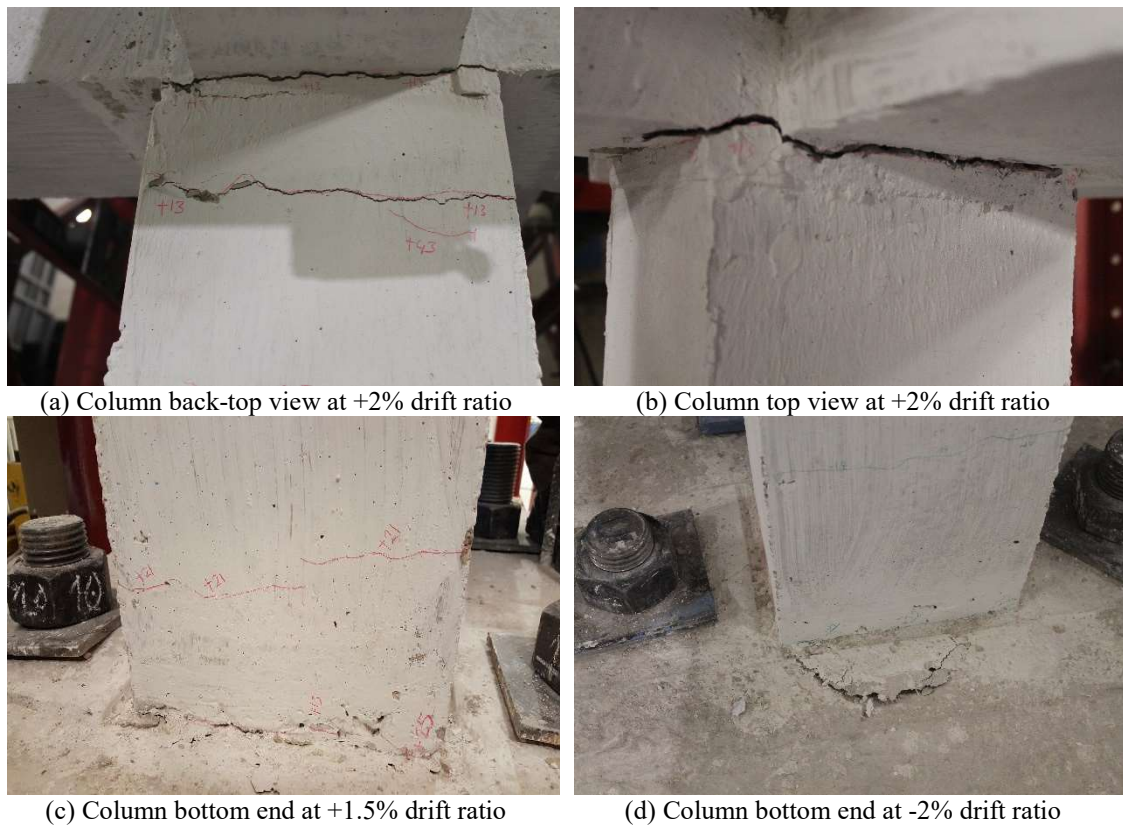
Figure 4.14. *Damage pattern of G1-3-CuAlMn at maximum roof drifts*

In addition to damage pattern of frame members, the observed failure mechanisms of CuAlMn rods are specifically shown in Figure 4.15. Another point of view in this experiment is that the upgrading bars exhibited some deformations during the test as well as fracturing. As the imposed strain level on the bars increased, unexpected failures in the

cross section of CuAlMn happened. Expectedly, it means that the diameter of the bars reduces proportionally related to growing axial load level. In conclusion, a total of two strengthening rods fractured in the system. The average length of threaded portions in the rods are measured as 50-53 mm at the ends of rods.

(a) View of CuAlMn rods before the test	(b) Measuring of diameter of CuAlMn-1 at -2% drift ratio
(c) Deformation of CuAlMn-1	(d) View of CuAlMn 1&2 after the test
(e) View of CuAlMn 3&4 after the test	(f) View of CuAlMn-2 aftet the test

Figure 4.15. *Failure pattern of CuAlMn rods during and after the test*

As a final remark, the main flexural cracks and their locations with crack widths are shown in Table 4.9. The first flexural cracks were marked on the columns in 13th pushing and 14th pulling directions. Since it is possible to see more than one crack on the column faces in the same lateral drift, there might be more than one crack width and location even if the crack number is the same. The maximum crack width was measured as 2.5 mm at

-1.49% drift ratio and 2.6 mm +2% drift ratio. Especially, a serious widening in crack width was visually observed after the frame attained 1% lateral drift.

Table 4.9. *The location of main flexural cracks with the growth in width*

Cycle No.	Crack No. corresponding first formation	Roof Displacement (mm)	Base Shear (kN)	Drift Ratio (%)	Crack width (mm)	Location of Crack (Name of Member - Side)
19	13	8.235	65.55	0.42	0.35	C2 - Back - Top - 1
25	13	10.035	61.65	0.51	0.5	C2 - Back - Top - 1
25	13	10.035	61.65	0.51	0.45	C1 - Front - Top - 1
31	13	14.85	66.15	0.75	0.9	C2 - Back - Top - 1
31	13	14.85	66.15	0.75	0.75	C1 - Front - Top - 1
32	14	-15.105	-56.7	-0.77	0.75	C2 - Front - Top - 1
37	13	19.725	69.3	1.00	1.3	C2 - Back - Top - 1
37	13	19.725	69.3	1.00	1	C1 - Front - Top - 1
38	14	-19.86	-59.85	-1.01	1.6	C2 - Front - Top - 1
38	14	-19.86	-59.85	-1.01	1.7	C1 - Back - Top - 1
43	13	29.94	80.85	1.52	2.5	C2 - Back - Top - 1
43	13	29.94	80.85	1.52	1.8	C1 - Front - Top - 1
43	13	29.94	80.85	1.52	0.5	C1 - Front - Top - 2
44	14	-29.295	-72.9	-1.49	2.5	C2 - Front - Top - 1
44	14	-29.295	-72.9	-1.49	2.5	C1 - Back - Top - 1
47	13	39.765	38.55	2.02	2.6	C1 - Front - Top - 1
47	13	39.765	38.55	2.02	1.1	C1 - Front - Top - 2

4.4.1. Load vs. displacement relationship of CuAlMn bars

The third test finalized with a strengthening process with superelastic CuAlMn SMA bars. As being in previous and next experiment, there were again two LoadCells and LVDTs measuring the imposed axial load on the bars and displacement. The graphical illustration is given in Figure 4.16 for axial load vs. displacement relationship of G1-3-CuAlMn. Initially, there is a salient difference in the curves corresponding to different loading directions because of the fracturing of CuAlMn bars at the different drift ratio. However, the deformation recovery of CuAlMn SMA bars is apparent in the figure with the effect of superelastic property. It can be said that the re-centering property of SE CuAlMn SMA bars without any residual deformation is observed during the experiment. Also, this property can be viewed in the hysteretic behavior of G1-3-CuAlMn globally. The general trend observed in load vs. displacement relationship of CuAlMn bars is similar to the cyclic tension tests of dog-bone shaped CuAlMn specimens. Furthermore,

starting of martensitic behavior is obvious for CuAlMn-1 while the frame sustains -2% lateral drift in the following figure. The axial load capacity of CuAlMn bars were measured as 32.66 kN and 21.38 kN in pulling and pushing directions, respectively.
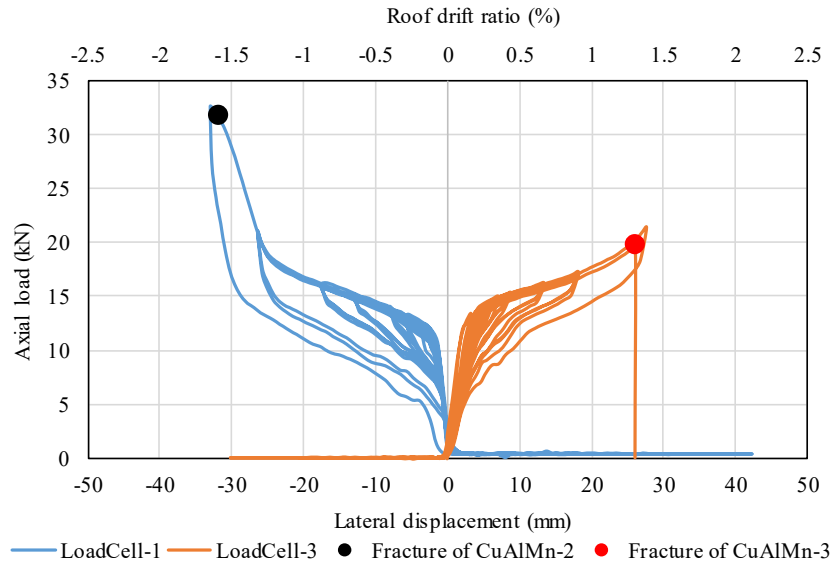
Figure 4.16. *Load vs. displacement history of SE CuAlMn bars*

4.4.2. Stress vs. strain relationship of CuAlMn bars

The stress vs. strain relationships of CuAlMn bars in the forward and backward directions are displayed in Figure 4.17 and Figure 4.18. The strain gages attached on the CuAlMn rods provided us information regarding the strain level of rods while they were axially loaded. Moreover, the stress parameter can be easily calculated using the load and geometric dimension information. Here, the observed visual trend in the figures is similar to each other although the numerical values in strains differ from greatly. The source of variation in strain distribution can be resulted from reliability of strain gage data. The forward and reverse transformations take place during loading and unloading process in the SMA bars. Thus, the residual strain values are very small when the material tries to come back to its undeformed position. Finally, the superelastic effect is clear in the following figures.
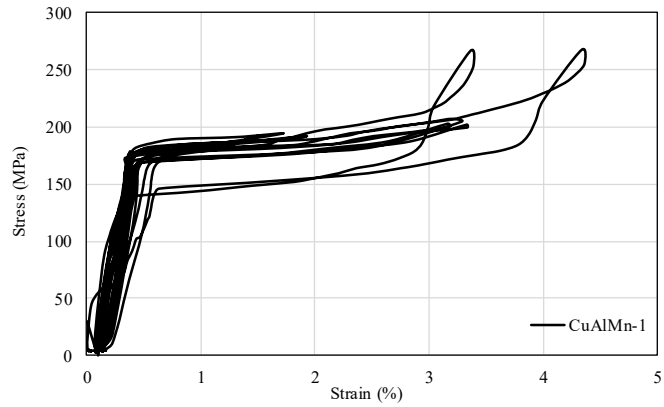
Figure 4.17. *Stress vs. strain relationship of CuAlMn-1*
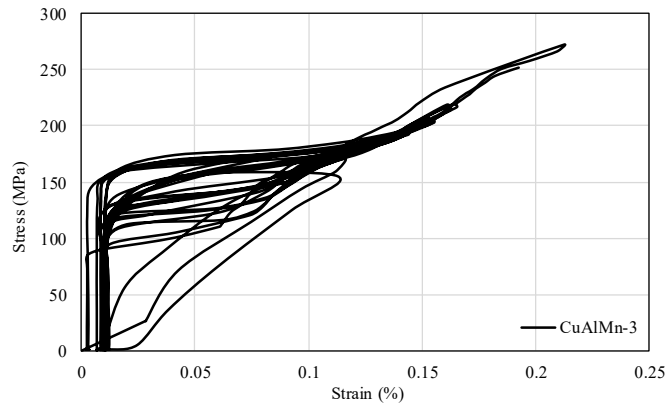
Figure 4.18. *Stress vs. strain relationship of CuAlMn-3*

There is a moderate difference in the shape of stress vs. strain graphs of CuAlMn rods. It must be clearly understood here that the strain gage position along the effective length of the rods is critical to get true relation. But, the maximum stress could not be occurred at this point where the strain gage is attached. In conclusion, the shape of stress vs. strain relationship of the CuAlMn rods are mostly similar in terms of general superelastic trend and reversible transformations but there is a difference in the strain level and unloading path.

4.5. G1-4-NiTi Upgraded Frame

The final experiment of this thesis study is called as G1-4-NiTi since the strengthening materials used in combination with RC frame is SE NiTi SMA bars. The same loading protocol was applied to this strengthened RC frame as in the case of previous experiments. The average concrete compressive strength obtained from cylindirical concrete samples through uniaxial compression test at the test day is 15.82 MPa.

The load and displacement history of G1-4-NiTi at the first cycles of loading protocol is given in Table 4.10. NiTi-strengthened frame gained its maximum lateral load at 1.5% roof drift as 159.15 kN in forward and backward directions, which corresponds to 43th and 44th cycles. The experiment was terminated at 2% drift ratio corresponding 48 cycles to be consistent previous tests although the NiTi rods were not fractured. Besides, the beam shear failure took place at the location where the U-shaped plates was connected for strengthening purposes. This caused the termination of the test.

Table 4.10. *The load and displacement history of G1-4-NiTi*

Cycle No.	Roof Displacement (mm)	Base Shear (kN)	Real Drift Ratio (%)	Expected Drift Ratio (%)
1	0.945	11.4	0.05	0.05
2	-1.005	-25.2	-0.05	-0.05
7	1.695	25.95	0.09	0.10
8	-2.07	-40.65	-0.11	-0.10
13	3.87	49.35	0.20	0.20
14	-3.96	-59.7	-0.20	-0.20
19	7.86	80.7	0.40	0.40
20	-7.83	-89.4	-0.40	-0.40
25	9.705	94.05	0.49	0.50
26	-9.795	-103.05	-0.50	-0.50
31	14.91	127.2	0.76	0.75
32	-14.78	-135.3	-0.75	-0.75
37	19.89	147.6	1.01	1.00
38	-19.61	-149.1	-1.00	-1.00
43	29.36	159.15	1.49	1.50
44	-29.78	-159.15	-1.51	-1.50
47	38.81	159	1.97	2.00
48	-38.96	-155.55	-1.98	-2.00
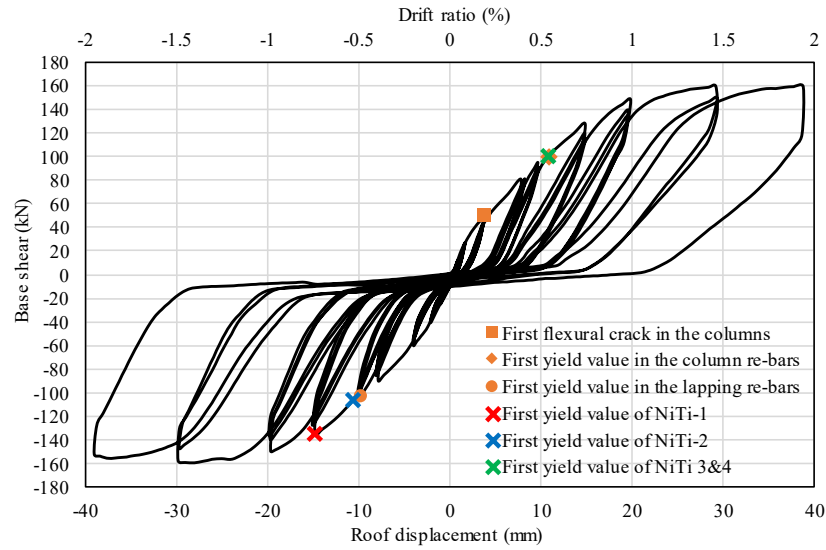
Figure 4.19. *Hysteretic behavior of G1-4-NiTi*

The base shear vs. lateral displacement relation of G1-4-NiTi is illustrated in Figure 4.19. In the beginning of cyclic loading, the small fully flag-shaped loops were observed in the hysteretic curves. Then, the shape of hysteresis was gradually looked like the reference and second specimen as the frame reached higher ultimate loads. Note that the loading and unloading paths have different stiffness especially up to 0.5% roof drift. So, the frame lost its resistance against lateral loading and the horizontal plateau is clear up to a specific point for loading and unloading paths. The base shear demand increased with the applied reversed cyclic displacement protocol and the concrete material around the U-shaped was severely cracked due to combination of shear and bending moment. For instance, the ultimate load value of G1-4-NiTi is two times greater than the ultimate load value of G1-3-CuAlMn at 1% drift ratio. More clear figures demonstrating each hysteresis loop are given in Figure 5.1, Figure 5.17-Figure 5.19.

(a) +0.5%	(b) +1%
(c) +1.5%	(d) +2%
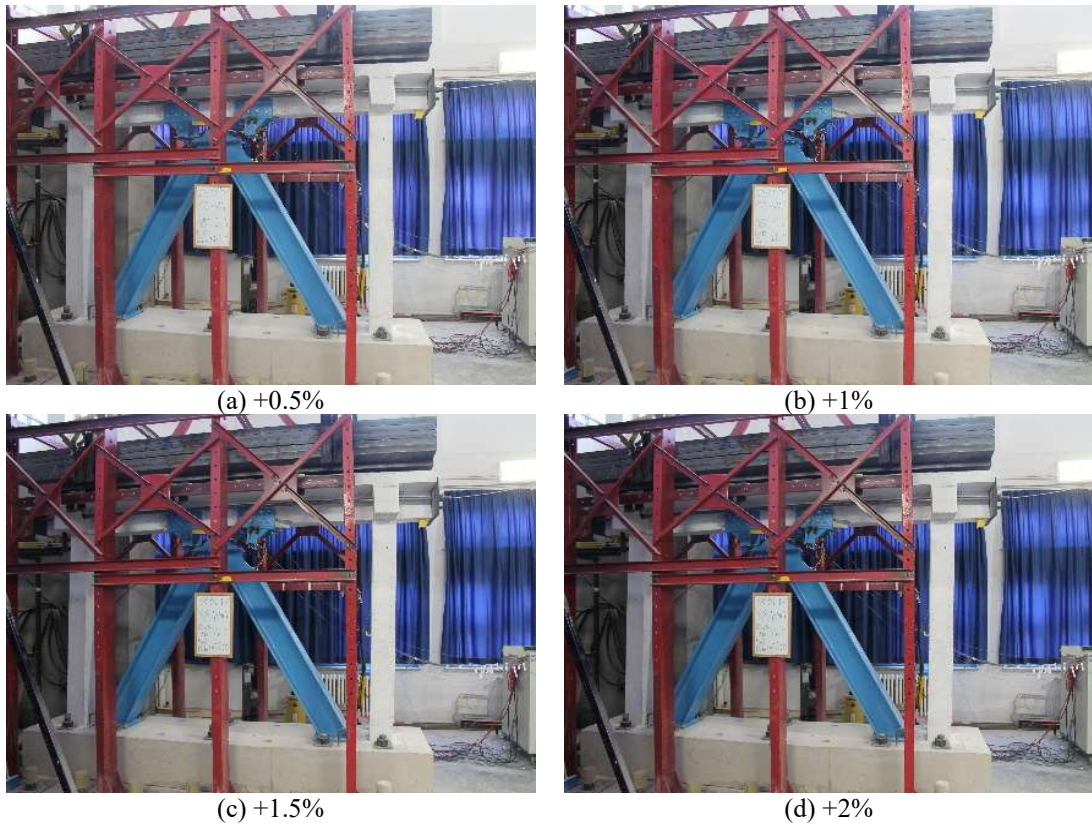
Figure 4.20. *Appearance of G1-4-NiTi at critical drift ratios*

Some critical damage patterns are numerically given in Table 4.11. First flexural crack was formed at +0.2% drift ratio according to the following table and yielding of re-bar was firstly measured in the lapping reinforcement. Additionally, first yielding steps of NiTi SMA bars are given in this table. Interestingly, the NiTi bars in backward direction yielded at the same drift cycle but in different displacement step contrary to the NiTi bars in forward direction. The reason of such an unexpected yielding step in backward loading might be attributed to the reliability of strain gage and difference in material characterization. Keep in mind that the yielding of NiTi bar is calculated considering the austenite yielding strain.

Table 4.11. *Critical failure steps in cracks, reinforcement and strengthening bars*

	Cycle No.	Roof Displacement (mm)	Base Shear (kN)	Drift Ratio (%)
First flexural crack in the columns	13	3.87	49.35	0.20
First yield value in the column re-bar	31	10.83	99.9	0.55
First yield value in the lapping re-bar	26	-9.795	-103.05	-0.50
First yield value of NiTi-1	32	-14.78	-135.30	-0.75
First yield value of NiTi-2	32	-10.56	-105.752	-0.54
First yield value of NiTi 3&4	31	10.83	99.9	0.55

(a) First flexural crack in the columns	(b) Column top end at +1% drift ratio
(c) Column top end at +2% drift ratio	(d) Column bottom end at -2% drift ratio
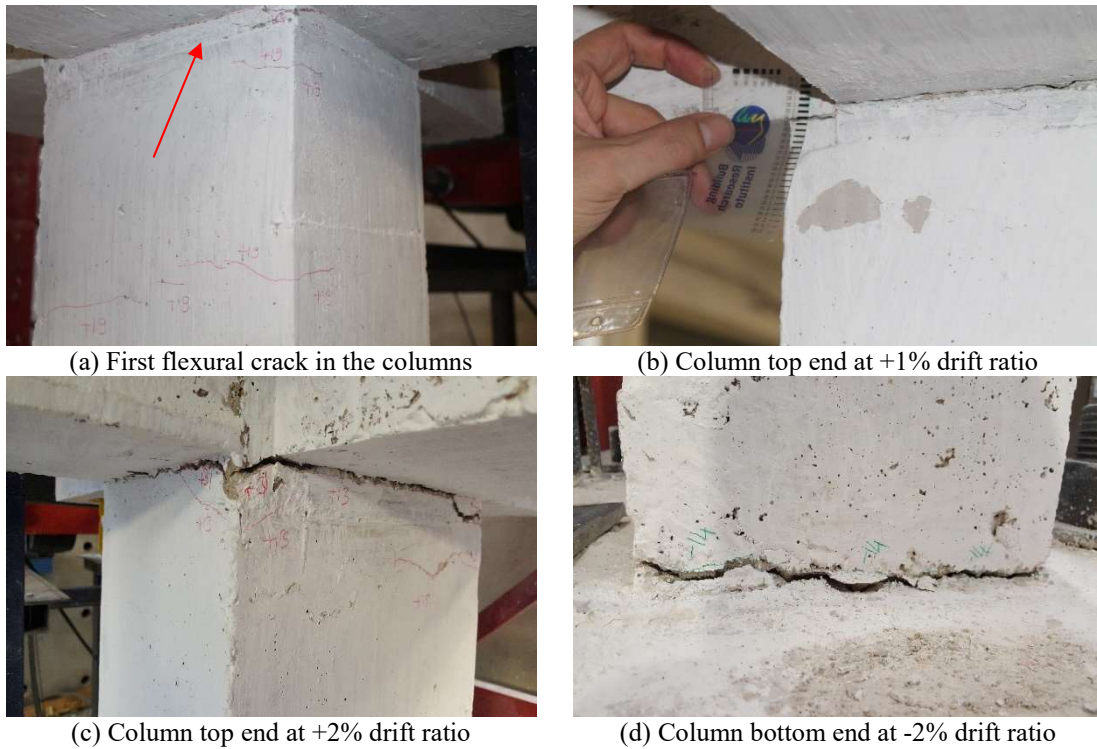
Figure 4.21. *Damage pattern of G1-4-NiTi at critical roof drifts*

The flexural cracks observed in the column members during the cyclic loading in G1-4-NiTi is given in the above Figure 4.21. As expected, the end regions of column members were exposed to flexural cracks due to bending moment. Moreover, the failure damage pattern of beam, where the U-shaped plates were connected, during the lateral loading is presented in Figure 4.22. In this experiment, the base shear demand imposed on the test specimen was noticeably greater than the second and third experiments. Thus, this higher loading caused forming of severe concrete cracking in the beam concrete around the U-shaped plates. Finally, the stable and proper position of U-shaped plates were seriously rotated by the lateral loading. Then, the imposed lateral drift could not be

fully transmitted to the NiTi rods due to the damage in the beam and hence rigid body rotation of the U-shaped plates.

(a) Crack formation at -0.2% drift ratio	(b) Concrete cracking +0.75 drift ratio
(c) Concrete cracking +1% drift ratio	(d) Concrete spalling at -2% drift ratio
(e) General view at +1.5% drift ratio	(f) General view at -2% drift ratio

Figure 4.22. *Failure pattern of U-shaped plates during cyclic loading*

As illustrated in Figure 4.22(f), the connection between the beam concrete and U-shaped plates were subjected to serious lateral loading since the axial load level carried by NiTi rods was relatively higher than other strengthening rods. From the beginning of experiment, firstly hairline cracks were formed around the U-shaped plates. Then, these cracks widened and propagated with the effect of lateral loading. This lateral load caused greater shear and bending moment demand around U-shaped plates and the applied bolted

connection detailing on RC beam did not meet such a demand level. Next, the concrete material reached ultimate strain level and failed in principal tension at the end of the test.

(a) Length of threaded portion-1 before the test

(b) Length of threaded portion-2 before the test

(c) Measuring of section width before the test

(d) Measuring of section height before the test

(e) Length of the NiTi bar after the test

(f) Length of threaded portions after the test

Figure 4.23. *View of NiTi rods before and after the test*

Figure 4.23 illustrates the state of the NiTi rods before and after the experiment to make comparison. Since the NiTi rods did not exhibit martensitic behavior according to the frame's hysteresis and load vs. displacement relationship of NiTi rods as well as the strain gage data, there was no visible or measurable elongation in both effective length and threaded portions of the NiTi rods. Only austenite transformation took placed in the rods with nearly zero residual strain. The measurements of the sections after the test is a proof of such a behavior.

The summary about the formation of cracks and their locations is presented in Table 4.12. In this table, a different type of crack formed around the U-shaped plates is introduced, unlike the tables presented in previous chapters. The maximum crack width in this test was measured as 3.5 mm at 48th cycle corresponding to 151.95 kN base shear and -2% drift ratio. A serious increment in crack widths is detected after 1% lateral drift ratio. Note that the cracks around the U-shaped plates lost measurable positions after a period of test since the width of the cracks visibly enlarged and the severe cracking of concrete started.

Table 4.12. *The locations of main flexural cracks with the growth in width*

Cycle No.	Crack No. Corresponding first formation	Roof Displacement (mm)	Base Shear (kN)	Drift Ratio (%)	Crack width (mm)	Location of Crack (Name of Member - Side - Region)
22	22	-8.07	-85.2	-0.41	0.5	Beam - U-shaped
25	7	9.705	94.05	0.49	0.45	C1 - Front - Top - 1
26	22	-9.795	-103.05	-0.50	0.55	Beam - U-shaped
26	8	-9.795	-103.05	-0.50	0.5	C1 - Back - Top - 1
31	7	14.91	127.2	0.76	1	C1 - Front - Top - 1
32	22	-14.775	-135.3	-0.75	2	Beam - U-shaped
32	8	-14.775	-135.3	-0.75	0.8	C1 - Back - Top - 1
37	7	19.89	147.6	1.01	1.4	C1 - Front - Top - 1
38	22	-19.605	-149.1	-1.00	3	Beam - U-shaped
38	8	-19.605	-149.1	-1.00	1.1	C1 - Back - Top - 1
43	7	29.355	136.65	1.49	2	C1 - Front - Top - 1
44	8	-29.775	-157.2	-1.51	2	C1 - Back - Top - 1
47	7	38.805	158.85	1.97	3	C1 - Front - Top - 1
48	8	-38.955	151.95	-1.98	3.5	C1 - Back - Top - 1

4.5.1. Load vs. displacement relationship of NiTi bars

The last experiment was accomplished with superelastic NiTi SMA bars. This experiment was terminated before the strengthening bars fractured since U-shaped plates lost its functionality and 2% drift ratio was enough to make comparison with others. The load vs. displacement history of NiTi bars is presented in Figure 4.24. A maximum load of NiTi bar measured in positive direction is 65.08 kN whereas this load is 59.89 kN in opposite loading direction. A fully and successful re-centering could not be observed in the following figure due to the fact that the self-centering mechanism could not be

activated. The observed residual deformation arised due to rotation of U-shaped plates as a result of unsatisfactory connection detailing.
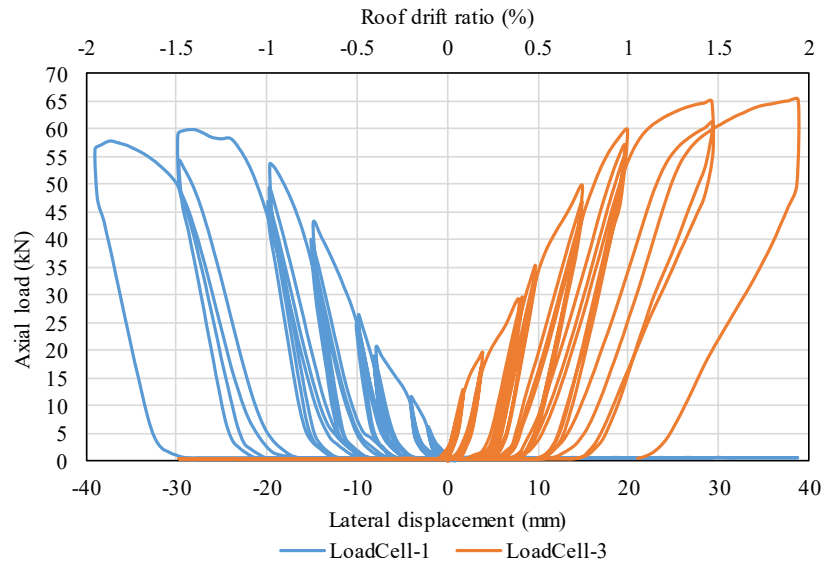
Figure 4.24. *Load vs. displacement history of SE NiTi bars*

4.5.2. Stress vs. strain relationship of NiTi bars

As presented in previous chapters, the stress vs. strain relation of NiTi rods are calculated using the information obtained from strain gage data, loadcell and geometric dimensions. Two graphs are demonstrated regarding the imposed strain and normal stress in Figure 4.25 and Figure 4.26. The difference in stress vs. strain distribution is apparent in the following figures. The source of such a dissimilarity might be linked with the position and reliability of strain gage and difference in material characterization. It is more logical to have comment about Figure 4.26 since the graph reflects the expected behavior. Even if the frame and NiTi rods did not exhibit re-centering in the hysteresis, such a mechanism is obvious in the mentioned figures.
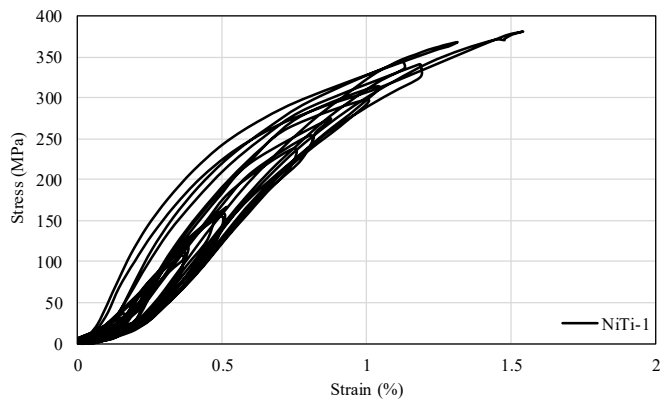
Figure 4.25. *Stress vs. strain relationship of NiTi-1*
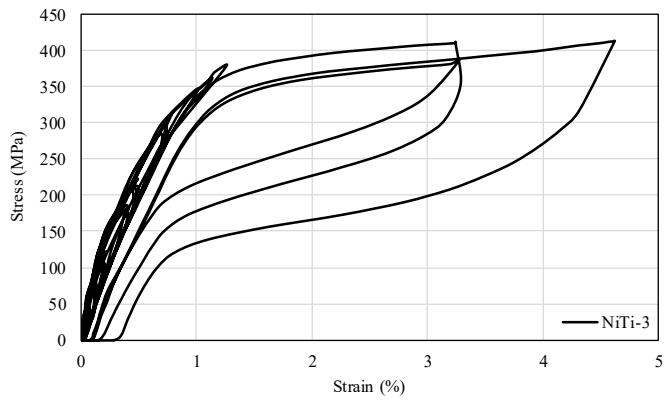
Figure 4.26. *Stress vs. strain relationship of NiTi-3*

5. DISCUSSION OF THE TEST RESULTS

The results of the RC frame tests are presented and discussed in this chapter. It is important to investigate the test results in terms of some seismic demand parameters to realize the advantages or disadvantages of the proposed strengthening system in enhancing the frame performance. Here, the test results are compared considering strength, stiffness, dissipated energy, ductility, equivalent viscous damping, re-centering property, strain gages data and ambient vibration results in detail.

5.1. Hysteretic Response of Frames

The hysteretic responses of the test specimens are considered to be the basis for the evaluation of RC frame test results among the seismic response parameters. The base shear vs. roof displacement relationships of frame tests are given in Figure 5.1. Here, the upper and lower limit of vertical and horizontal axis of hysteretic loops are changed considering maximum lateral displacement (G1-1-Reference) and maximum ultimate load (G1-4-NiTi) in each row. The aim of such a demonstration is to make comparison among the seismic responses of frames. In the first row, the hysteretic curves are shown as they are. Then, the vertical axes of the loops are shown taking the upper and lower limit as maximum load. At the same time, the horizontal axis is kept as constant as they are. In the third row, a similar action performed for horizontal axes of hysteresis. Based on the maximum lateral displacements and drifts, the horizontal axes of hysteresis are updated keeping the vertical axes as constant. In the last row, both upper and lower limit of hysteretic curves are changed in vertical and horizontal axes considering the ultimate load of G1-4-NiTi and maximum lateral displacement of G1-1-Reference. In conclusion, hysteretic trends of four different RC frames are introduced updating the vertical and horizontal axis of hysteresis in order to display the difference in seismic response of the frames.

Firstly, it is clear that the maximum lateral displacement (G1-1-Reference) and the maximum base shear (G1-4-NiTi) draw attention when the following figures are considered. Besides, the ductile behavior of G1-1-Reference frame is obvious in the last row of this figure. Even if the Steel and CuAlMn-strengthened frames have similar base shear values, there is visible difference between the shape of hysteretic curves due to material characteristics.
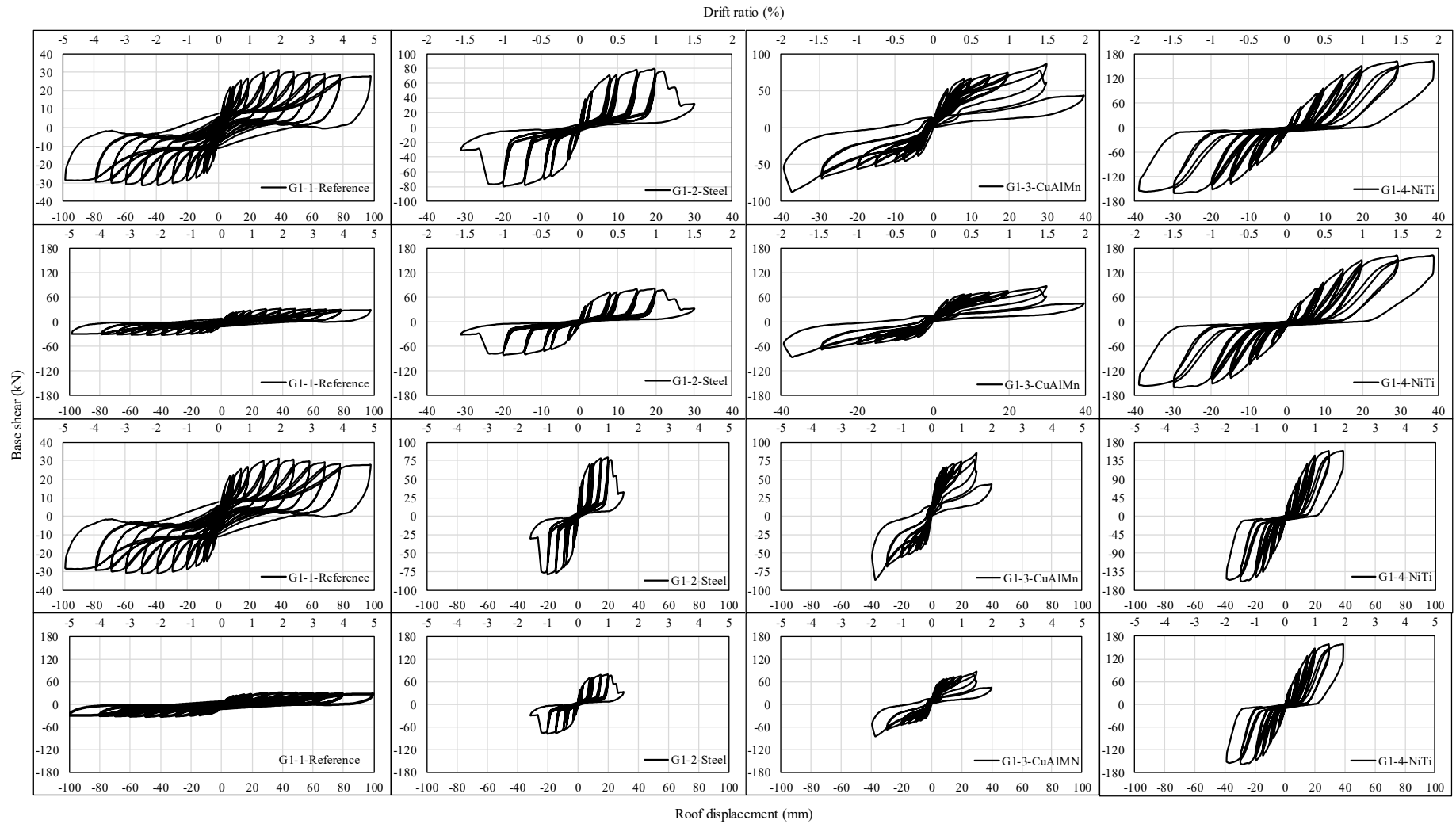
Figure 5.1. *Comparison of frame base shear vs. roof displacement relationships*

5.2. Strength

To be able to investigate the efficacy of the proposed strengthening system, primarily the strength parameter is investigated in detail. What is known from the experiments that each frame with or without upgrading system showed different behavior under the effect of reversed cyclic loading. The ultimate load capacity of frames and strength deterioration are firstly computed in this context. So, the numerical values of maximum lateral load of frames and the corresponding roof displacements are demonstrated in Table 5.1. Also, the strengthened specimens are compared to that of non-strengthened reference specimen in terms of lateral load capacity. In this table, the forward and backward loadings are introduced seperately to show the differences.

G1-4-NiTi has the highest lateral load capacity of 159.2 kN among the tested frames. It gained its ultimate load at 1.5% drift ratio in both forward and backward loading. The second tested frame, G1-2-Steel, reached the maximum horizontal load capacity at the earliest in 1% repeating drift cycle. Contrary, the reference specimen attained its ultimate load at -2.5% drift ratio. All seismically upgraded frames have greater ultimate load than the reference frame. According to the comparison, the lateral load capacity of G1-4-NiTi is 5.1 times greater than the G1-1-Reference. However, the minimum changing ratio in ultimate load is obtained in G1-2-Steel as 2.5. It can be easily said that all strengthening materials and proposed system increased the peak lateral load resisted by the frame.

It is possible to interpret the strength of each frame by introducing the envelope curves. They are obtained by combining the point of ultimate load in the hysteresis and corresponding roof displacement for the first positive and negative repeating cycle of loading history. The envelope curves of tested RC frames are illustrated in Figure 5.2. The maximum drift ratio, which is common for all tested specimens, is 1.5%. It should also be remembered that the only difference between experiments is the strengthening materials used in the system. Accordingly, the mechanical properties of materials are directly effective on the seismic performance of tested frames as well as suggested strengthening system. As displayed in Figure 5.2, the experiment with SE NiTi SMA bars were terminated at 2% drift ratio although the bars were not fractured. It is due to the fact that the frame reached its comparable load and displacement value and the U-shaped plates lost its functionality. For this reason, there is no sudden decrease in lateral load of

G1-4-NiTi. Also, it is clear that this curve has a yielding point and reached a plateau before 2% roof drift ratio. Furthermore, the reference specimen did not display a serious decline in its ultimate load. It followed very flat plateau in which the load goes down very gradually, and roof displacement raises. The sudden drop in lateral load capacity can be observed in G1-2-Steel and G1-3-CuAlMn following the fracturing of the strengthening bars.

Table 5.1. *Lateral strength values of tested RC frames*

Type of Loading	Properties and Units		G1-1 Reference	G1-2 Steel	G1-3 CuAlMn	G1-4 NiTi
Forward Loading (Pushing)	Ultimate Lateral Load, V_{max}^+	(kN)	31.2	78.9	85.8	159.2
	Change in V_{max}^+ compared to that of ref. Frame	(kN/kN)	1	2.5	2.8	5.1
	Roof Displacement at Ultimate Load	(mm)	39.0	19.7	29.9	29.4
	Drift Ratio at Ultimate Load	(%)	2.0	1.0	1.5	1.5
	Cycle No. at Ultimate Load		47	37	43	43
Backward Loading (Pulling)	Ultimate Lateral Load, V_{max}^-	(kN)	-31.2	-78.9	-85.8	-159.2
	Change in V_{max}^- compared to that of Ref. Frame	(kN/kN)	1	2.5	2.8	5.1
	Roof Displacement at Ultimate Load	(mm)	-49.1	-20.1	-39.8	-29.8
	Drift Ratio at Ultimate Load	(%)	-2.5	-1.0	2.0	-1.5
	Cycle No. at Ultimate Load		47	38	48	44
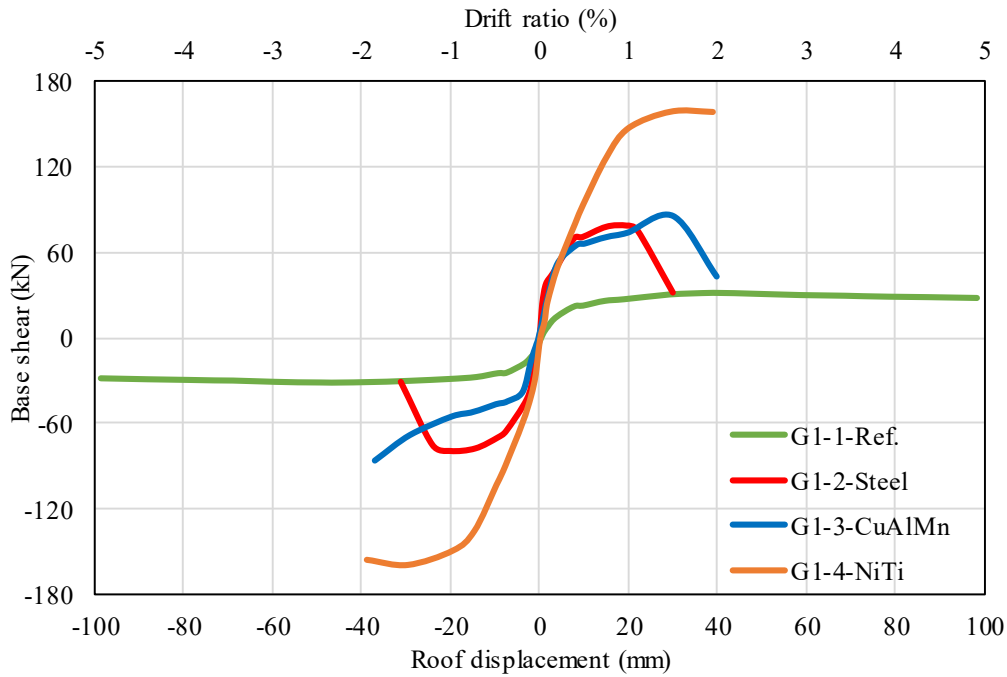
Figure 5.2. *Response envelope curves of tested RC frames*

5.3. Stiffness

In the analyses of seismic response parameters of frames, the lateral stiffness is an essential criterion to assess the performance of RC frames under consideration. It states a relationship between applied loads to the structure and its response.

Within the scope of this study, the RC frames with a flexurally dominated behavior was designed and constructed, and such a behavior observed in the tested RC frames. Accordingly, what type of stiffnesses we are interested in this study is the lateral stiffness of the frame system. Also note that the total lateral stiffness of system is directly affected by member stiffnesses.

There are various descriptions explained in the literature for stiffness parameter. Figure 5.3 displays a capacity curve including top lateral displacement and total base shear of a system subjected to lateral loading. In this graph, two different stiffness parameters are indicated; K_0 is the initial slope representing the elastic stiffness of the structure (first approach) and K_s is the secant stiffness (second approach).

A total of three different stiffness calculations are made in this study to discover the variations in stiffness of four tested RC frames. The estimated stiffness values are obtained by using the capacity curve considering positive or forward loading of specimens. First of all, the initial stiffnesses are calculated by taking the slope of line in the elastic portion of backbone curve. Then, a line starting from origin and intersecting the 60 percent of the ultimate load of each frame ($0.6V_{max}$) on the curve, as did in previous study conducted by Akın et al. (2011), is drawn. Afterward, the slope of this line gave the secant stifness of frames. The results are introduced in tabular form in Table 5.2. The aim of presenting two different estimations for stiffness parameter is to be able to make comparison and avoid any probable miscalculations.
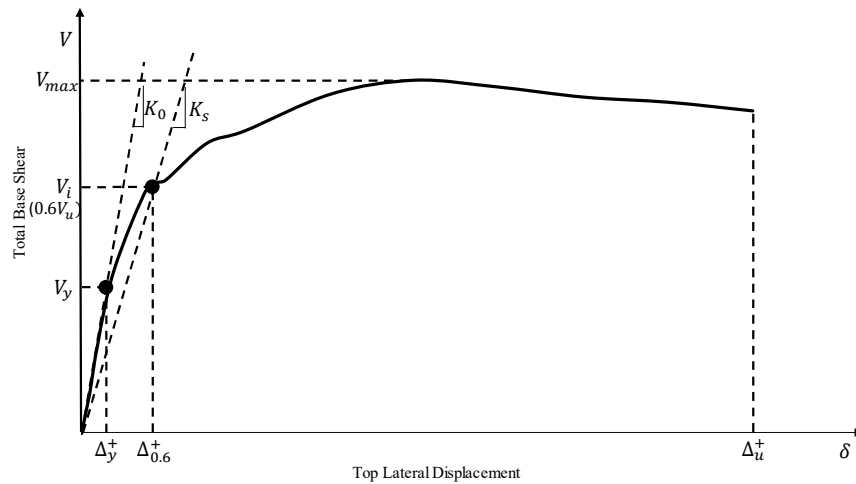
Figure 5.3. *Definition of structural stifnesses*

As shown in Table 5.2, the initial stiffness values of strengthened frames are higher than the reference frame. Generally, the initial stiffness, K_0, is greater than the secant stiffness, K_s, for conventional materials of construction (Elnashai and Sarno, 2008, p. 56). This statement is valid in initial stiffness values of tested RC frames within the scope of this study. It is a fact that the material properties such as the elastic Young's modulus and the elastic shear modulus directly affect the response of frames to the seismic actions. Unlike the reference specimen, strengthening materials contributed to the lateral stiffnesses of the RC frames as proportionally with their rigidities. Expectedly, the initial stiffness of G1-2-Steel are greater than all the frames because of higher modulus of elasticity of conventional steel compared to that of other strengthening materials.

However, the effective area and length of the strengthening bars have a role in stiffness calculations. The reason of why the initial stiffness value of NiTi experiment is greater than the G1-3-CuAlMn is that the frame with NiTi rods showed a rigid performance in the first ascending part of elastic portion due to higher Young modulus. However, it is not expected behavior that the secant stiffness of G1-4-NiTi is less than the G1-3-CuAlMn. It is most probably due to the fact that U-shaped plates could not resist the lateral loading and they lost their effective contribution gradually as the imposed deformation increases. Hence, NiTi-strengthened frame did not preserve initial rigidity as the roof displacements increased due to unexpected rotation of U-shaped plates. As a conclusion, all strengthening procedures increased the stiffness of RC frames compared to the reference frame.

Table 5.2. *Initial stiffness values of tested specimens*

Specimen	Initial stiffness K_0^+ (kN/mm)	Change in K_0^+ Compared to that of Ref. Frame	Secant stiffness K_s^+ (kN/mm)	Change in K_s^+ Compared to that of Ref. Frame
G1-1-Reference	7.35	1.00	3.77	1.00
G1-2-Steel	35.71	4.86	13.07	3.47
G1-3-CuAlMn	14.71	2.00	11.61	3.08
G1-4-NiTi	22.06	3.00	10.78	2.86

Thirdly and ultimately, the stiffness calculation is made according to cyclic response of RC frames. A peak-to-peak stiffness method is used here to obtain stiffness while the structural damage of members increases along with the reversed cyclic loading. The stiffness of the frame degrades at each loading cycle as the damage occurs. The peak-to-peak stiffness is represented as a slope of line connecting the ultimate two points of first cycles at each drift ratio in positive and negative side (Figure 5.4). Thus, the stiffness degradaration of frames are demonstrated by normalized stiffness degradation vs. roof drift ratio in Figure 5.5 and Figure 5.6. In the former figure, the stiffness values are normalized with respect to their first stiffness values obtained from first loading cycle. In the latter figure, the stiffness values are normalized with respect to the first stiffness value of the reference frame.
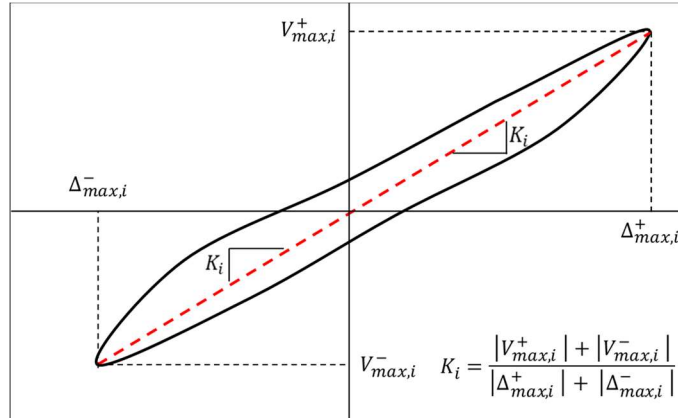
Figure 5.4. *Illustration for calculation of peak-to-peak stiffness*

,
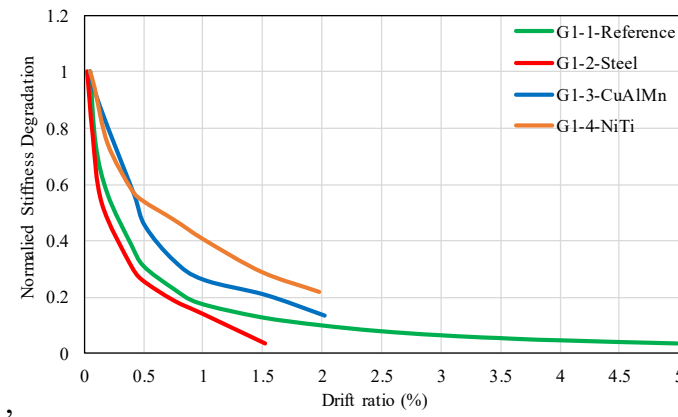
Figure 5.5. *Stiffness degradation curves-I (Normalized to their initial stiffness)*

It may be stated that the rigidity of the RC frames dropped sharply until they reached the lateral load capacity due to deterioration in the lateral resisting system. Then, the decreasing rate in the lateral stiffness happens more slowly. On the other hand, G1-2-Steel continued to lose its stiffness dramatically after 1% drift ratio corresponding its ultimate load point. Although the initial and secant stiffness of G1-2-Steel is higher in the beginning, a sharp decline took placed under the effect of applied lateral loads. In addition, it should be also underlined that the stiffness values obtained from peak-to-peak method are similar to the values calculated from initial stiffness calculations at the beginning. A smooth decrease occurred in the stiffness degradation of G1-3-CuAlMn to 0.5% roof drift ratio whereas other frames were exposed to a serious decline with regard to starting point. Another important observation on the degradation curve is that the stiffness of G1-2-Steel at 0.2% drift ratio is almost the same with G1-4-NiTi. Generally,

the observed trend in the second experiment is that it is more prone to loose its rigidity quickly. At the end of the test, G1-4-NiTi has the greatest peak-to-peak stiffness.
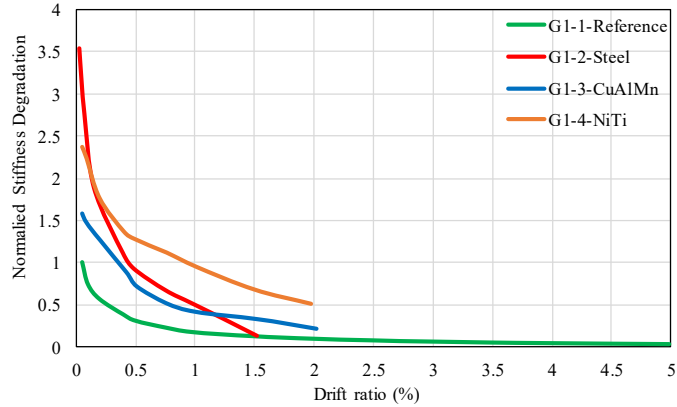
Figure 5.6. *Stiffness degradation curves-II (Normalized to the initial stiffness of the Reference Frame)*

In the above figure, the peak-to-peak stiffness values are presented by normalizing the results relative to the reference specimen. As expected, the G1-2-Steel has the highest stiffness value in the beginning. But then, G1-4-NiTi leads after 0.4% roof drift ratio due to sharp decline in the stiffness of Steel-strengthened frame. Also note that the peak-to-peak stifness of G1-3-CuAlMn is calculated without strengthening bars in the positive loading of 2% lateral drift. While the CuAlMn-strengthened frame tried to attain -2% lateral drift, the strengthening bars were fractured in the negative loading.

5.4. Dissipated Energy

The area under the lateral displacement vs. base shear curve gives us the energy dissipated by the frame during cyclic loading. Here, the dissipated energy is calculated by considering the area composed of force-displacement points for the first cyclic loading of each drift ratio. Other lateral drift cycles are neglected in dissipated energy estimations. This parameter informs us about the amount of energy dissipated at each different cyclic loading while the RC frame shows elastic and post-elastic behavior during lateral loading. The representative area under each complete displacement cycle is shown in Figure 5.7. Besides, the amount of energy absorbed by the frames in each different drift cycle is displayed in Table 5.3. Also, the comparison between the reference frame and other

strengthened frames is made in Table 5.3. The unit presented below is in "kN.m" or "kilojoules".
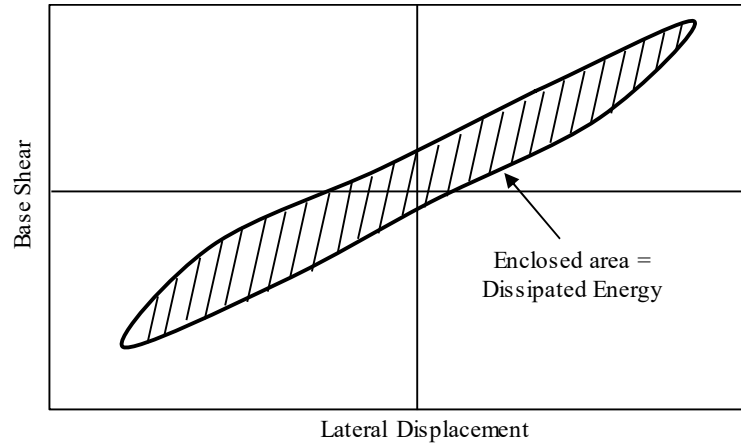
Figure 5.7. *The dissipated energy per each cycle by the frame*

The common drift ratio applied to all specimens is 1.5% and G1-4-NiTi has the highest dissipated energy value 5.99 kN.m at this drift. It is a general trend that NiTi-strenghtened frame absorbed the most seismic energy as the drift increases. The reason of such a remarkable ascending trend in this experiment comes from the nature of material characteristics. Remember that NiTi absorbed more energy during the cyclic tensile tests (Figure 3.23). Another interesting finding in Figure 5.8 is that the amount of energy dissipated by G1-2-Steel at 1.5% drift is greater than the G1-3-CuAlMn. It is again related to characteristics of material under given loading. The very narrow loops of CuAlMn during the cyclic tensile test before starting martensite phase can be considered as a noticeable cause for such a behavior. All of the frames tested showed more energy dissipation than reference frame under given lateral loading up to 2% roof drift ratio.
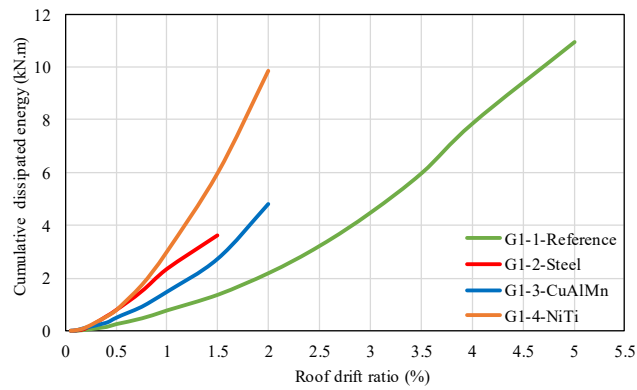
Figure 5.8. *Cumulative dissipated energy vs. roof drift ratio for tested RC frames in the 1th cycles*
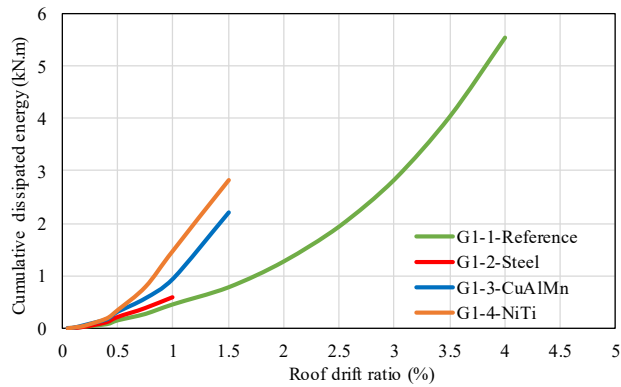
Figure 5.9. *Cumulative dissipated energy vs. roof drift ratio for tested RC frames in the 2nd cycles*

In the following Table 5.3, it is obvious that G1-1-Reference has the lowest dissipated energy value at 1.5 roof drift even if it reaches maximum roof drift ratio at the end of experiment. Neverthless, the amount of dissipated energy of G1-4-NiTi is very close to reference specimen while it attains 2% maximum drift ratio. Also, NiTi-strengthened frame has almost twice as much energy as CuAlMn-strengthened frame at the end of the experiments. Moreover, Figure 5.9 clearly indicates that the dissipated energy by the frames during the second cyclic loading of roof drifts is considerably lower than the the dissipated energy in the first cycle of roof drifts, which is an expected behavior due to the accumulated damage in the first cycle.

Table 5.3. *The amount of energy dissipation of frames in the 1th cycles*

	Total Dissipated Energy at 1.5% drift (kN.m)	Change in Energy Diss. Compared to that of Reference Frame at 1.5% drift	Total Dissipated Energy at maximum drift (kN.m)	Change in Energy Diss. Compared to that of Reference Frame at maximum drift
G1-1-Reference	1.38	1.00	10.97	1.00
G1-2-Steel	3.60	2.60	3.60	0.33
G1-3-CuAlMn	2.72	1.97	4.8	0.44
G1-4-NiTi	5.99	4.33	9.85	0.90

5.5 Ductility

Ductility is described as the ability of material, component or a system to sustain post-elastic deformations without substantial reduction in strength. There are some definitions of ductility in the literature to assess the structural response; material based-ductility, section-based ductility, member-based and globally system-based ductility. In this study, the global deformation capability of a system is dealed with explaining the effect of other ductility factors. To calculate the ductility of a system, an idealized bi-linear curve of forward envelope curves is used. Here, the two approaches used to idealize to actual backbone curve is summarized in Figure 5.10. A point corresponding to a 15% strength reduction after the post-peak strength considered as the ultimate point for backbone curve. There are two methods to represent the envelope curves in a bilinear form; an idealization with one slope using secant stiffness or two slope using post-yield stiffness (FEMA 356 and Akın, 2011, p.146). Here, the most appropriate idealization is made on the capacity curves for representation by equating the area under backbone curve to the idealized curve. Then the ductility is calculated using the relationship between ultimate and yield displacement.
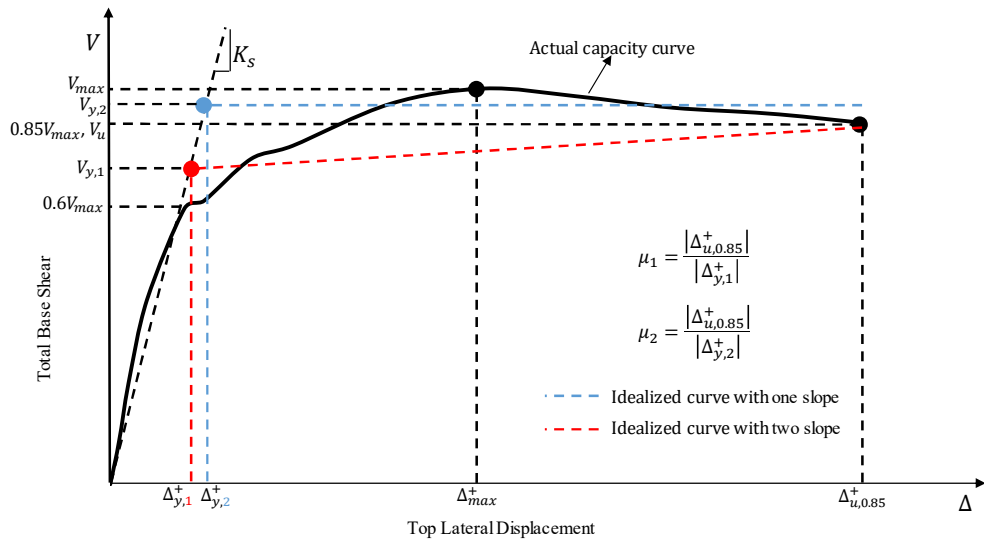
Figure 5.10. *Illustration for the calculation of frame ductility*

An idealization of capacity curves is made using a relation expressed in above figure. Bilinear forms of forward envelope curves are given in Figure 5.11. It is clear from the following figures that the RC frame with or without strengthening mechanism showed a ductile behavior. The ductile response observed from the RC frames is attributed to the low axial load on the columns. Consequently, plastic flexural hinges were developed at the column ends without experiencing shear failure. The capacity curves of first three experiments are idealized using a relation expressed in blue line form in Figure 5.10. In the last experiment, the idealized form of G1-4-NiTi is accounted for considering post-yield slope that corresponds to red line form in Figure 5.10. The reason for considering such a different approach in the G1-4-NiTi is to minimize the difference between the actual and idealized capacity curves.

It is obvious in the following idealization figures that each test has its own characteristic envelope curve with different effective or secant stiffness. This parameter has an influence on the estimation of a ductility. Note that the only difference among all frame tests is the strengthening materials used to enhance the seismic performance of RC frames.

(a) G1-1-Reference

(b) G1-2-Steel

(c) G1-3-CuAlMn

(d) G1-4-NiTi
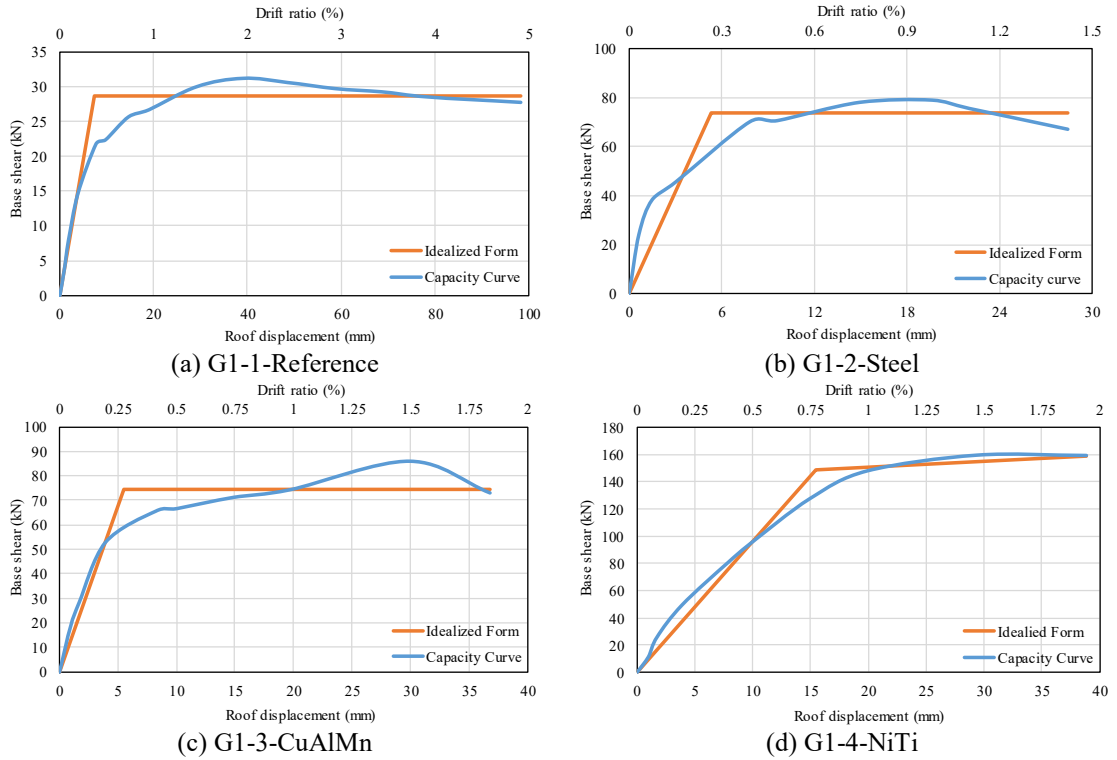
Figure 5.11. *Idealized envelope curves of frames*
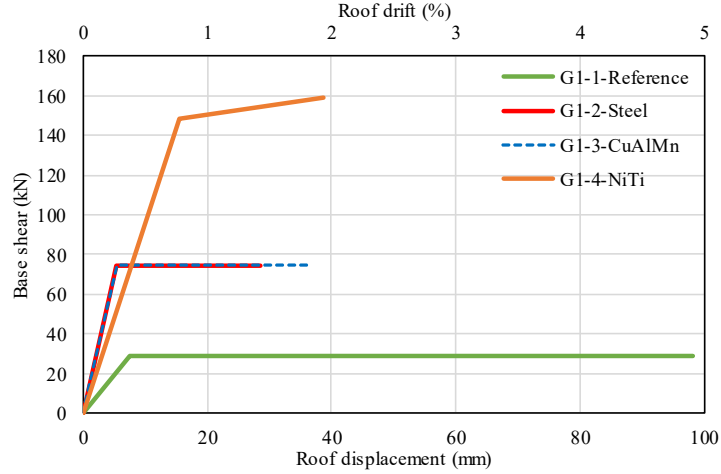
Figure 5.12. *Comparison of idealized curves*

Table 5.4. *Numerical results of ductility calculation*

Specimen	V_y^+	Δ_y^+	$\Delta_{u,0.85}^+$	Ductility $\Delta_{u,0.85}^+/\Delta_y^+$
	(kN)	(mm)	(mm)	(mm/mm)
G1-1-Reference	28.57	7.59	98.19	12.94
G1-2-Steel	73.98	5.31	28.46	5.36
G1-3-CuAlMn	74.58	5.52	36.78	6.67
G1-4-NiTi	148.36	15.43	38.81	2.51

The ductility parameter is computed for each of the test using the bilinear idealization approximation. Therefore, the results are presented in above Table 5.4. There are two important issues affecting the ductile behavior of RC frames, the fracturing of the strengthening rods and rigid connection between the subcomponents of the strengthening system. In the frame hysteresis curves, it is apparently observed that the lateral load suddenly decreases if one of the above-mentioned failure criterion takes place. Moreover, the martensitic behavior of the strengthening bars would seriously affect the ductility unless any failure observed.

As expected, the estimated ductility was highest for the reference frame, which is 12.94, since it sustained maximum lateral drift with lowest base shear. Even if the NiTi tolerated its lateral drift ratio up to 2% drift ratio, which is similar to G1-3-CuAlMn, the calculated ductility is lower than G1-3-CuAlMn. The reason of why such a difference occurred is higher lateral loading and idealization with two-slope. The yield strength and displacement of the G1-2-Steel and G1-3-CuAlMn is very close to each other whereas the G1-4-NiTi has highest yield value.

5.6. Equivalent Viscous Damping

The input energy coming from the harmonic or periodic excitation during the loading process is dissipated in viscous damping. So, the system creates a hysteresis loop in a form of elliptical shape. Then, the area within hysteresis loop gives the energy dissipated by the system. The equivalent viscous damping (ξ_{eq}) can be simply defined as a relation between the dissipated energy (E_D) and elastic strain or stored energy (E_{So}) in an excitation cycle of actual structure. It is of interest to know that the formula of equivalent viscous damping can be derived as equating the energy dissipated in a cycle to the energy dissipated in viscous damping. Also, there is an important assumption in the formula that the excitation frequency is the same as the natural frequency of the system.

$$\xi_{eq} = \frac{1}{4\pi}\frac{E_D}{E_{So}} = \frac{1}{2\pi}\frac{A_{loop}}{F_{max}D_{max}} \tag{5.1}$$

The structures exhibit nonlinear behavior due to the yielding of materials used in the construction under seismic loading. A large portion of the energy is dissipated in the inelastic range of structures throughout the formation of plastic hinges, cracking,

interaction with non-structural elements, soil-structure interaction, etc. The SMA materials can be utilized in passive or active vibration control systems effectively as a damper due to its unique properties such as restoring force (Han et al, 2003). The equivalent viscous damping ratio could be also a key parameter to understand the behavior of structure under the effect of earthquake loading while it displays plastic deformations with residual values and dissipates the energy. Here, the equivalent viscous damping ratio is calculated to further understand the behavior of RC frames under quasi-static cyclic loading. In these estimations, Equation (5.1) and Figure 5.13 are taken into consideration.
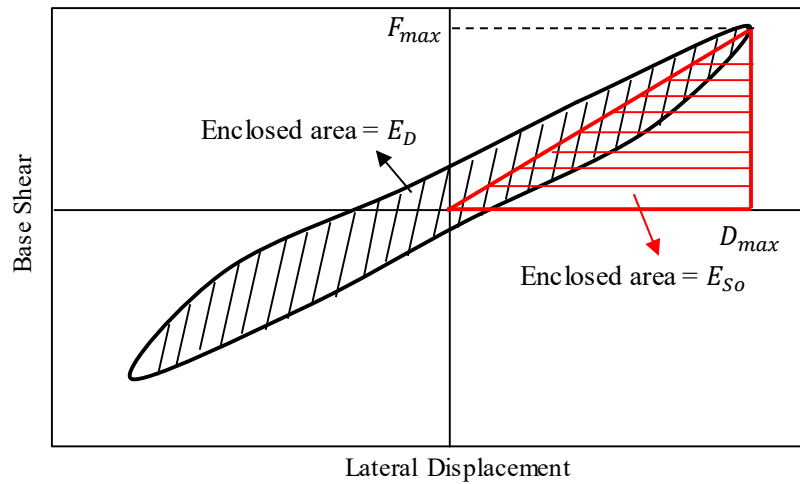
Figure 5.13. *Dissipated and stored energy for viscous damping*

The measured response of the RC frames under lateral loading is different from each other and they show variable damping characteristics depending on the nature of frames. For instance, the first cycles of roof drifts have higher damping capabilities than the second cyclic loading of same drift ratio as it is shown in the following figures. Besides, the first hysteretic damping ratio measured in all frames corresponding to first drift ratio 0.05% is around 5%. At the beginning of tests, there is no exact difference between the specimens. The sudden increase and decrease are observed in the steel-strengthened frame. The reference frame followed less fluctuating way up to 1% drift ratio and more stable way after that drift compared to other frames in Figure 5.14. Contrary, the as-built specimen has smooth and almost linear path after 0.4% in Figure 5.15. The most critical reduction in damping capacity between the first and second cycles

is observed in G1-2-Steel by 70%. It is worh to debate the damping performance of frames strengthened with shape memory alloys since these materials exhibit a recovery after removing the applied load with negligible residual values to a 6% strain. Keep in mind that the strengthening bars were not loaded properly in NiTi SMA-strenghtened experiment because of loosing of functionality of U-shaped plates. Generally, the damping capability of SMA-based strengthened frames are lower than the reference specimen except for 0.2% drift in both first and second drift cycles. It is interesting that the ability to absorb the input energy of CuAlMn and NiTi-based strengthened frames are higher than the reference specimen at 0.2% drift. When it comes to comparing SMAs with G1-2-Steel in the second loading cycles, the frames with NiTi and CuAlMn SMA bars exhibited better damping capacity. It is important for the structure to damp the input energy under reversed cyclic loadings. In these experiments, the damping ratios of G1-3-CuAlMn and G1-4-NiTi are close to each other. Even if the materials have the ability to absorb energy during the cyclic loading due to the imposed damage and inherit nature of materials, the experimental system should give a proper chance the materials to exhibit damping capability. The reason of why NiTi test could not attain sufficient damping ability is the unexpected failure of U-shaped plates.
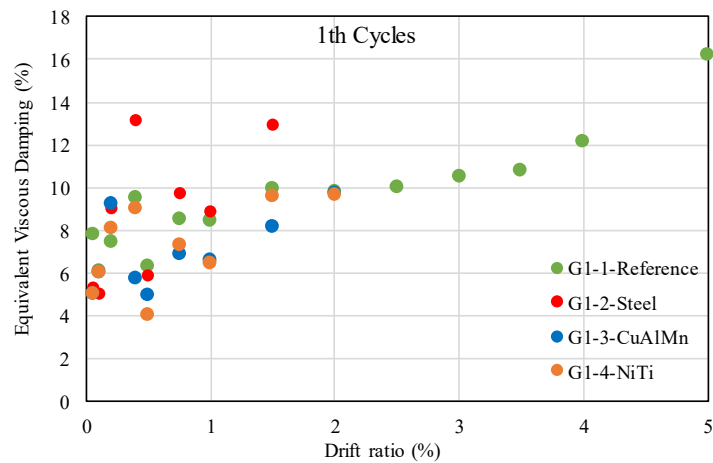
Figure 5.14. *Equivalent viscous damping of specimens for the first cycles*
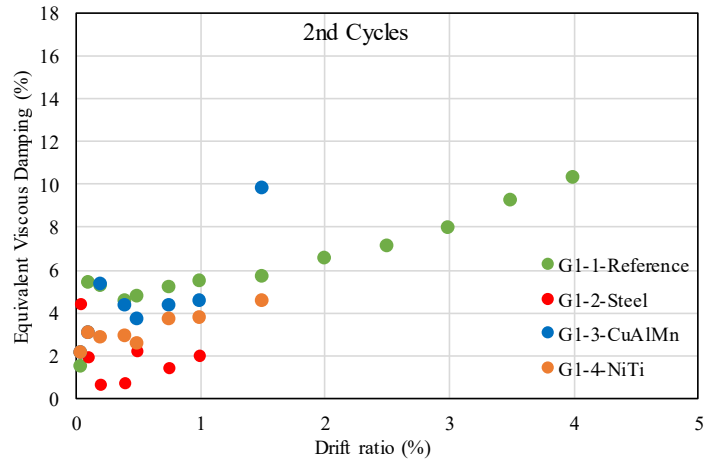
Figure 5.15. *Equivalent viscous damping of specimens for the second cycles*

5.7. Re-centering

We know from the experimental studies that the RC structures experiences residual deformations after seismic loading since the materials used in construction are prone to experience inelastic deformations causing residual deformations even after the load removal. The source of this unrecoverable deformations is the nonlinearity of materials with permanent deformations. On the contrary, shape memory alloy materials have a unique property of eliminating or limiting the residual deformations via shape memory effect or superelasticity. It means that the SMA material exhibit a full recovery from large post-yield strains (generally 6% strain) to the origin of stress-strain curve. There is a comparable performance in terms of residual displacement in the system after the starting of martensite phase even if the SMA materials experiences large strains. This superior effect provides the structure to recover its inelastic deformations and limit it in more acceptable range. To clarify the re-centering mechanism, the main parameter is the residual displacement or drift value that the frame experienced while it comes back after the load is removed.

In this experimental study, two types of residual displacement or drift calculations are introduced considering the observed behavior in the hysteresis curves. The first one is the classical calculations made in literature, which is the intersection point of the unloading path on the horizontal axis. Second and lastly, a different approach is applied to the hysteresis to obtain the residual values. In this method, the hysteretic behavior of frames is considered in the numerical estimates.

5.7.1. First method to calculate residual displacement

The basic idea is presented here to calculate the residual displacement values of frames after each roof drift is applied. In each cyclic process, the hysteretic curve has loading and unloading path. The residual displacement value of a hysteresis is accepted a point where the hysteretic curve intersects the horizontal axis, which is the roof displacement axis, due to nonlinear behavior of materials while the applied load is removed. Note that shape of hysteresis is neglected in this type of computing since the focus is the intersection points of unloading path and horizontal axis of hysteresis. Similar way for flag-shaped hysteresis is adopted in a study performed by Cardone (2012).

In Figure 5.17, the hysteretic curves of tested RC frames are given by dividing them into four parts, which are the hysteresis loops up to 0.5% roof drift and its focused views and hysteresis loops after 0.5% up to end of tests and again its focused views. The aim of presenting focused views of hysteretic curves is to be able to inspect the change in loading or unloading path and the intersection point in the horizontal axis of hysteresis. The way to determine the intersection point on the horizontal axis is shown in Figure 5.16. Moreover, the detailed hysteretic curves of the tested RC frames are shown Figure 5.19. Note that G1-1-Reference was subjected to serious damage level after %2 lateral drift ratio and the shape of hysteretic loops is like the G1-3-CuAlMn until that drift ratio.
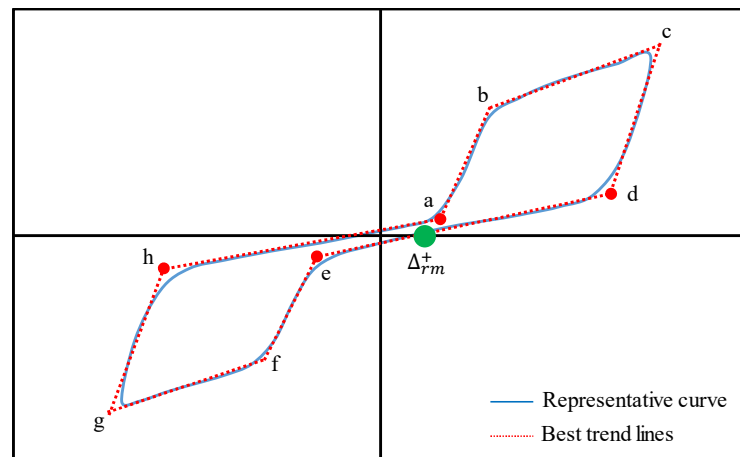
Figure 5.16. *Calculation of residual displacement using first method*

106
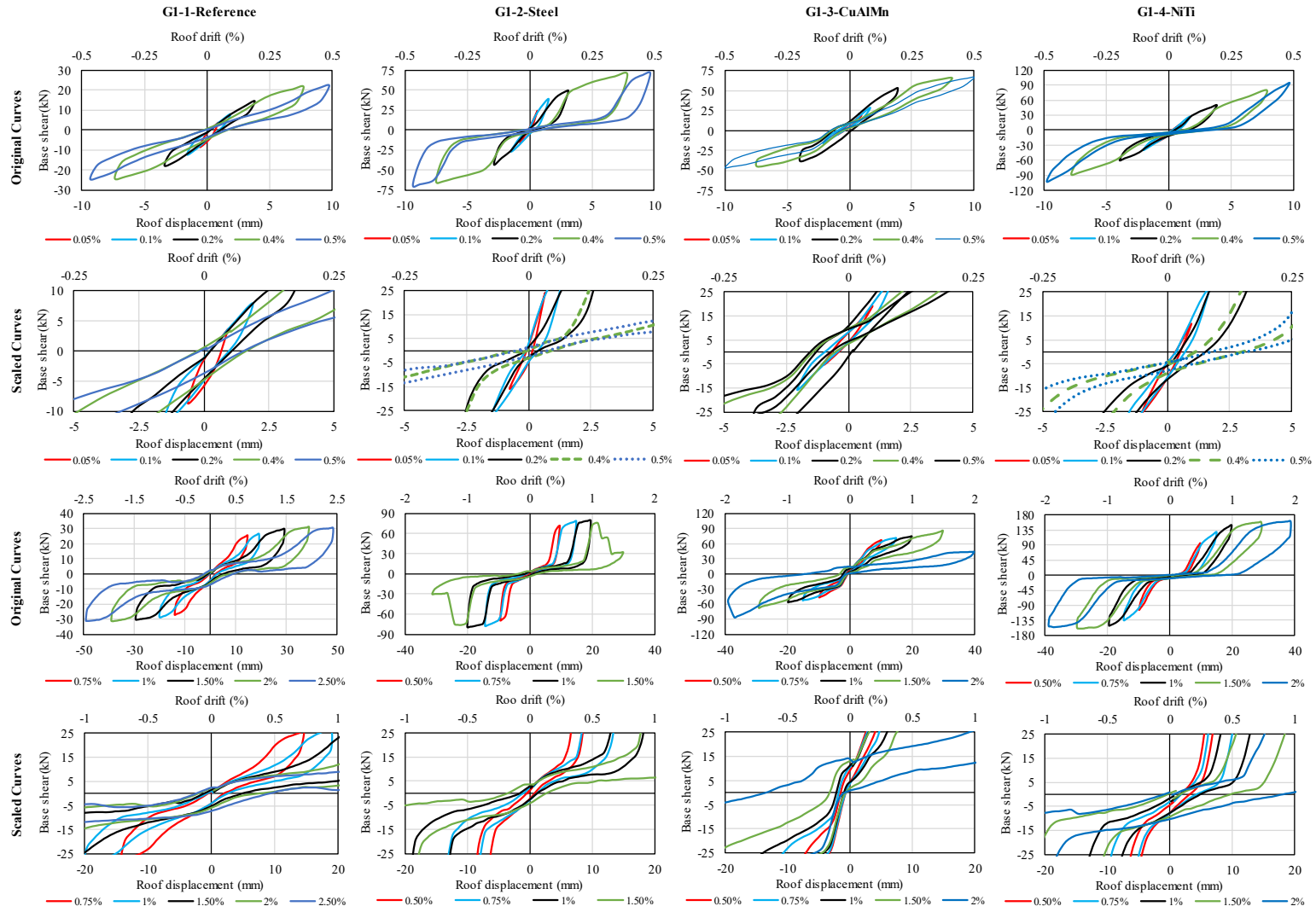
Figure 5.17. *Comparison of hsyteretic curves in re-centering property*
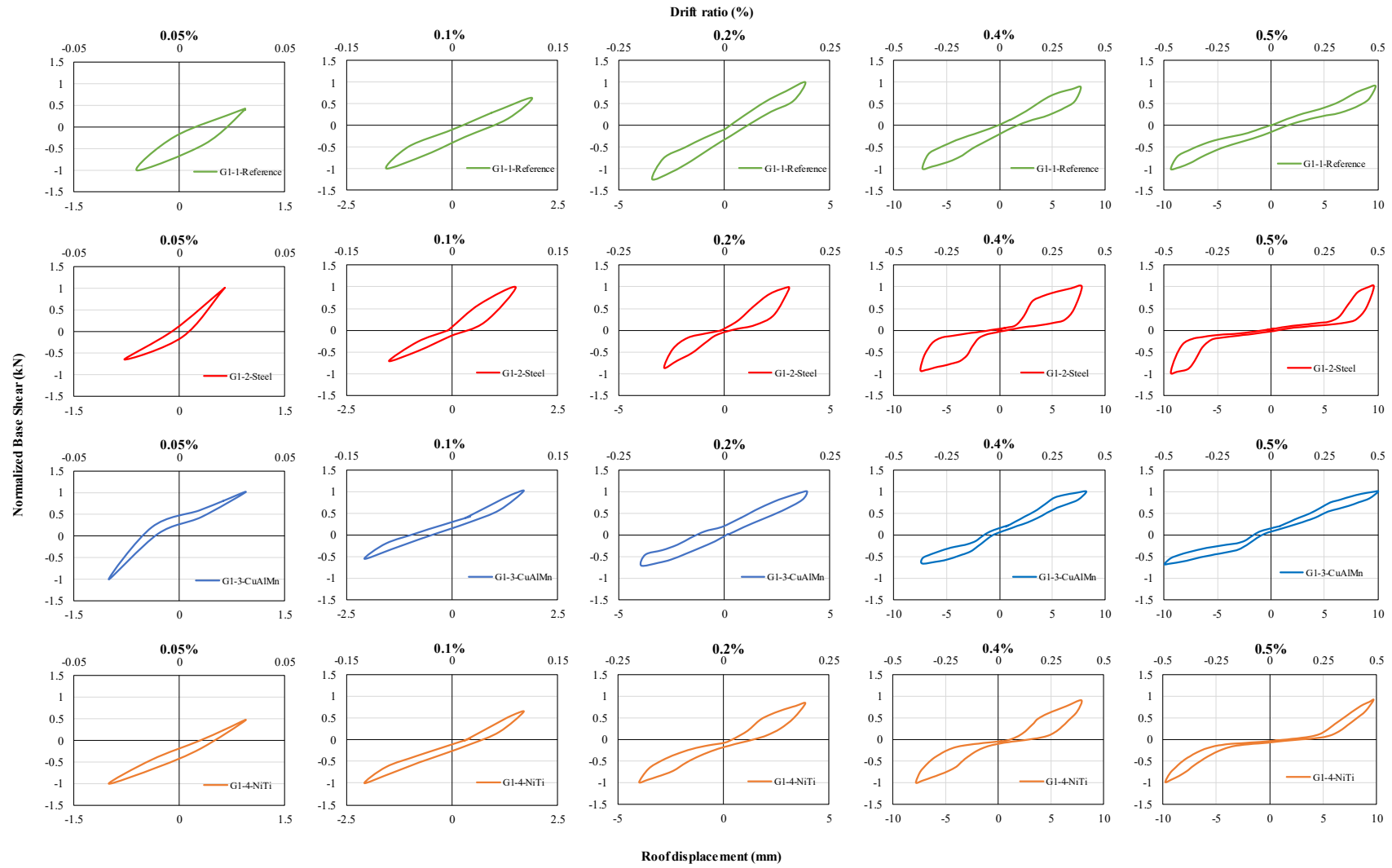
Figure 5.18. *Comparison of experimental hysteretic behaviors of specimens*
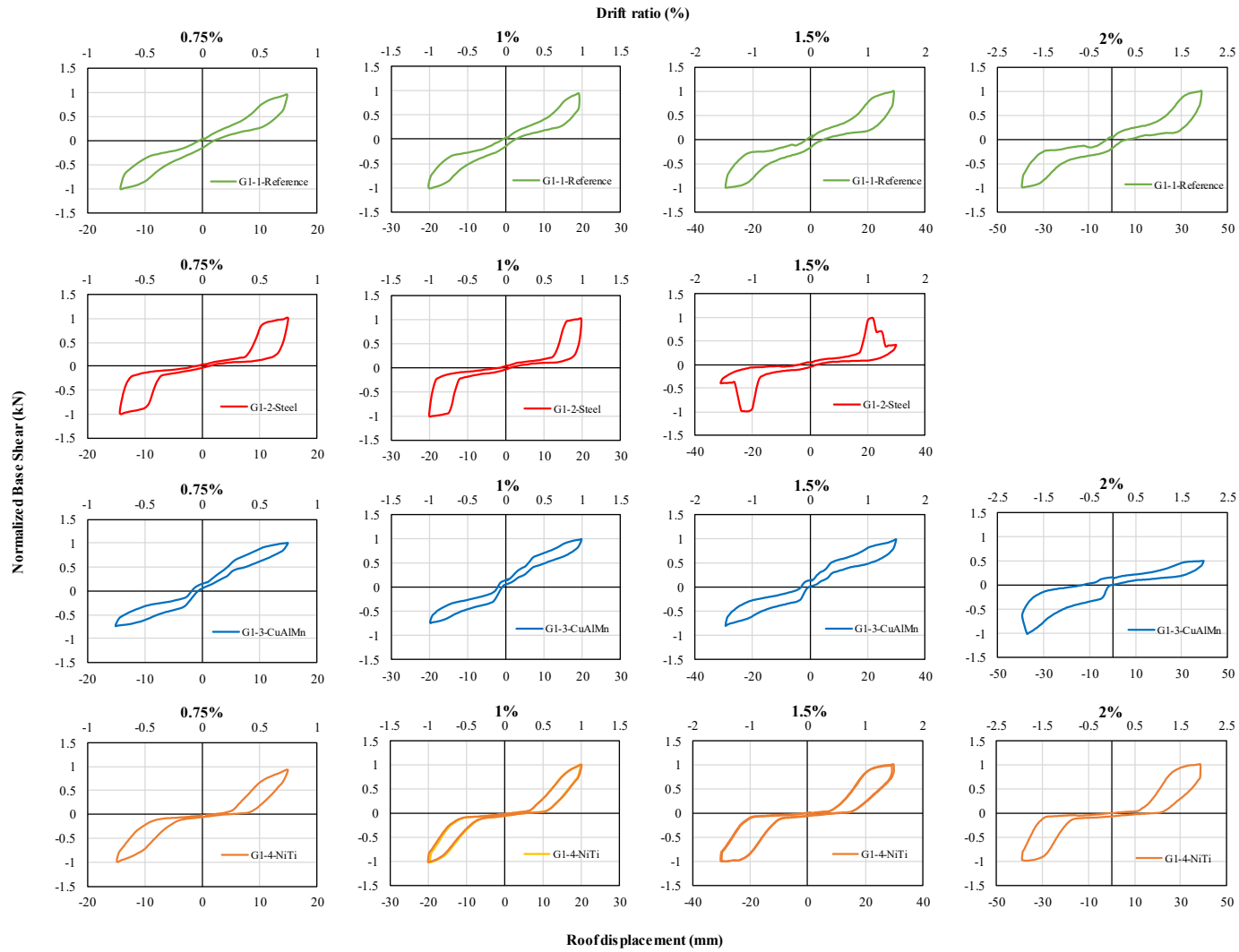
Figure 5.19. *Comparison of experimental hysteretic behaviors of specimens (Continue)*
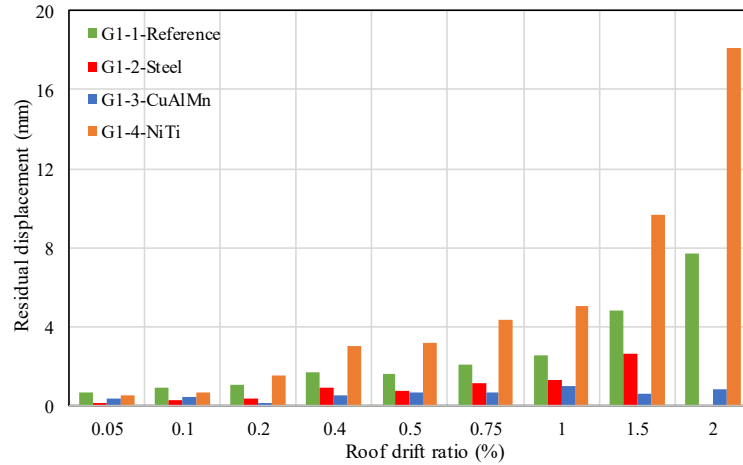
Figure 5.20. *Residual displacement vs. roof drift ratio of the RC frames*

As can be seen in Figure 5.20, G1-3-CuAlMn has considerably lower residual values compared to other RC frames due to re-centering property of SE CuAlMn bars. However, the G1-4-NiTi could not show similar fully re-centering mechanism due to failure of U-shaped plates. At 1.5% lateral drift ratio, the residual displacement of G1-2-Steel has lower than the G1-1-Reference. It means that actively-worked strengthening mechanism provided self-centering in the hysteretic curve.

5.7.2. Second method to calculate residual displacement

The structural response of tested RC frames, which is the hysteresis loops, is further taken into consideration under applied cyclic loading compared to first method. For example, the initial shape of hysteresis at the beginning and the change in the shape of hysteresis while the frame tries to come back to zero position with the effect of recovery force are interpreted entirely. In this calculation, a similar way, which were used in a study presented by Speicher et al., 2011, is adopted to compute the residual displacement upon unloading in both forward and backward direction. As illustrated in Figure 5.18 and Figure 5.19, the hysteretic responses of specimens differ from each other. Such a variation in response results from the damage level of frames during the loading scheme and material characterization used in system to strengthen RC frames. Finally, how calculations are made for the residual displacements in pushing and pulling directions in loading and unloading paths, $\Delta_{RL,RU}^{+,-}$, is shown in Figure 5.21. Keep in mind that this figure is only a schematic representation for the calculations. A critical stiffness change is accepted as minimum %20 to identify the displacements at the point of a, d, e and h.
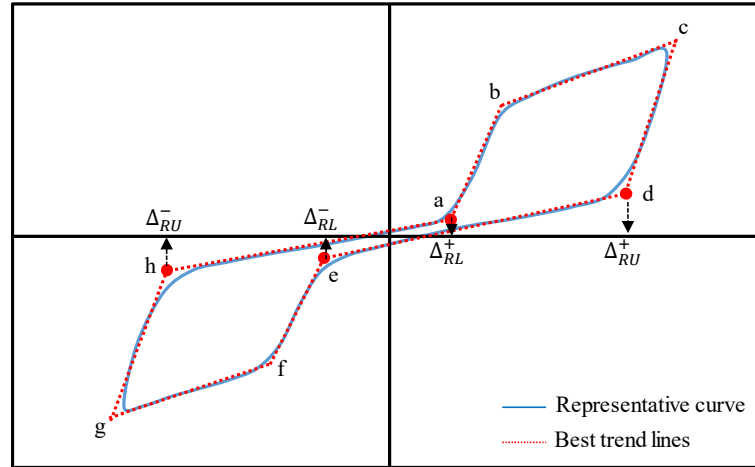
Figure 5.21. *Calculation of residual displacement using second method*

The numerical results estimated in each hysteresis is given in Table 5.5. Here, the N/A represents "Not Applicable" due to a boundary condition. If this term is used in the table, this means that the specimen has no "critical stiffness change" at this drift ratio depending on the type of path. Additionally, the calculations are not made for the G1-3-CuAlMn since it showed superelasticity and successful re-centering ability upon unloading contrary to other frames.

Table 5.5. *Residual displacement values of specimens using second method*

		Roof drift ratio (%)						
		0.2	0.4	0.5	0.75	1	1.5	2
G1-1-Reference	Δ_{RL}^+ (mm)	N/A	N/A	N/A	N/A	10.59	14.80	20.54
	Δ_{RU}^+ (mm)	3.28	6.96	7.60	13.99	14.97	22.59	30.34
	Δ_{RL}^+ (mm)	N/A	N/A	N/A	N/A	-10.18	-14.45	-20.73
	Δ_{RU}^+ (mm)	-2.90	-6.69	-8.34	14.25	-15.11	-23.08	-32.05
G1-2-Steel	Δ_{RL}^+ (mm)	N/A	1.62	6.10	7.94	12.59	17.44	
	Δ_{RU}^+ (mm)	2.16	6.24	7.79	13.20	18.15	27.31	
	Δ_{RL}^+ (mm)	N/A	-1.82	-5.97	-7.65	-12.26	-17.60	
	Δ_{RU}^+ (mm)	-2.25	-6.22	-7.98	-12.35	-18.18	-27.78	
G1-4-NiTi	Δ_{RL}^+ (mm)	1.93	2.05	4.60	5.24	6.85	9.56	13.13
	Δ_{RU}^+ (mm)	2.53	5.00	5.79	8.81	11.65	16.12	23.27
	Δ_{RL}^+ (mm)	-2.66	-1.80	-3.89	-4.46	-7.53	-10.31	-17.83
	Δ_{RU}^+ (mm)	-3.47	-4.93	-5.90	-9.37	-13.19	-21.21	-30.72

To make further clarification, the numerical results given in above table are demonstrated graphically in the following figures. It is of importance to evaluate this graphs that if the specimens do not experience a critical stiffness change (especially it has occurred in the first cycles of G1-1-Reference) the residual value is equal to the unloading residual displacement value. Generally, G1-4-NiTi has lowest residual values compared to other tests. It can be interpreted that even if the G1-4-NiTi do not exhibit fully re-centering property observed in G1-3-CuAlMn due to insufficient functionality of U-shaped plates, the findings verify the semi re-centering mechanism of G1-4-NiTi. Also, the NiTi bars showed superelasticity according to the load cell and strain gage data presented in Chapter 4.5.
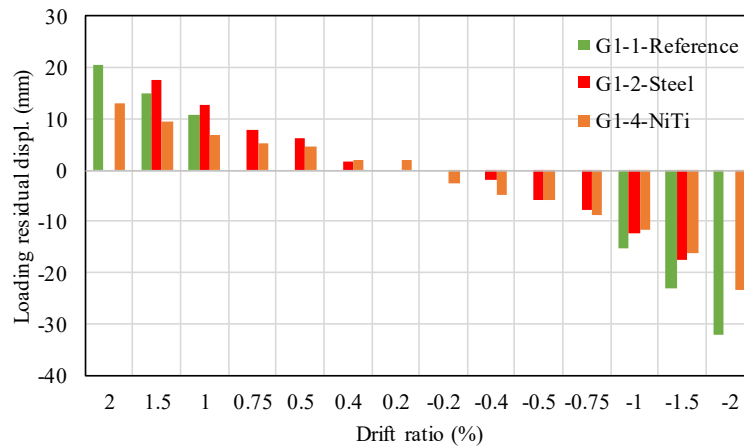
Figure 5.22. *Loading residual displacement (Δ_{RL}) vs. drift ratio relationship of specimens*
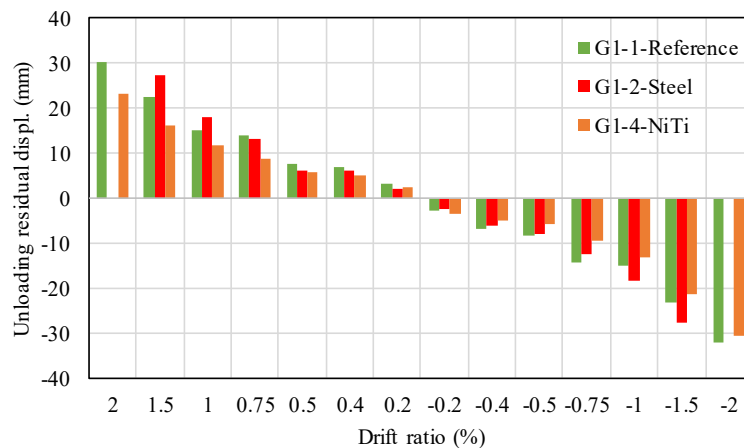
Figure 5.23. *Unloading residual displacement (Δ_{RU}) vs. drift ratio relationship of specimens*

It is interesting to find that the G1-1-Reference frame has less loading and unloading residual displacement value compared to that of G1-2-Steel at 1% and 1.5%

drift ratio. It is most probably due to the fact that the as-built specimen did not have the same damage level observed in the second experiment at this roof drift level. The similar loading and unloading paths to the G1-2-Steel are noticed in the reference frame hysteresis after 2% drift ratio. The sudden increase in slope of loading part after stabilized path starting from origin means that the frame starts to resist against the lateral loading. Otherwise, the sudden decrease in the slope of unloading path means that the resistance of RC frame against lateral loading softens due to cumulative damage level occurred in previous drifts. G1-2-Steel has lower residual values up to 1% roof drift since the critical damage level is observed in steel-strengthened frame after 1% drift. It means that the strengthening procedure with any material is successfull in limiting the residual displacement values until the frame reaches unrecoverable damages.

5.8. Strain Gages Data

The strain gages were placed on the longitudinal and lateral reinforcements of structural members before concrete casting to collect strain data while the frame is subjected to quasi-static cyclic loading. It is important to know that the the placement of strain gages to the bars is composed of several steps. Moreover, the concrete casting can negatively affect the strain gages unless they are protected well. Also, if the length of strain gage cables was not enough to connect it to the data logger, the length of cables was elongated by making an addendum. Furthermore, the location of strain gages on the bars might not match up to a region where the maximum strain can occur. Finally, the reliability of data is dependent on all conditions mentioned above. The first yield strain and maximum strain obtained from strain gages for each type of bars in the system are summarized in the following tables (Table 5.6-Table 5.9). In these tables, Lapp. symbolizes the lapping reinforcements while the Long. represents longitudinal reinforcements. The yielding point of SMA bars are found out using the cyclic tensile test given in Table 3.5. The yield strain of re-bars was calculated from the material tests presented in Figure 3.8 and Figure 3.9.

Generally, the drift values corresponding to first of reinforcement yielding in the reference specimen are higher than the strengthened frames. Yielding of stirrups in the columns are only observed in the reference specimen. A maximum strain of longitudinal reinforcement was measured in the second experiment as 0.473%. The maximum strains

measured in third and last experiments in longitudinal and lapping reinforcements are relatively lower than previous experiments. Besides, the reinforcements of RC frames reached their yielding points in earlier roof drifts in CuAlMn-strengthened frame compared to that of NiTi test. Also, a careful attention must be paid to understand the strains of strengthening bars. In the second experiment, the data are not meaningful since the mid-portion of conventional steel bars showed elastic behavior whereas the ends of bars displayed inelastic behavior. A maximum strain measured in CuAlMn SMA bar was 4.279% at 44th cycle while the strengthened RC frame carried 66.3 kN base shear. On the other hand, the NiTi bars in the positive and negative loading direction reached their ultimate strains at different drift cycles. Moreover, the attained ultimate strains by NiTi bars showed difference from each other.

Table 5.6. *Processed SG data of G1-1-Reference*

Notation	Position	Reinforcement Type	Cycle No.	First Yield Strain, ε_y (mm/mm)	Roof Displ. (mm)	Base Shear (kN)	Drift Ratio (%)	Cycle No.	Maximum Strain, ε_{max} (mm/mm)	Roof Displ. (mm)	Base Shear (kN)	Drift Ratio (%)
SG-7	C2 - BS	Stirrup	45	0.00118	27.63	24.15	1.40	55	0.00223	57.66	29.7	2.93
SG-17	C2 - BR	Long. re-bar	55	0.00111	53.67	29.25	2.72	67	0.00149	98.19	27.75	4.98
SG-19	C2 - TL	Long. re-bar	44	0.00115	-25.71	-29.4	-1.31	64	0.00434	-74.37	-29.25	-3.78
SG-21	C2 - TR	Long. re-bar	43	0.00113	23.22	27.15	1.18	55	0.00256	58.68	29.7	2.98
SG-7	C1 - TR	Long. re-bar	43	0.00112	24.24	27.75	1.23	55	0.00223	57.66	29.7	2.93
SG-9	C1 - TL	Long. re-bar	44	0.00113	-26.73	-29.7	-1.36	64	0.00268	-74.37	-29.25	-3.78
SG-1	C1 - BS	Stirrup	31	0.00112	11.94	23.4	0.61	37	0.00137	18.03	26.1	0.92
SG-5	C1 - BR	Lapp. re-bar	63	0.00110	75.87	28.2	3.85	67	0.00135	96.72	27.75	4.91
SG-6	C1 - BR	Long. re-bar	32	0.00115	-13.56	-27	-0.69	32	0.00116	-14.22	-27.3	-0.72

Table 5.7. *Processed SG data of G1-2-Steel*

Notation	Position	Reinforcement Type	Cycle No.	First Yield Strain, ε_y (mm/mm)	Roof Displ. (mm)	Base Shear (kN)	Drift Ratio (%)	Cycle No.	Maximum Strain, ε_{max} (mm/mm)	Roof Displ. (mm)	Base Shear (kN)	Drift Ratio (%)
SG-15	C1 - BR	Long. re-bar	31	0.00116	14.1	76.8	0.72	43	0.00473	30.01	31.95	0.16
SG-14	C1 - BR	Lapp. re-bar	37	0.00121	14.78	60.6	0.75	43	0.00180	30.01	31.95	0.16
SG-21	C1 - TL	Long. re-bar	19	0.00114	6.825	67.35	0.35	43	0.00175	29.20	30.8	0.15
SG-19	C1 - TR	Long. re-bar	38	0.00111	-16.85	-76.65	-0.86	44	0.002	-28.19	-30	-0.15
SG-3	C2 - BR	Lapp. re-bar	25	0.00111	9.03	69	0.46	43	0.00176	29.20	30.8	0.15
SG-5	C2 - BL	Lapp. re-bar	26	0.00112	-8.805	-67.95	-0.45	38	0.00154	-15.9	-75.6	-0.08

Table 5.8. *Processed SG data of G1-3-CuAlMn*

Notation	Position	Reinforcement Type	Cycle No.	First Yield Strain, ε_y (mm/mm)	Roof Displ. (mm)	Base Shear (kN)	Drift Ratio (%)	Cycle No.	Maximum Strain, ε_{max} (mm/mm)	Roof Displ. (mm)	Base Shear (kN)	Drift Ratio (%)
SG-17	C2-BR	Lapp. re-bar	32	0.00117	-11.37	-46.80	-0.58	48	0.00190	-36.29	-84.15	-0.19
SG-21	C2-TR	Long. re-bar	25	0.00114	8.46	62.85	0.43	47	0.00161	39.27	43.50	0.21
SG-19	C2-TL	Long. re-bar	48	0.00114	-32.64	-74.55	-1.66	48	0.00161	-39.20	-85.80	-0.21
SG-7	C1-TR	Long. re-bar	25	0.00111	6.53	54.15	0.33	42	0.00291	16.02	51.45	0.08
SGS-2	CuAlMn-2	Strengthening bar	32	0.00703	-13.26	-49.95	-0.67	44	0.04279	-28.61	-66.30	-0.15

Table 5.9. *Processed SG data of G1-4-NiTi*

Notation	Position	Reinforcement Type	Cycle No.	First Yield Strain, ε_y (mm/mm)	Roof Displ. (mm)	Base Shear (kN)	Drift Ratio (%)	Cycle No.	Maximum Strain, ε_{max} (mm/mm)	Roof Displ. (mm)	Base Shear (kN)	Drift Ratio (%)
SG-14	C1-BL	Lapp. re-bar	26	0.00112	-9.80	103.05	-0.50	48	0.00145	-35.42	-154.20	-0.19
SG-16	C1-BR	Lapp. re-bar	31	0.00110	12.71	113.40	0.64	43	0.00149	28.43	158.40	0.15
SG-7	C2-TL	Long. re-bar	37	0.00113	18.96	144.00	0.96	47	0.00185	38.81	158.85	0.20
SG-21	C1-TL	Long. re-bar	31	0.00120	10.83	99.90	0.55	47	0.00207	31.79	152.55	0.17
SG-9	C2-TR	Long. re-bar	32	0.00113	-13.05	125.70	-0.66	48	0.00183	-37.34	-155.55	-1.90
SG-19	C1-TR	Long. re-bar	44	0.00115	-21.15	144.15	-1.07	48	0.00162	-34.50	-153.00	-1.75
SG-5	C2-BR	Lapp. re-bar	37	0.00114	17.01	132.75	0.86	43	0.00163	26.43	156.60	1.34
SG-3	C2-BL	Lapp. re-bar	32	0.00114	-11.37	113.25	-0.58	44	0.00169	-26.03	-156.30	-1.32
SGS-1	NiTi-1	Strengthening bar	32	0.00588	-14.78	135.30	-0.75	44	0.01276	-28.98	-158.85	-0.15
SGS-2	NiTi-2	Strengthening bar	32	0.00596	-10.56	105.75	-0.54	44	0.01543	-27.98	-159.15	-0.15
SGS-3	NiTi-3	Strengthening bar	31	0.00587	10.83	99.90	0.55	47	0.04602	38.81	158.85	0.20
SGS-4	NiTi-4	Strengthening bar	31	0.00641	10.83	99.90	0.55	47	0.03835	38.81	158.85	0.20

5.9 Ambient Vibration Results

Ambient vibration measurements were carried out through four accelerometers placed on the two upper ends of RC frame to interpret the structural performance in different aspects. The accelerometers provided an information about the change in frequency before and after the tests. So, this change can be interpreted considering the loss of stiffness due to the damage occurred during the reversed cyclic loading conditions. It should be noted that there is a difference between the reference specimen and the rest of specimens, which were strengthenened. All measurements were conducted without additional mass on the frame, and there was no connection between the actuator and the frame and out-of-plane supports. The specimens were only connected to a strong floor by the help of bolts during the measurements. Then, ambient vibration measurements were performed for 30 minutes for each of specimens. A sampling rate of vibration measurements were 200 Hz. during the tests.

The ambient vibration test results acquired from overall experimental process are summarized in Figure 5.24. To simplify the illustration, the horizontal axes of these graphs are logarithmically scaled. The frequency value obtained from all accelerometers placed on the beam and slab level are very close to each other. Apparently, the frequency of tested RC frames after experiments are lower than initial frequency. It means that the RC frames lost their original stiffnesses partially as the damage occurs due to increasing amplitude of lateral drifts. This results in elongation in the period of structure and hence a reduction in the frequency. What we know from the structural dynamics is that there is an inversely proportional relation between the frequency and the period. Multiplication of these two parameters is equal to 1 and one of these parameters raises as another one decreases or vice versa.
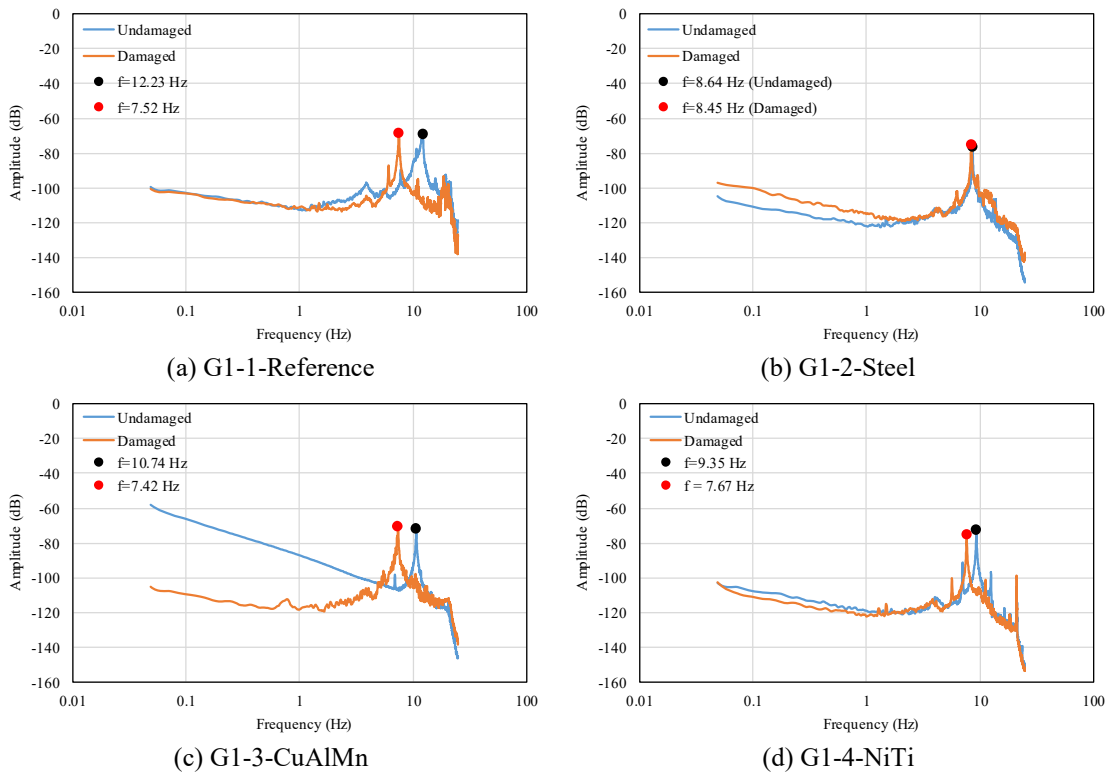
Figure 5.24. *Frequency change in specimens*

Vibration-based test results are also presented in Table 5.10 to make comparison among the frames. According to the numerical values given in Table 5.10, the greatest change in frequency took placed in G1-1-Reference by 38%. Although G1-3-CuAlMn tolerated its maximum drift ratio up to 2%, the frequency values reduced by 30.91%. Similarly, the frequency changing ratio in G1-4-NiTi is almost 18%. In the last row of the table, the comparison is made by taking the damaged frequency of first experiment as reference. The damaged frequencies of the tested specimens are close to each other, but it is important to remember that the reference specimen reached its damaged frequency after 5% lateral drift ratio. Although the RC frames are the same in terms of geometric dimensions and material type, the initial frequency values are different from each other. The difference in undamaged frequencies of the specimens might be resulted from the strengthening procedure including drilling works that can be lead to the damage in the beam before the test or non-homogenous distribution of concrete material.

Table 5.10. *Numerical results of ambient vibration tests*

		G1-1-Reference	G1-2-Steel	G1-3-CuAlMn	G1-4-NiTi
Undamaged Fre.	(Hz)	12.23	8.64	10.74	9.35
Damaged Fre.	(Hz)	7.52	8.45	7.42	7.67
The changing ratio	(%)	38.51	2.20	30.91	17.97
The change in fre. Compared to that of Ref. Frame	(%)	1	1.12	0.99	1.02

6. ANALYTICAL MODELLING OF FRAMES

The substandard RC frames tested in this study was modeled and analyzed in SeismoStruct Version 7.0.6. to be able to make validation and comparison with the real tests. The SeismoStruct program is capable of predicting the seismic response of structures under various loadings considering the geometric nonlinearities and material inelasticity. In addition, it offers user a chance to create fibre-based beam-column element modelling. Firstly, the original RC frame was taken into consideration and then the strengthening methodology was employed in modelling.

Initially, the mechanical properties of material were taken from the material tests. Accordingly, the average concrete compressive strength and the yield strength of plain re-bars were employed as 16.3 MPa and 332.5 MPa, respectively. Also, strain limits such as yielding and ultimate strain were determined according to the material tests for concrete and steel properties. In SeismoStruct, there are various material alternatives that can be used in analysis. It is a critical issue to select the most appropriate material model since it affects the response of RC frame. For this reason, uniaxial Menegetto and Pinto (1973) steel model and uniaxial nonlinear Mander et al. (1988) concrete model was utilized in analytical modelling of RC frames (Figure 6.1). The proposed steel model, initially developed with ribbed reinforcement bars, can also be used for the modelling of smooth rebars used in the construction of existing RC structures (Prota et al., 2009). As shown in Figure 6.2, the beam and column sections were formed considering the geometric dimensions and reinforcement arrangement given in Section 3. In addition, a 3D model of the bare frame is given in Figure 6.3.

(a) Mander concrete model   (b) Menegetto-Pinto steel model
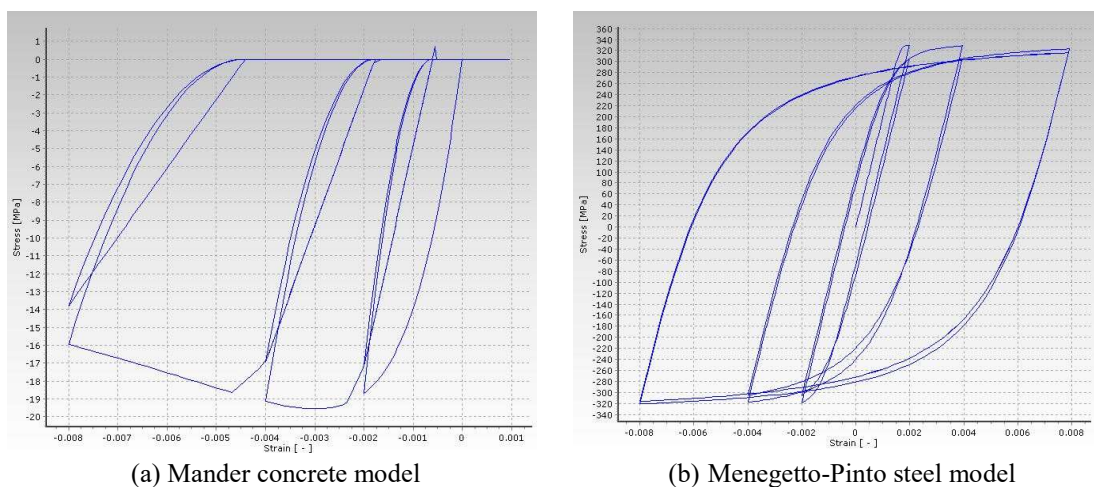
Figure 6.1. *The material models in SeismoStruct*

(a) T-shaped beam section   (b) Column sections
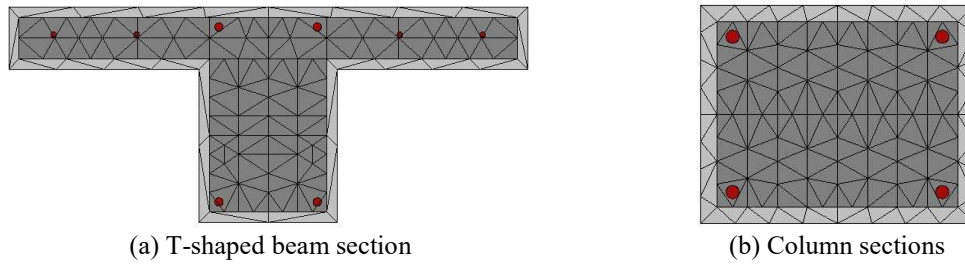
Figure 6.2. *Section views in SeismoStruct*
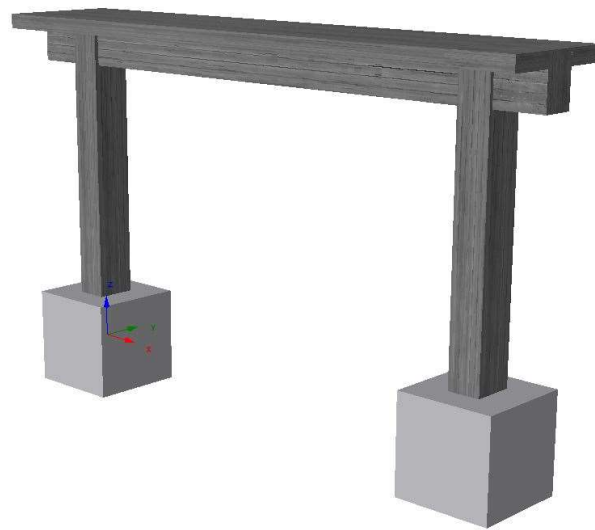
Figure 6.3. *3D view of the reference specimen*

In the first place, the eigen value analysis was conducted to validate the frequency response of reference frame obtained through ambient vibration tests. According to the eigen value analysis, the first mode is fully translational mode in the real loading direction. Therefore, the frequency of original frame in the first translational mode is calculated as 12.52 Hz in SeismoStruct platform. This value is very close to the value obtained from ambient vibration tests for the undamaged condition of G1-1-Reference, which was 12.23 Hz. The small diffence between the ambient vibration measurements and eigen analysis can result from the environmental conditions, the uncertainty in material strength and the reliability of the vibration tests. Such a difference can be interpreted as model-calibration problem in identifying the modal parameters of sample frame by conducting nonlinear analysis. It is known in this study that the under-designed RC frames tested had no infill, which has also driving role in determining the first mode frequency and mode shapes. It should be also kept in mind that the aim of ambient

121

vibration tests carried out in this study is to comment the change in stiffness depending on variation in frequency and make comparison between the undamaged and damaged conditions of frames.

In creating the 3D fibre-based modelling, the inelastic force-based frame element type was selected to form the column and beam members because it is the most accurate element types capabling of capturing the inelastic behavior along the entire length of a structural member according to SeismoStruct manual. In addition, the program provides user an advantage to select individual fibre to obtain the stress-strain state of the related fibre depending on the nature of material. Thus, the individual fibre sections for concrete and steel materials were selected to monitor the variation in stress-strain state at the critical integration sections where the maximum bending moment was expected. Afterward, the loading protocol used in the real tests were applied to the column top ends in the loading direction and static time-history analysis was completed. When it comes to create a model with upgrading mechanism, an extra node was assigned at the beam level. The upgrading material was introduced between the column top node and this extra node. So, the distance between these two nodes is equal to the effective length of the strengthening rods. To be able to reflect the real experimental conditions, the out-of-plane movement of frames was prevented by assigning restraints to the nodes at the beam level. Additionally, it is important to mention that the strengthening rods were introduced to the analytical system as a truss member. A front view of the frame with loading conditions and strengthening bar is illustrated in Figure 6.4. Here, the important point about the working principle of truss member is that the material hysteresis is symmetrical for the forward and backward loading directions in the program (Figure 6.5). Accordingly, there is no need to be assigned another node to the left of the frame with secondary truss member. In real experimental setup, there are two bars working in both pushing and pulling directions. But, in the analytical model, the diameter of the strengthening bar is equal to twice the diameter of the bar in the real test. In conclusion, this model is well compatible with the real experimental setup due to the strengthening material symmetry in hysteresis and double sectional area.
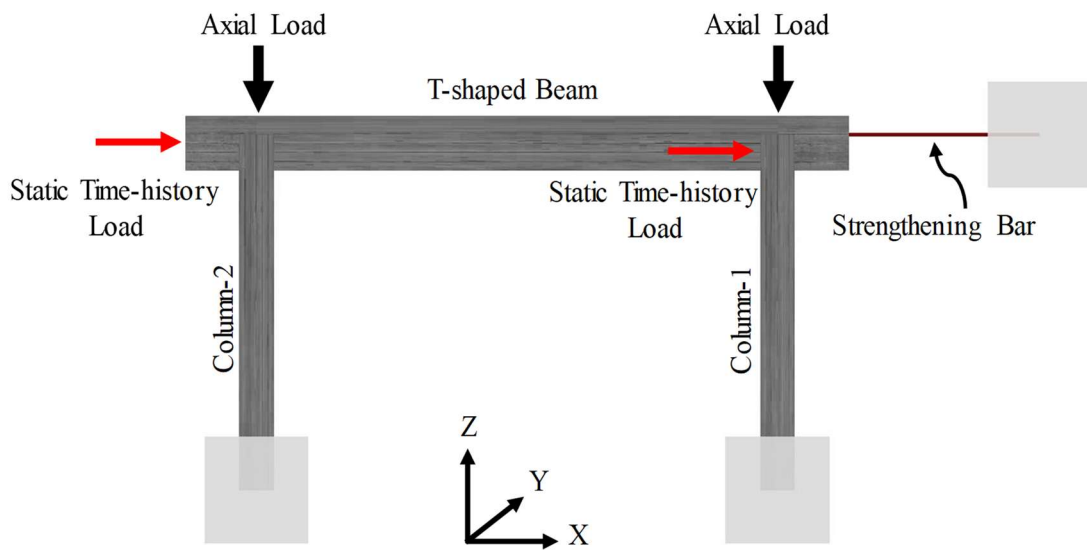
Figure 6.4. *Side view of the analytical model with loading conditions*
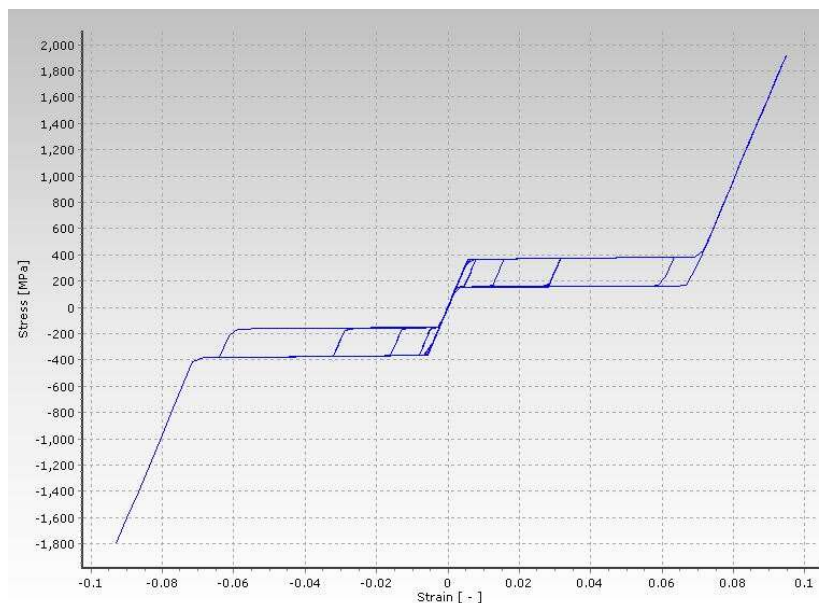
Figure 6.5. *A sample shape memory alloy material model in SeismoStruct*

The results of the analysis are presented in the following sections in terms of hysteresis, envelope curves and critical failure strains marked on the hysteresis. Generally, the performed analysis is well matched up with the experimental results for the first two experiments. It is obvious from the analytical models that the frames tend to exhibit ductile behavior (especially in G1-1-Reference). Firstly, the reinforcement bars yielded and then the unconfined concrete reached to its limiting strain. Such a visible

behavior verifies the design procedure and observed response of RC frames during the experiments. However, the seismic response of RC frames with strengthening methodology under cyclic lateral displacements is directly dependent on the properties of upgrading materials under axial loading. Particularly, the SeismoStruct program assumes constant modulus of elasticity for both fully austenitic and martensitic behavior in SMA material model. In real experiments, the SMA material fractures when they reach axial load or strain capacity. In addition, the analytical model works perfectly under given loading conditions and modelling assumptions. Contrary, our experiments experienced some unexpected problems related to connection between the beam and upgrading materials. For these reasons, the results of analytical models with SMA-upgraded frames are presented up to limit drift ratio, which the frames tolerated in the tests.

It is all clear from the following figures that four RC frames showed ductile behavior in the analysis as it is expected. Also, the total shear force carried by two columns in loading direction under consideration is noticeably lower than their calculated shear capacity. This also validates the flexural seismic response of RC frames during the reversed-cyclic loading.

Firstly, the hysteretic curve of reference specimen is given in Figure 6.6(a). Clearly, the general form of the curve is very close to experimental hysteresis curve in terms of ultimate load and variation in strain. The ultimate load of the non-strengthened specimen is obtained as 31 kN and 30.8 kN for positive and negative loading directions, respectively. Similarly, the ultimate load of the frame was 31.2 kN in the experiment. The shape of hysteresis is not similar in terms of residual displacement. In Figure 4.1, it is obvious that the lateral load sharply reduced to a specific point after the frame reached its peak load in both directions and then the slope of the lateral load seriously changed. Then, it increased gradually up to a specific point and again started to decrease immediately. Such a behavior is mostly due to cumulative damage level related to plastic deformations. In addition, it may be arised from the resisting force activated at certain displaced position from the roller supports on the steel frame around the tested specimen to prevent out-of-plane movement of the RC frame under the combined effect of lateral and vertical load. Thus, the residual strength was not introduced for concrete and steel material in the analytical model even if they are exposed to serious damage level. This is valid for other RC frame modellings in SeismoStruct.

(a) Analytical hysteresis of G1-1-Reference   (b) Comparison of hysteretic loops
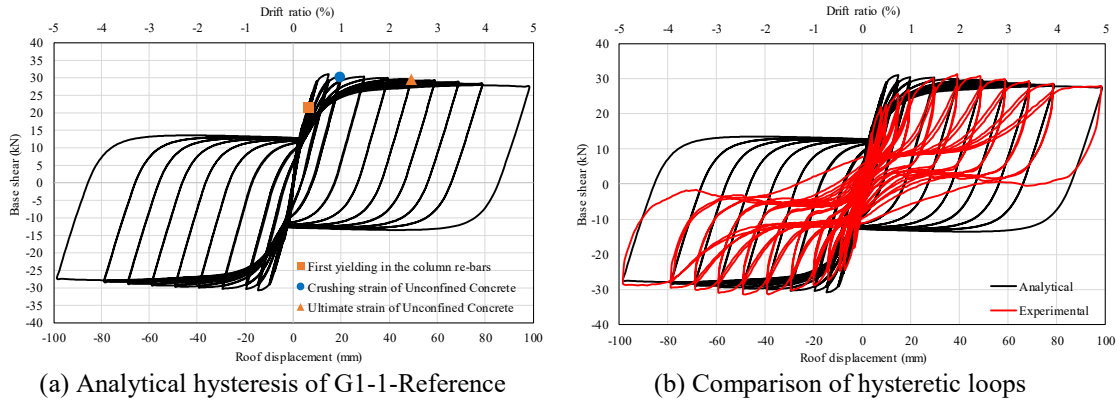
Figure 6.6. *Hysteretic behavior of G1-1-Reference*

(a) Analytical hysteresis of G1-2-Steel   (b) Comparison of hysteretic loops
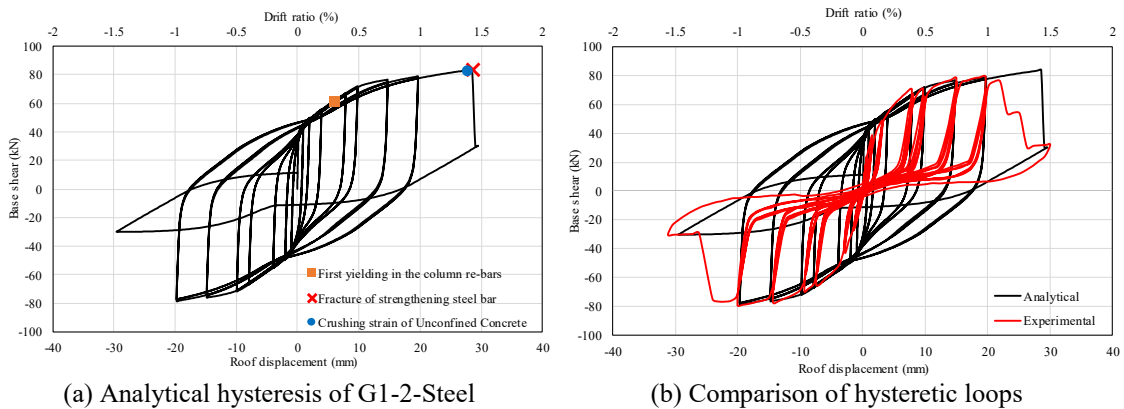
Figure 6.7. *Hysteretic behavior of G1-2-Steel*

In the analytical model, the ultimate laod of G1-2-Steel is 78.2 kN in forward direction and 78.68 kN in backward direction. In real test, the lateral load capacity was obtained as 78.9 kN. The analytical and experimental results are in good agreement in terms of base shear of G1-2-Steel. The strengthening steel bars fractured before the frame reached 1.5% lateral drift in the experimental test. Following the fracturing of the bars, the base shear suddenly dropped to average 30.3 kN in both directions, which was nearly equal to the base shear obtained in the test of G1-1-Reference. The roof drift ratio in G1-2-Steel which the unconfined concrete attained maximum strain is larger than the G1-1-Reference. It means that similar damage level was occurred in later drifts. Obviously, the shape of hysteresis is different from the experimental force vs. displacement relation presented in Figure 4.5. in terms of band width of the hysteresis. The hysteretic loops do not follow any lateral plateau in the loading or unloading paths. This is due to the fact that the lateral stiffness deterioration and the reduction in flexural rigidity at the damaged

125

sections is not introduced in the SeismoStruct. Accordingly, the residual displacement level of frame hysteresis is relatively higher than the experimental result.
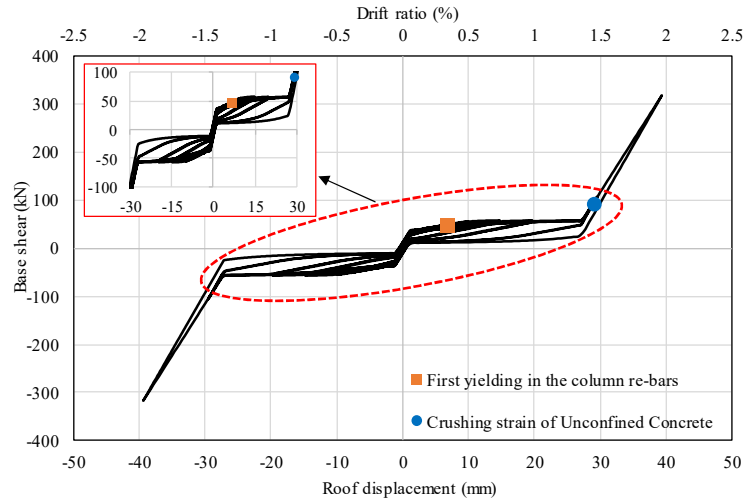
Figure 6.8. *Hysteretic behavior of G1-3-CuAlMn*
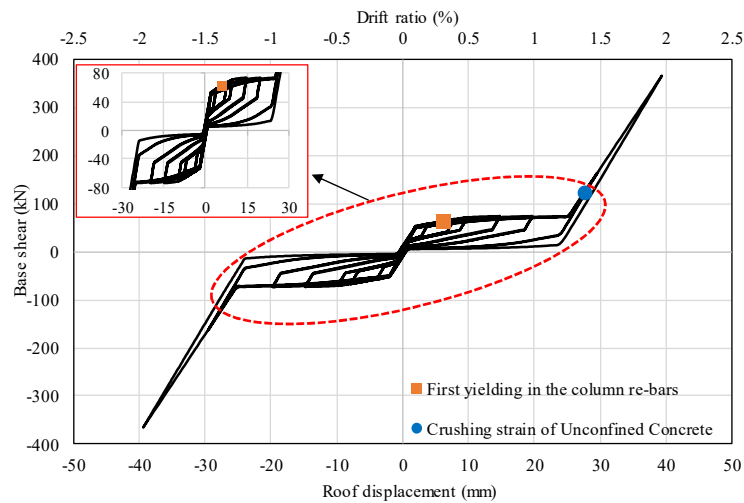
Figure 6.9. *Hysteretic behavior of G1-4-NiTi*

The SMA-strenghtened frames exhibited desired and expected flag-shaped behavior in the analytical model when they are subjected to reversed cyclic loading under constant axial load (Figure 6.8 and Figure 6.9). The main difference between the analytical model and the real test is not to be reflected progressive damage accumulation and improper loading transferring due to compression failure of concrete at a region where the U-shaped plates connected to the beam especially for NiTi strengthened

126

specimen. First of all, the SMAs show fully austenitic and martensitic behavior until the end of the test. The superelastic plateau strain is introduced as 6.5% for CuAlMn and NiTi SMAs at the beginning and the martensitic behavior starts in the hysteresis when the SMA rods reach this strain level. Obviously, the frames, which were upgraded with SMA bars, properly showed re-centering ability in the analytical model due to superelastic property of SMA bars. So, the frames successfully return the original position after removing the applied loading. In addition, the martensitic behavior of hysteresis is clear due to material characteristics. Owing to the inherit feature of SMA materials, the permanent plastic deformations of RC frames is considerably reduced to a negligible point. Apparently, the experimental results are not compatible with the analytical model in terms of lateral load capacity. It is mostly due to the fact that the imposed lateral drift was not directly transmitted to the strengthening bars because of the insufficient rigid design of U-shaped plates and detailing for the connection between the SMAs and RC components. This caused martensitic behavior not observed in the real tests contrary to analytical hysteresis. In the analytical hysteretic loops of G1-3-CuAlMn, the bars are not fractured at the end of the test contrary to the real experiment. This could be possibly resulted from the perfect material characterization and modelling assumptions in the SeismoStruct. Furthermore, it is clear from the figures that NiTi-strengthened frame dissipated more energy due to its wider hysteretic loops. Lastly, it is found out that the unconfined concrete crushes after the frame starts showing the martensitic behavior.

There are some differences in hysteretic behavior of SMA-strengthened frames in terms of ultimate load, shape of hysteresis and martensitic behavior. In real practice, the SMA rods were threaded at the ends with a sufficient length to connect them to the strengthening mechanism and U-shaped plates via nuts. The connections at the ends of rods were subjected to serious stress concentration in the test with the effect of lateral loading. Also, the connection of U-shaped plates to the beam through the bolts were not failed due to shear loading in the tests. However, the magnitude of bending moment had an effect on the bolts around the beam increased with rapidly applied reversed cyclic lateral loading. Afterward, the concrete crushing was visually observed in the beam for SMA-strengthening frames. Then, the lateral load was not correctly transferred to the strengthening rods axially. These are the reasons for G1-3-CuAlMn and G1-4-NiTi frames not to show the real behavior monitored in the experiments.
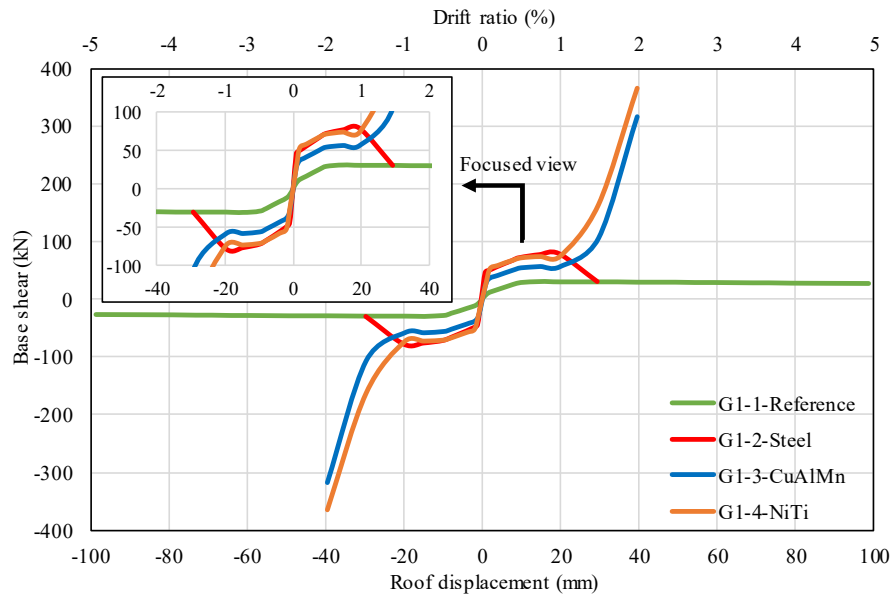
Figure 6.10. *Envelope curves of analyzed frames*

(a) G1-1-Reference

(b) G1-2-Steel

(c) G1-3-CuAlMn

(d) G1-4-NiTi
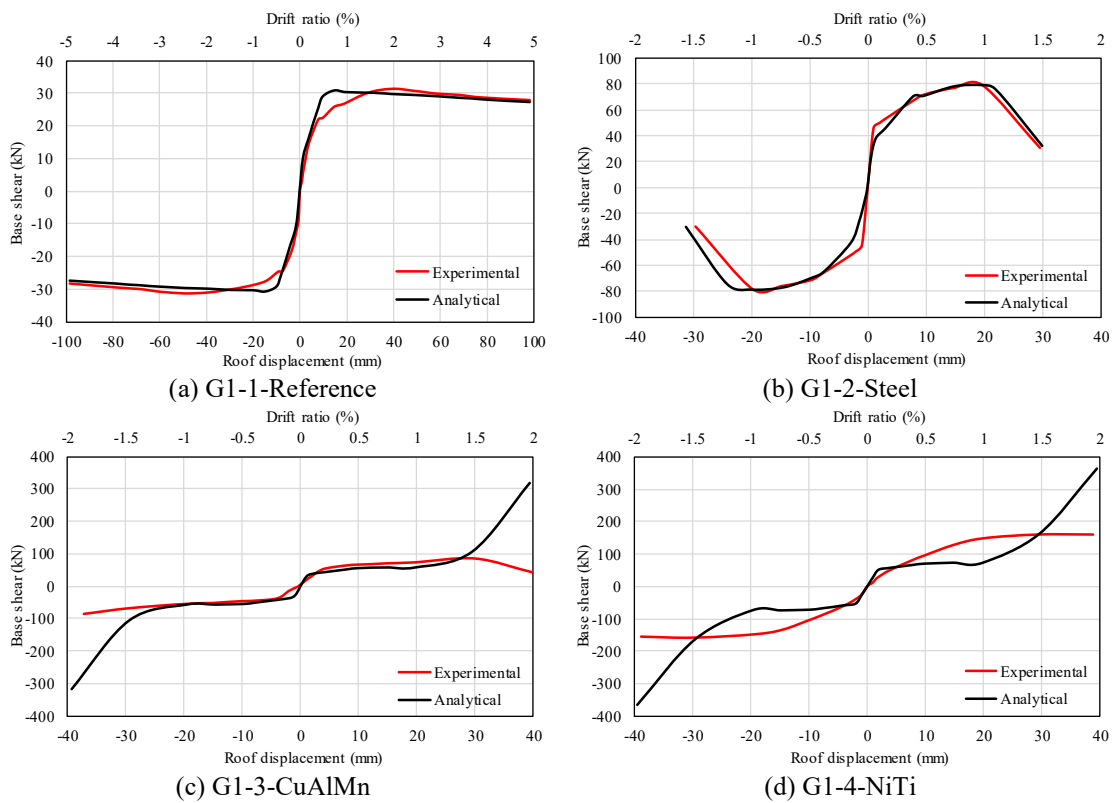
Figure 6.11. *Comparison of envelope curves*

128

The envelope curves of the analyzed RC frames are given in Figure 6.10. Furthermore, the comparison is presented in Figure 6.11 between analytical and experimental envelope curves. The experimental envelope curves are mostly similar to the analytical ones but there are few differences with the envelope curves obtained from experiments. Initially, the martensitic behavior was not clearly observed in the test and there was a sudden decrease in the ultimate load of the frame following the fracturing of strengthening bars (G1-3-CuAlMn). There is also moderate difference in the elastic portion for the SMA-strengthened frames. It is worth to mention that the G1-3-CuAlMn upgraded frame has quite similar trend up to %1.5 lateral drift ratio with experimentally obtained envelope curve. Contrary, there is a considerable difference in the envelope curve trend for the NiTi-strengthened frame due to failure of subcomponents. However, the envelope curves of G1-1-Reference and G1-2-Steel is almost the same as experimentally obtained curve in terms of ultimate lateral load and the observed trend.

6.1. Load vs. Displacement Relationship of Upgrading Materials

The general hysteresis and their skeleton curves obtained from analytical model are discussed in previous part in detail. What we know basically from the loading mechanism is that the applied lateral load to the column end is transferred to the upgrading materials as axial load. Then, the force vs. displacement relationship of strengthening rods is fully perfect in the analytical model, but in real life, it is pretty hard to create such a perfect condition. In the analytical model, the upgrading materials exhibit symmetrical behavior in the forward and backward loading directions. The axial force vs. displacement relationship of analytical models as well as stress calculations are presented in the following Figure 6.12-Figure 6.14.
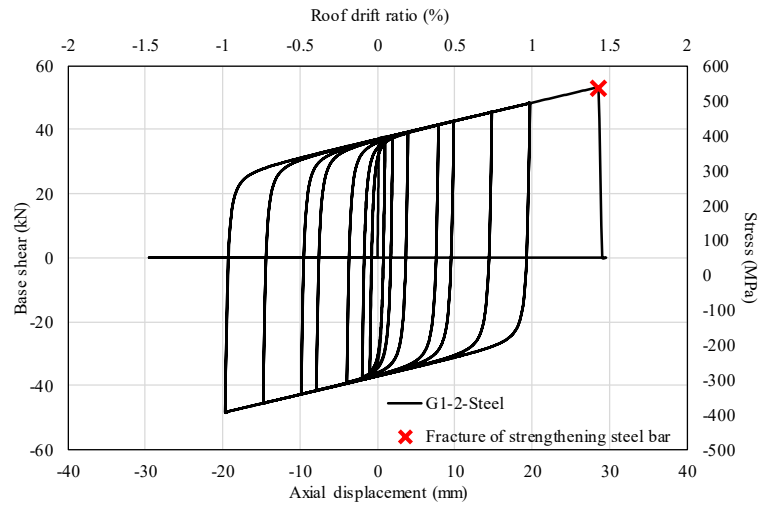
Figure 6.12. *Force vs. displacement relation of G1-2-Steel*

As it is shown in the above figure, the expected ideal behavior of strengthening steel bar is obtained through analysis. The shape of the figure is the similar to the material model introduced to the program before the analysis. So, the behavior of strengthening steel bar is in good agreement with the observed and measured performance in real test. The fracture of steel bar took place before 1.5% roof drift ratio as occurred in the experimental process. Moreover, total axial load capacity of the steel bar carried in the analytical model is very close to the experimental capacity of conventional steel bar. In Figure 4.10, the axial load capacity of a steel bar can be calculated as nearly 25 kN. Then, the axial load capacity of the steel bars for pushing or pulling direction is around 50 kN. Therefore, this capacity is obtained from the analytical model as 53.3 kN.
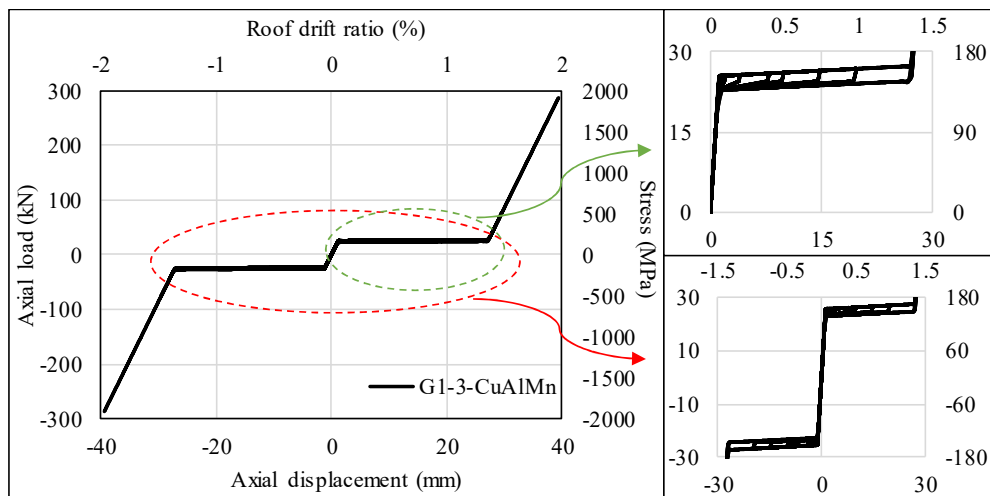
Figure 6.13. *Load vs. displacement relation of G1-3-CuAlMn*

130
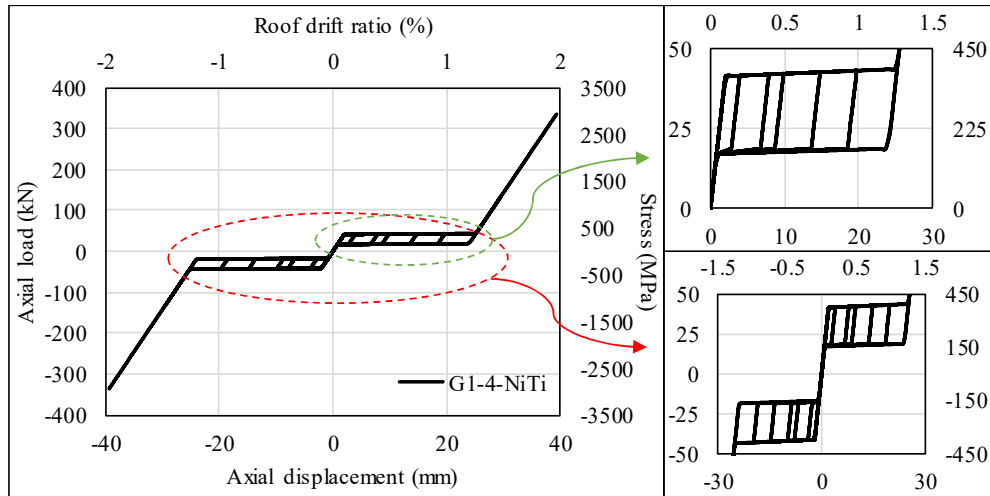
Figure 6.14. *Load vs. displacement relation of G1-4-NiTi*

When it comes to evaluate the hysteresis of SMA-strengthened frames, it is found out that the RC frames exhibited flag-shaped hysteretic curves due to superelastic material property of shape memory alloy bars (Figure 6.8 and Figure 6.9). Herein, similar flag-shaped hysteresis is expectedly observed in the SE CuAlMn and NiTi SMA bars while they are loaded axially. As mentioned before, the constructed analytical model perfectly benefits from the superelastic property of SMAs. In contrast, this perfect behavior could not be catched in the experiments. In analytical model, the austenitic phase is first observed to a degree of the superelastic plateau strain level of SMA bar and then the martensitic behavior starts. The CuAlMn SMA bar has narrow band in load vs. displacement history contrary to NiTi. This is resulted from the difference in material characteristics towards the applied loading. Such a difference in band width is a result of the different transformation stresses of materials while they show superelasticity in the upper and lower plateau of hysteresis (see Figure 3.15-Figure 3.18). Accordingly, dissimilar band width of hysteresis affects the absorbed energy by the bar and so the frame.

7. SUMMARY AND CONCLUSIONS

The main purpose of this study is to investigate the effectiveness of upgrading methodology with different conventional and innovative materials that could be used in substandard RC frames experimentally. A strengthening procedure was conducted with three different materials; conventional Steel bars, Superelastic (SE) CuAlMn Shape Memory Alloy (SMA) bars and lastly SE NiTi SMA bars.

Within the scope of this thesis study, 2/3-scaled one-bay one-storey four reinforced concrete (RC) frames with no infill, which represent the existing substandard RC framed structures with some deficiencies, were designed and constructed in laboratory conditions. All the frames were identical in terms of geometric dimensions and reinforcement detailing. The level of axial load applied to the column top ends was only the ten percent of their axial load capacity due to limited laboratory conditions and safety concerns. Then, a quasi-static displacement-controlled reversed cyclic lateral loading history was applied to all specimens to explore the seismic performance of frames. The first frame was tested as a reference and then the rest of the frames were strengthened with conventional Steel bars, SE CuAlMn and NiTi SMA bars, respectively. A strengthening mechanism was designed, fabricated and incorporated in RC frames in order to contribute the structural performance of specimens under lateral loading. A total of four strengthening bars were used in each of last three experiments with different geometric and mechanical properties. Moreover, ambient vibration measurements were taken at each specimen before and after the tests to detect the change in frequency due to the imposed damage during cyclic loading. At the end of the tests, the results assessed in terms of strength, stiffness, dissipated energy, ductility, hysteretic damping ratio, re-centering, strain gages (SG) data and finally vibration-based monitoring. In addition to performed real tests, analytical models of the RC frames were generated in SeismoStruct platform.

According to the obtained and evaluated results of this study, general upgrading methodology was successful in terms of seismic responses of RC frames under the combined effect of constant axial load and reversed cyclic loading. The conclusions of this study are summarized in the following items;

- The proposed upgrading methodology provided an increment in strength parameter. However, the increase in strength is directly dependent on the geometric

dimensions of the upgrading materials. The specimens attained ultimate loads whose absolute values are the same in the forward and backward loading.

- In this study, the visible damage on the columns were reduced throughout the upgrading procedure. The crack widths in the upgraded RC frames were relatively lower than the reference specimen.

- Considerable increment was provided in lateral stiffnesses of the RC frames through upgrading methodology in terms of initial stiffness, secand stiffness and peak-to-peak stiffness.

- The axial rigidity of the upgrading materials is quite effective in calculation of initial stiffnesses of the RC frames. The initial stiffness value of the Steel-strengthened specimen, which is called as G1-2-Steel in this study, was 4.86 times greater than reference frame. Similar contributions to the rigidity of the frames were provided by CuAlMn and NiTi strengthened frames. The initial stiffness of G1-4-NiTi was higher than the G1-3-CuAlMn by 50% since the modulus of elasticity of NiTi in the austenite region is 18% greater than CuAlMn. Nonetheless, the secand stiffness of the G1-4-NiTi is lower than G1-3-CuAlMn.

- The dissipated energy of RC framed structures during the earthquake excitation is important property showing the capability of absorbing input energy coming from ground shaking. In this study, the reference frame had maximum energy dissipating capacity since it sustained its lateral drift up to 5% without distinct strength reduction. At 1.5% lateral drift, which is common for all tested RC frames, NiTi-strengthened frame dissipated the input energy at most. The interesting result is that the dissipated energy by the G1-3-CuAlMn is lower than G1-2-Steel though superelastic effect of CuAlMn bars. To be able to comment on this difference, it is essential to look at the material test results. In the uniaxial cyclic tension test, the hysteretic loops of CuAlMn is relatively narrower than the steel. In the second cyclic lateral drifts, the CuAlMn-strengthened frame dissipated more energy than the steel-strengthened frame at 1.5% roof drift where the maximum dissipation was observed in G1-4-NiTi.

- In this study, the RC frames designed such that the formation of plastic hinges concentrated at the end regions of columns and the overall behavior was in flexural. The RC frames showed ductile performance during the experiments with or without upgrading strategy. For the SMA strengthened frames, the martensitic behavior of SE SMAs is effective in ductile behavior. It can be easily observed in the analytically obtained

behavior of RC frames. Due to the insufficient rigid connection detailing between SMA bars and RC components, the martensitic behavior was not fully observed in CuAlMn and NiTi.

- The RC frames displayed variable characteristics in hysteretic damping. Surprisingly, the trend in reference frame is very well in the first and second cyclic drifts. Besides, the steel strengthened frame showed outstanding performance in the first cycles. But, in the second cycles, the hysteretic damping of G1-2-Steel dramatically decreased, and the viscous damping ratio of SMA-strengthened frames was considerably larger than G1-2-Steel due to superelastic cyclic characteristics. In the first cyclic drifts, damping characteristics of SMAs were similar to each other, but CuAlMn-strengthened frames exhibited superior performance in the second cyclic drifts compared to that of G1-4-NiTi.

- Within the scope of this study, two different estimations were made to best reflect and interpret the re-centering feature of SMAs considering the shape of hysteresis. G1-3-CuAlMn showed fully re-centering property with negligible residual displacements in comparison to other tests. The self-centering mechanism was obviously observed in the frame hysteresis and CuAlMn bar hysteresis as well as stress vs. strain relationship of the bars. Interestingly, the shape of the steel-strengthened frame hysteresis indicated well performance in terms of residual displacement compared to reference frame even if the conventional steel experienced permanent deformations following the removal of applied loading in the material tests. The residual values of G1-4-NiTi was noticeably larger than the G1-1-Reference and G1-2-Steel in the first method because of unexpected connection failure of U-shaped plates. Additionally, in the second method of calculations where the shape of hysteresis was considered, only three hysteresis were evaluated except for G1-3-CuAlMn. Herein, G1-4-NiTi provides more advantage compared to the first and second experiment in terms of residual values. The recovery process might be called as fully in G1-3-CuAlMn and partially in G1-4-NiTi.

- It is important to consider that the strain rate used in the frame tests and material tests are different from each other. The real seismic excitation frequency is larger than the frequency used in this study during the experiments. So, the physical behavior of the SMAs are sensible to stress, strain and temperature under cyclic loading, but in this study, the re-centering property is found to be insensitive to the strain rate.

- The ambient vibration measurements provided valuable information about the change in the rigidity of the frames after the damage occurred. Before the tests, there are almost no differences in the undamaged frequencies, but at the end of the tests, the damaged frequencies were similar. In the G1-2-Steel, the vibration-based results were questionable due to similarity between undamaged and damaged condition. According to the results, SMA-strengthened frames were experienced less softening in rigidity while they tolerated 2% lateral drift contrary to the reference specimen.

- For the G1-1-Reference and G1-2-Steel, the analytical model is well matched with the experimental results in terms of ultimate load, load vs. displacement relation of strengthening bars and variation in strain of reinforcement and unconfined concrete in the hysteresis. But, similar result could not be obtained for G1-3-CuAlMn and G1-4-NiTi. The analytical model showed perfect self-centering without residual displacement as well as no fracturing in the bars. However, re-centering mechanism in the experimental hysteresis was obviously took place in the G1-3-CuAlMn. Here, the model assumptions are very important to reproduce the real behavior if there is no systematic error in the experiment.

- In conclusion, it is quite essential to construct fully-rigid subcomponents of a system involving SMAs to observe self-centering mechanism. If the subcomponents fail due to any error, it could be highly problematic to discover the properties of SMA. The proposed strengthening system was generally successful in this study. But, the region where the U-shaped plates connected to the beam was seriously damaged due to the magnitude of higher lateral loading, especially in the G1-4-NiTi. If the horizontal length of the U-shaped plates had been longer or the height of the plates had been higher to the slab level, the tolerated lateral drift by the strengthened frames might have been more.

- As a general conclusion, the SMAs offer many advantages compared to conventional materials for the structural engineering applications due to inherit material characterization. Such an improvement in the seismic behavior of RC frames are observed in this study. But, more emphasis should be put on discovering the effectiveness of SMA materials in the field of seismic upgrading together with finite element modelling of proposed system to validate the results.

REFERENCES

Abdulridha, A., and Palermo, D. (2017). Behaviour and modelling of hybrid SMA-steel reinforced concrete slender shear wall. *Engineering Structures*, 147, 77-89.

Akın, E. (2011). *Strengthening of brick infilled RC frames with CFRP reinforcement-general principles.* Doctoral Thesis Study. Ankara: Middle East Technical University, Graduate School of Sciences

Akın, E., Canbay, E., Binici, B., and Özcebe, G. (2011). Testing and analysis of infilled reinforced concrete frames strengthened with CFRP reinforcement. *Journal of Reinforced Plastics and Composites*, 30(19), 1605-1620.

Almeida, A., Ferreira, R., Proença, J. M., and Gago, A. S. (2017). Seismic retrofit of RC building structures with Buckling Restrained Braces. *Engineering Structures*, 130, 14-22.

Amezquita-Sanchez, J. P., and Adeli, H. (2016). Signal processing techniques for vibration-based health monitoring of smart structures. *Archives of Computational Methods in Engineering,* 23(1), 1-15.

Araki, Y., Endo, T., Omori, T., Sutou, Y., Koetaka, Y., Kainuma, R., and Ishida, K. (2011). Potential of superelastic Cu–Al–Mn alloy bars for seismic applications. *Earthquake Engineering and Structural Dynamics,* 40(1), 107-115.

Araki, Y., Shrestha, K. C., Maekawa, N., Koetaka, Y., Omori, T., and Kainuma, R. (2016). Shaking table tests of steel frame with superelastic Cu–Al–Mn SMA tension braces. *Earthquake Engineering and Structural Dynamics,* 45(2), 297-314.

Arslan, M. E., and Durmus, A. (2014). Modal parameter identification of in-filled RC frames with low strength concrete using ambient vibration. *Structural Engineering and Mechanics,* 50(2), 137-149.

ARTeMIS – Operational Modal Analysis Software Provided by Structural Vibration Solutions A/S. Available at: http://www.svibs.com/ (accessed October 2008).

Atli, K. C. (2016). The effect of tensile deformation on the damping capacity of NiTi shape memory alloy. *Journal of Alloys and Compounds,* 679, 260-267.

Bal, İ. E., Crowley, H., Pinho, R., and Gülay, F. G. (2008). Detailed assessment of structural characteristics of Turkish RC building stock for loss assessment models. *Soil Dynamics and Earthquake Engineering,* 28(10-11), 914-932.

Cardone, D. (2012). Re-centring capability of flag-shaped seismic isolation systems. *Bulletin of Earthquake Engineering,* 10(4), 1267-1284.

Casciati, F., Faravelli, L., and Hamdaoui, K. (2007). Performance of a base isolator with shape memory alloy bars. *Earthquake Engineering and Engineering Vibration,* 6(4), 401-408.

Cortés-Puentes, L., Zaidi, M., Palermo, D., and Dragomirescu, E. (2018). Cyclic loading testing of repaired SMA and steel reinforced concrete shear walls. *Engineering Structures, 168,* 128-141.

Cruz Noguez, C. A., and Saiidi, M. S. (2011). Shake-table studies of a four-span bridge model with advanced materials. *Journal of Structural Engineering,* 138(2), 183-192.

Cruz Noguez, C. A., and Saiidi, M. S. (2012). Performance of advanced materials during earthquake loading tests of a bridge system. *Journal of Structural Engineering,* 139(1), 144-154.

Del Vecchio, C., Di Ludovico, M., Prota, A., and Manfredi, G. (2016). Modelling beam-column joints and FRP strengthening in the seismic performance assessment of RC existing frames. *Composite Structures,* 142, 107-116.

DesRoches, R., and Smith, B. (2004). Shape memory alloys in seismic resistant design and retrofit: a critical review of their potential and limitations. *Journal of Earthquake Engineering,* 8(03), 415-429.

Di Sarno, L., and Elnashai, A. S. (2002). Seismic retrofitting of steel and composite building structures. Mid-America Earthquake Center CD Release 02-01.

Di Sarno, L., Elnashai, A. S., and Nethercot, D. A. (2006). Seismic retrofitting of framed structures with stainless steel. *Journal of Constructional Steel Research,* 62(1-2), 93-104.

Dolce, M., Cardone, D., and Marnetto, R. (2000). Implementation and testing of passive control devices based on shape memory alloys. *Earthquake engineering and structural dynamics,* 29(7), 945-968.

Dolce, M., Cardone, D., Ponzo, F. C., and Valente, C. (2005). Shaking table tests on reinforced concrete frames without and with passive control systems. *Earthquake Engineering and Structural dynamics*, *34*(14), 1687-1717.

DPT, (1999), Depremin Ekonomik ve Sosyal Etkileri, Muhtemel Finansman İhtiyacı, Kısa, Ortave Uzun Vadede Alınabilecek Tedbirler, Ankara.

Eatherton, M. R., Fahnestock, L. A., and Miller, D. J. (2014, July). Self-centering buckling restrained brace development and application for seismic response mitigation. *In 10th US National Conference on Earthquake Engineering: Frontiers of Earthquake Engineering,* NCEE 2014, Anchorage, Alaska, 21-25 July.

Elnashai, A. S., and Di Sarno, L. (2008). *Fundamentals of earthquake engineering,* New York: Wiley.

El-Betar, S. A. (2016). Seismic vulnerability evaluation of existing RC buildings. *HBRC Journal*.

Erdik, M. (2001). *Report on 1999 Kocaeli and Düzce (Turkey) earthquakes.* In Structural control for civil and infrastructure engineering, 149-186.

Escobar, J. A., Sosa, J. J., and Gómez, R. (2005). Structural damage detection using the transformation matrix, *Computers and structures,* 83(4), 357-368.

Fan, W., and Qiao, P. (2011). Vibration-based damage identification methods: A review and comparative study. *Structural Health Monitoring,* 10(1), 83-111.

FEMA, P. (2000). Commentary for the seismic rehabilitation of buildings. *FEMA-356, Federal Emergency Management Agency,* Washington, DC.

FEMA, A. (2007). 461/Interim Testing Protocols for Determining the Seismic Performance Characteristics of Structural and Nonstructural Components. *Applied Technology Council,* Redwood City, CA, 113.

Fugazza, D. (2003). *Shape-memory alloy devices for earthquake engineering: Mechanical properties, constitutive modeling and numerical simulations.* Master of Science Thesis. Italy: University of Pavia

Fugazza, D. (2005). *Experimental investigatin on the cyclic properties of superelastic NiTi Shape-Memory Alloy wires and bars*. Thesis of Doctoral Degree: University of Pavia

Gao, N., Jeon, J. S., Hodgson, D. E., and DesRoches, R. (2016). An innovative seismic bracing system based on a superelastic shape memory alloy ring. *Smart Materials and Structures,* 25(5), 055030.

Garcia, R., Hajirasouliha, I., and Pilakoutas, K. (2010). Seismic behaviour of deficient RC frames strengthened with CFRP composites. *Engineering Structures,* 32(10), 3075-3085.

Gencturk, B., Araki, Y., Kusama, T., Omori, T., Kainuma, R., and Medina, F. (2014). Loading rate and temperature dependency of superelastic Cu–Al–Mn alloys. *Construction and Building Materials,* 53, 555-560.

Ghassemieh, M., Mostafazadeh, M., and Sadeh, M. S. (2012). Seismic control of concrete shear wall using shape memory alloys. *Journal of Intelligent Material Systems and Structures,* 23(5), 535-543.

Ghorbani-Renani, I., Velev, N., Tremblay, R., Palermo, D., Massicotte, B., and Léger, P. (2009). Modeling and testing influence of scaling effects on inelastic response of shear walls. *ACI Structural Journal,* 106(3), 358.

Han, Y. L., Li, Q. S., Li, A. Q., Leung, A. Y. T., and Lin, P. H. (2003). Structural vibration control by shape memory alloy damper. *Earthquake engineering and Structural dynamics,* 32(3), 483-494.

Hosseini, F., Gencturk, B., Lahpour, S., and Gil, D. I. (2015). An experimental investigation of innovative bridge columns with engineered cementitious composites and Cu–Al–Mn super-elastic alloys. *Smart Materials and Structures,* 24(8), 085029.

Fujita, M., Takanashi, T., Kuzume, K., Ueda, T., Kobayashi, A., Joray, D., Diggelmann, M., Bob, C., San, S., Badea, C., Gruin, A., Iures, L., Ajdukiewicz, A.B., Hulimka, J.S., Hong, G., Chung, Y., and Chung, H. (2010). Case Studies of Rehabilitation, Repair, Retrofitting, and Strengthening of Structures (Vol. 12). International Association for Bridge and Structural Engineering. IABSE.

Inci, P., Goksu, C., Demir, U., and Ilki, A. (2017). Ambient vibration testing of different levels of structural seismic damage, *International Conference on Earthquake Engineering and Structural Dynamics,* 12-14 June, Reykjavik, Iceland

ISO 13822 (2010). Bases for design of structures – Assessment of existing structures. Geneve: ISO TC98/SC2

Johnson, R., Padgett, J. E., Maragakis, M. E., DesRoches, R., and Saiidi, M. S. (2008). Large scale testing of nitinol shape memory alloy devices for retrofitting of bridges. *Smart materials and structures,* 17(3), 035018.

Lee, H. S., Kage, T., Noguchi, T., and Tomosawa, F. (2003). An experimental study on the retrofitting effects of reinforced concrete columns damaged by rebar corrosion strengthened with carbon fiber sheets. *Cement and concrete research,* 33(4), 563-570.

Li, H., Liu, Z. Q., and Ou, J. P. (2007). Study on reinforced concrete beams strengthened using shape memory alloy wires in combination with carbon-fiber-reinforced polymer plates. *Smart Materials and Structures,* 16(6), 2550.

Lobo, P. S., Almeida, J., and Guerreiro, L. (2015). Shape memory alloys behaviour: A review. *Procedia Engineering,* 114, 776-783.

Mander, J.B., Priestley, M.J.N., and Park, R. (1988). Theoretical stress-strain model for confined concrete. *Journal of Structural Engineering,* 114(8), 1804-1826.

Melkumyan, M. (2013). Comparison of Innovative Base Isolation Retrofitting Technology with Conventional Retrofitting of Existing Buildings. *In Computational Methods in Earthquake Engineering,* 461-490, Springer Netherlands.

Menegotto M., Pinto P.E. (1973). Method of analysis for cyclically loaded R.C. plane frames including changes in geometry and non-elastic behaviour of elements under combined normal force and bending. *Symposium on the Resistance and Ultimate Deformability of Structures Acted on by Well Defined Repeated Loads,* International Association for Bridge and Structural Engineering, Zurich, Switzerland, 15-22.

Ozbulut, O. E., and Hurlebaus, S. (2010). Seismic assessment of bridge structures isolated by a shape memory alloy/rubber-based isolation system. *Smart Materials and Structures,* 20(1), 015003.

Ozbulut, O. E., and Hurlebaus, S. (2011). Re-centering variable friction device for vibration control of structures subjected to near-field earthquakes. *Mechanical Systems and Signal Processing,* 25(8), 2849-2862.

Ozbulut, O. E., Hurlebaus, S., and Desroches, R. (2011). Seismic response control using shape memory alloys: a review. *Journal of Intelligent Material Systems and Structures*, 22(14), 1531-1549.

Ozcelik, O., Amaddeo, C., Misir, S., Durmazgezer, E., and Yücel, U. (2015), "Modal identification results of RC frames at different damage levels", *3rd Conference on Smart Monitoring Assessment and Rehabilitation of Civil Structures,* Antalya, Turkey, September

Parsons, T. (2004). Recalculated probability of M≥ 7 earthquakes beneath the Sea of Marmara, Turkey. *Journal of Geophysical Research: Solid Earth,* 109(B5).

Prota, A., De Cicco, F., and Cosenza, E. (2009). Cyclic behavior of smooth steel reinforcing bars: experimental analysis and modeling issues. *Journal of Earthquake Engineering,* 13(4), 500-519.

Saiidi, M. S., Sadrossadat-Zadeh, M., Ayoub, C., and Itani, A. (2007). Pilot study of behavior of concrete beams reinforced with shape memory alloys. *Journal of Materials in Civil Engineering,* 19(6), 454-461.

SAP2000, C. S. I. (2013). Computers and Structures Inc. Berkeley, CA, USA.

SeismoSoft (2011). SeismoStruct - A computer program for static and dynamic nonlinear analysis of framed structures, Available from URL: www.seismosoft.com

Shajil, N., Das, D., and Chandrasekaran, L. (2009). Effects of cycling on the pseudoelastic properties of CuAlMnNi and TiNi based pseudoelastic alloys. *The International Journal of Structural Changes in Solids,* 1(1), 171-185.

Shin, M., and Andrawes, B. (2010). Lateral cyclic behavior of reinforced concrete columns retrofitted with shape memory spirals and FRP wraps. *Journal of Structural Engineering,* 137(11), 1282-1290.

Shrestha, K. C., Araki, Y., Nagae, T., Koetaka, Y., Suzuki, Y., Omori, T., and Ishida, K. (2013). Feasibility of Cu–Al–Mn superelastic alloy bars as reinforcement elements in concrete beams. *Smart Materials and Structures,* 22(2), 025025.

Shrestha, K. C., Saiidi, M. S., and Cruz, C. A. (2015). Advanced materials for control of post-earthquake damage in bridges. *Smart Materials and Structures,* 24(2), 025035.

Song, G., Ma, N., and Li, H. N. (2006). Applications of shape memory alloys in civil structures. *Engineering structures,* 28(9), 1266-1274.

Speicher, M. S., DesRoches, R., and Leon, R. T. (2011). Experimental results of a NiTi shape memory alloy (SMA)-based recentering beam-column connection. *Engineering structures,* 33(9), 2448-2457.

Tapan, M., Comert, M., Demir, C., Sayan, Y., Orakcal, K., and Ilki, A. (2013). Failures of structures during the october 23, 2011 Tabanlı (Van) and november 9, 2011 Edremit (Van) earthquakes in Turkey. *Engineering Failure Analysis,* 34, 606-628.

Tazarv, M., and Saiid Saiidi, M. (2014). Reinforcing NiTi superelastic SMA for concrete structures. *Journal of Structural Engineering,* 141(8), 04014197.

Turkish Earthquake Code (2007). Specification for buildings to be built in seismic zones, Ministry of Public Works and Settlement Government of Republic of Turkey; Ankara, Turkey

Thermou, G. E., and Elnashai, A. S. (2006). Seismic retrofit schemes for RC structures and local-global consequences. *Progress in Structural Engineering and Materials,* 8(1), 1-15.

TS EN 12390-2, Sertleşmiş Beton Deneyleri, Bölüm-2, Dayanım Deneylerinde Kullanılacak Deney Numunelerinin Hazırlanması ve Kürlenmesi, Türk Standartları Enstitüsü, Ankara, Nisan, 2002

Uçarkuş, G. (2010). *Active Faulting And Earthquake Scarps A Long The North Anatolian Fault In The Sea Of Marmara.* Doctoral dissertation. Istanbul: Avrasya Earth Science Institute

Wang, B., and Zhu, S. (2018). Superelastic SMA U-shaped dampers with self-centering functions. *Smart Materials and Structures,* 27(5), 055003.

Wenzel, H., and Pichler, D. (2005). *Ambient vibration monitoring.* John Wiley & Sons.

Wilson, J. C., and Wesolowsky, M. J. (2005). Shape memory alloys for seismic response modification: a state-of-the-art review. *Earthquake Spectra,* 21(2), 569-601.

Yılmaz, N., and Avşar, Ö. (2013). Structural damages of the May 19, 2011, Kütahya–Simav earthquake in Turkey. *Natural hazards,* 69(1), 981-1001.

Youssef, M. A., Alam, M. S., and Nehdi, M. (2008). Experimental investigation on the seismic behavior of beam-column joints reinforced with superelastic shape memory alloys. *Journal of Earthquake Engineering,* 12(7), 1205-1222.

Zafar, A., and Andrawes, B. (2012). Incremental dynamic analysis of concrete moment resisting frames reinforced with shape memory composite bars. *Smart Materials and Structures,* 21(2), 025013.

CV

Name-Surname	: Burak DURAN
Foreign Language	: English
Date and Place of Birth	: Tokat / 1992
E-mail	: burak.duran@deu.edu.tr, burakduran05@gmail.com

Education and Professional History:

- 2015, B.Sc. Degree, Anadolu University, Engineering Faculty, Department of Civil Engineering
- 2016, Civil Engineer, Doğanca Const. and Cons. Company
- 2017, Research Assistant, Dokuz Eylul University, Engineering Faculty, Department of Civil Engineering, Mechanics Division

Publications and Scientific Activities

- Duran, B., Tunaboyu, O., Avşar, Ö. (2017). Binaların Risk Değerlendirmesine Düşük Dayanımlı Beton Elastisite Modülünün Etkisi. Uluslararası Doğal Afetler ve Afet Yönetimi Sempozyumu, 2-4 Mart 2016, Karabük, Türkiye, 2016

- Duran, B., Tunaboyu, O., Avşar, Ö. (2017). Determination of elasticity modulus of low strength concrete and its effect on the risk assessment results by DSVB. Journal of the Faculty of Engineering and Architecture of Gazi University, 32(1), 275-286

- Duran, B., Tunaboyu, O., Kaplan, O., Avşar, Ö. (2017). CFRP ile Gerçekleştirilen Yapısal Onarım Aşamalarının Betonarme Çerçeve Rijitliğine Katkısı. 4.Uluslararası Deprem Mühendisliği ve Sismoloji Konferansı, 11-13 Ekim, Eskişehir, Türkiye

- Duran, B., Tunaboyu, O., and Avşar, Ö. (2017). Malzeme Dayanımlarının Standart Altı Betonarme Çerçevelerin Sismik Performansına Etkisi. 4.Uluslararası Deprem Mühendisliği ve Sismoloji Konferansı, 11-13 Ekim, Eskişehir, Türkiye

- Duran, B., Tunaboyu, O., Kaplan, O., and Avşar, Ö. (2018). Ambient Vibration Testing Of A Damaged Substandard RC Frame At Each Structural Repair Steps with CFRPs, 16th European Conference on Earthquake Engineering, 18-21 June, Thessaloniki, Greece
- Duran B., Tunaboyu O., Kaplan O., and Avşar Ö., (2018). Effectiveness of Seismic Repairing Stages with CFRPs on the Seismic Performance of Damaged RC Frames. Structural Engineering and Mechanics (In Press)

Member of Professional Organization

- 2016, Chamber of Civil Engineering, İzmir.